12-18-2020

Controlled membrane remodeling by Nanospheres and Nanorods: Experiments targeting the design principles for membrane-based materials

Sarah Zuraw-Weston
University of Massachusetts Amherst

Controlled membrane remodeling by Nanospheres and Nanorods: Experiments targeting the design principles for membrane-based materials

A Dissertation Presented

by

SARAH E. ZURAW-WESTON

Submitted to the Graduate School of the
University of Massachusetts Amherst in partial fulfillment
of the requirements for the degree of

DOCTOR OF PHILOSOPHY

September 2020

Department of Physics

Controlled membrane remodeling by Nanospheres and Nanorods: Experiments targeting the design principles for membrane-based materials

A Dissertation Presented

by

SARAH E. ZURAW-WESTON

Approved as to style and content by:

_____
Anthony D. Dinsmore, Chair

_____
Jennifer Ross, Member

_____
Chris Santangelo, Member

_____
Maria Santore, Member

_____
Narayanan Menon, Department Head
Department of Physics

ACKNOWLEDGMENTS

I would like to thank my advisor, Tony Dinsmore, for his years of guidance, thoughtful advice, patience, and gentleness. These past few years of study have been an absolute delight and it is due to the kind, curious and caring atmosphere Tony has cultivated in the Lab by modeling those traits in his mentorship. In particular, his ability to thoughtfully comprehend and empathize with other perspectives (scientific and otherwise) has been invaluable in crafting holistic views of the context of this research. I would also like to thank my committee members, Chris Santangelo, Jennifer Ross and Maria Santore for their helpful discussion and input throughout my graduate studies. A special thank you to Jenny for being a role model and guide both in my undergraduate and graduate career serving on both my undergraduate and graduate thesis committees. Thank you also to Laura Cadonati for guiding and advising me as an undergraduate researcher. Laura provided a model for me just as I was starting my studies as a physicist and helped me to establish my identity as someone who could and does love physics.

I would also like to thank my peers, Rui Cao, Arash Manafirad, Wei He, Mingzhu Cui, Robert Keane, Zachary Curtis, and Alyssa Conway. Rui and Arash for the invaluable input and camaraderie as we tackled the challenges of membrane experiment together. Wei He for being a guide to many of us as a senior student. Mingzhu, Rob and Zach for being tremendous lab mates ready and willing to help, learn, and grow together. I would also like to thank Alyssa Conway for her insight into image analysis techniques. All have been good friends and it has been my tremendous honor to work with each one.

Finally, I would like to thank my family and friends for their support during not only my graduate studies but for all the love, sacrifice and small victories over the years that have allowed me to arrive here. I do not take for granted the tremendous achievement that this represents and not just for me but for the community I represent. Special thank you to my parents Joseph and Celia, my sisters Elizabeth and Ruth, and my husband Ian. To all the friends, teachers and family members who have supported me in this effort, thank you. I would like to thank God for his great grace and mercy. How truly blessed I have been.

ABSTRACT

CONTROLLED MEMBRANE REMODELING BY NANOSPHERES AND NANORODS: EXPERIMENTS TARGETING THE DESIGN PRINCIPLES FOR MEMBRANE-BASED MATERIALS

SEPTEMBER 2020

SARAH E. ZURAW-WESTON, B.A., UNIVERSITY OF MASSACHUSETTS. AMHERST
PH. D., UNIVERSITY OF MASSACHUSETTS AMHERST

Directed by: Professor Anthony D. Dinsmore

In this thesis we explore two experimental systems probing the interactions of nanoparticles with lipid bilayer membranes. Inspired by the ability of cell membranes to alter their shape in response to bound particles, we report two experimental studies: one of nanospheres the other of long, slender nano-rods binding to lipid bilayer vesicles and altering the membrane shape. Our work illuminates the role of particle geometry, particle concentration, adhesion strength and membrane tension in how membrane morphology is determined. We combine giant unilamellar vesicles with oppositely charged nanoparticles, carefully tuning adhesion strength, membrane tension and particle concentration.

In the case of nanospheres we show that spherical nanoparticles binding to lipid-bilayer membrane vesicles results in a remarkably rich set of collective morphologies that are controllable via the particle binding energy. We separately study cationic and anionic particles, where the adhesion is tuned by addition of oppositely charged lipids to the vesicles. When the binding energy is weak relative to a characteristic membrane-bending energy, vesicles adhere to one another and form a soft solid gel, a novel and useful platform for controlled release. With larger binding energy, a transition from partial to complete wrapping of the nanoparticles causes a remarkable vesicle destruction process culminating in rupture, nanoparticle-membrane tubules, and an apparent inversion of the vesicles.

In the case of nanorods when we increased adhesion strength, the primary behaviors observed are membrane deformation, vesicle-vesicle adhesion, and vesicle rupture. These behaviors are observed in well-defined regions in the parameter space with sharp transitions between them. We observed deformation of the membrane resulting in tubulation, texted surfaces, small dark aggregates, and large aggregates. These responses are robust and repeatable providing a physical understanding of the dependence on shape, binding affinity, and particle concentration in membrane remodeling. These findings help unify the diverse phenomena observed previously as well as present new particle induced morphologies. They open the door to a new class of vesicle-based, closed-cell gels that are more than 99% water and can encapsulate and release on demand, and show how to drive intentional membrane remodeling for shape-responsive systems.

TABLE OF CONTENTS

Page

LIST OF FIGURES

CHAPTER 1

INTRODUCTION TO LIPID MEMBRANES

The lipid bilayer membrane works in tandem with proteins and other biomolecules to provide the cell with its shape, facilitate the transport of cargo, and protect the interior of the cell, see figure 1.1.[1,2,3] Despite how fundamental a system the cell is, a clear physical description remains elusive. Moreover, it is difficult to extract basic physical mechanisms with the full complications of the cell. Experiments with simplified systems are thus needed to elucidate these complex interactions. The goal of this dissertation is to pursue a detailed physical description of the lipid bilayer via a systematic experimental design. In doing so one can derive insight into how nanoparticles interact with biological membranes.

This work also has relevance in biomedical and material science application and can be applied toward the development of soft reconfigurable membrane-based materials. The lipid-bilayer membrane offers an enormous range of applications because it is thin, flexible, impermeable to most solutes, and fluid-like in its plane.[4,5] Its flexibility allows the membrane to curve around binding particles or proteins or viruses, leading to the potential for major shape reorganization. Live cells harness these interactions to tune morphology and function, such as in the bicontinuous structure of the endoplasmic reticulum, protrusions leading to cell mobility, [1,6,7,8] or enwrapped objects in phagocytosis or endocytosis.2·3 There has been great progress in the application of synthetic lipid bilayers for encapsulation and delivery.[9] Lipid membranes can support the embedding and encapsulation of cargo via membrane deformation making them useful for fabricating cell-membrane mimicking materials and drug delivery. Lipid membranes have also been used to create biosensor technologies for monitoring food toxicants and environmental pollutants.[10] Despite the enormous progress in the application of synthetic lipid bilayers for

encapsulation and delivery, there is considerably greater (and still undeveloped) potential if we can learn how to trigger changes in membrane geometry and topology in synthetic systems. This knowledge would lead to new responsive, bioinspired materials that could modulate morphology and function in complex ways, on demand.

The results in this thesis show how it is possible to tune morphology and shape-changing dynamics of vesicles via the controlled binding of nanoparticles. This provides a potentially useful experimental model of cell lysis or formation of filipodia in cells[1] and it opens the door to new applications. These findings could be used to create cargo-carrying vesicles with the ability to rupture when bound particles are stimulated or, potentially, when particle binding is tuned by an external trigger. [11] These results also show how to engineer soft solid gels that can encapsulate cargo. They may also provide a unified picture for the wide variety of phenomena reported in cells and vesicles, which likely correspond to different regions of a phase space defined chiefly by particle binding strength, the membrane bending modulus, membrane tension, particle geometry and particle concentration.

This dissertation is divided into five chapters. The first chapter introduces the field of lipid membrane physics and presents the key parameters that govern the deformation of lipid membranes by the binding of nanoparticles. Chapter two describes the methods and materials used to obtain the results reported in this document and provides details on protocols and specific techniques. The third and fourth chapters present the detailed results of experiments looking at the interactions of lipid bilayer membranes with spherical and rod-shaped nanoparticles, respectively. The last chapter presents a summary of the results presented in this dissertation, provides context for their significance, and presents suggestions for future research.

This chapter is divided into three sections. The first section introduces the physical properties of lipid bilayer membranes and outlines how to characterize the deformation of the membrane induced by the binding of spherical nanoparticles to the membrane. The second section extends this reasoning to non-spherical particles, in particular rod-shaped particles. The final section comments on the complex membrane-mediated interactions of the many-particle system. The purpose of this first chapter is to prepare our consideration of the results presented in chapters three and four in view of the present literature on the topic.

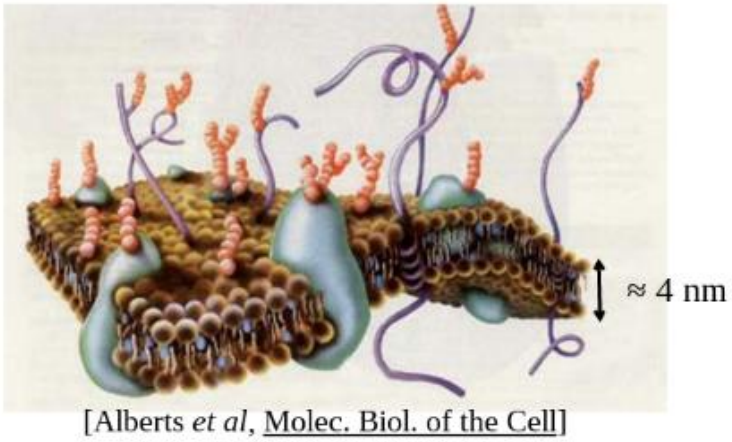

Figure 1.1: Artist Depiction of Cell membrane featuring lipids and proteins.

Three-dimensional schematic drawing of a cell membrane. The small molecules with round head groups and tails pointing toward the inside of the membrane are lipid molecules and compose the bulk of the membrane structure. The larger molecular structures are various proteins that bind to or imbed themselves within biological membranes. Lipids and proteins work in tandem forming the cell membrane which provides shape, structure and performs vital functions crucial for the survival of the cell. This image was reproduced from Alberts, *et al*, [B. Albert *et al*, Molecular Biology of the Cell, New York, Garland Science (2002), 4th Edition]. [12]

Section 1: Binding and envelopment of spherical nanoparticles

Deformations of a membrane due to the binding of particles (proteins, viruses, nanoparticles, etc.) are characterized by a competition between the favorable reduction in free-energy due to adhesion and the cost of deforming the membrane. The equilibrium state of the

system is determined by minimizing the total energy while accounting for adhesion and bending. For large particles or many-particle systems tension also contributes an energetic cost opposing binding that must be considered. Typically, the membrane is described as a continuous elastic sheet.[13,14,15] For small particles molecular interactions are important and simulations are used to investigate translocation through and incorporation within the membrane.[16,17,18,19] For the purposes of this investigation the continuum model will be utilized, since in the literature it appears to work well to nanometer scale curvatures. The exact shape of the membrane due to the binding of particles is nontrivial. The shape depends on many different parameters including membrane stretching energy, [13,20] membrane tension,[21] particle geometry,[22,23,24] contact energy,[13,20] and spontaneous curvature of the membrane.[13,25,26] Using particles of a specific geometry is a powerful method to explore the role of geometry, as it defines the shape of the membrane enveloping the particle. If one knows the shape of the membrane, then the Helfrich model can be used to find the deformation energy per unit area of the membrane which, for the case of zero tension, is described by

$$e_{bend} = \frac{1}{2}\kappa(c_1 + c_2 - c_0)^2 + \bar{\kappa}c_1c_2 \quad (1).$$

where c_1 and c_2 are the principle curvatures and c_0 is the spontaneous curvature of the membrane. The sum of c_1 and c_2 is the total curvature and is denoted as K (which is twice the mean curvature). The product of c_1 and c_2 is the Gaussian curvature denoted by K_G. The membrane bending modulus is denoted as κ, and the saddle splay modulus or curvature modulus is, $\bar{\kappa}$. Making these substitutions we get the following expression.

$$e_{bend} = \frac{1}{2}\kappa(K - c_0)^2 + \bar{\kappa}K_G \quad (2).$$

In our experimental system, we can simplify this further by estimating the spontaneous curvature of our membrane as zero. This is reasonable since the membrane composition should be very nearly symmetric and the spontaneous curvature of the membrane should be much smaller than the curvature of the particle. The Gaussian curvature term can also be neglected if we assume no topological changes.[13] We can again rewrite the bending energy as.

$$e_{bend} = \frac{1}{2}\kappa K^2 \quad (3).$$

By inserting the total curvature of a sphere into the expression above we can find the bending energy required to deform the membrane around the spherical particle. Next, we balance the energy required to deform the membrane against the binding energy of the particle to the membrane and in doing so can determine critical conditions for when envelopment occurs and what physical parameters dominate the system. Here we define the adhesion energy per unit area to be, ω, the particle radius, a, and the membrane tension, σ.[15] For a single spherical particle this is predicted from the Helfrich model of membranes.[13,27,28] Comparing the different energetic contributions from adhesion, bending and tension, the following critical particle radii characterize the membrane-particle interactions,

$$a^* = \sqrt{\frac{2\kappa}{\sigma}} \quad \text{and} \quad a^{**} = \sqrt{\frac{2\kappa}{\omega}} \quad (4).$$

The first of these two critical radii, a^*, compares the bending energy with the membrane tension and thus characterizes the crossover between the bending-dominated ($a \ll a^*$) and tension-dominated regimes ($a \gg a^*$). Cell membranes have a typical tension of 0.01-0.3 mN/m[29,30] resulting in a value for a^* in the 10-100 nm which is similar to the sizes observed for proteins. It is this condition that motivates us to look at the interactions of nanoparticles and lipid vesicles as a good model for this system. For lipid bilayer membranes, nanoparticle binding typically results in small

a^* values and a^{**} values that range from a^*/a <<1 to >>1. The nanoparticles thus fall within the bending-dominated regime. Micrometer-sized particles result in a value of a*/a that is not small, and tension plays a dominate role. Within the bending-dominated regime, particles with $a<a^{**}$ will remain unwrapped while larger particles are completely wrapped.[13,31,32,33] This expression can be rewritten to provide the threshold adhesion strength required to fully wrap a particle of radius, a, where equality refers to the case of zero tension (see figure 1.2),[34]

$$\omega_0 \leq \frac{2\kappa}{a^2} \quad (5).$$

Theoretical calculations and simulations,[13,27,35,36,37] as well as experiments support this picture.[14,38,39,40], as do the results reported in Ch 3 of this thesis. The inclusion of nonzero tension shifts this transition to higher values of ω.[13] Additionally, for nonzero tension or tension that is not small compared to the dimensionless combination in equation (1) there exist stable partial-wrapped states that are separated by a continuous transition from unwrapped states and by a discontinuous transition of the energy to the completely wrapped state. The complete wrapping threshold can also be shifted when considering the interactions of many nanoparticles. Simulation studies with three or more particles[41] as well as with non-spherical particles[31] show this transition can be shifted to lower values of ω.

This line of reasoning can be utilized to define a dimensionless parameter that describes the particle adhesion,

$$\gamma := \frac{1}{a}\sqrt{\frac{2\kappa}{\omega}} \quad (6).$$

Adhesion can be driven by a number of interactions including van der Waals interactions,[39] hydrophobic interactions,[42] electrostatic interactions,[43] and adhesion via receptor-ligand

bonds.[44,45,46,47,48,49,50] Typically, in these systems, adhesion is modeled to be continuous and homogeneous. Values for the bending rigidity are typically $20k_BT < \kappa < 100k_BT$, and membrane tension is $0.05\ k_BTnm^{-2} < \sigma < 20\ k_BTnm^{-2}$,[13,51] and adhesion strength is typically $2 * 10^{-6}\ k_BTnm^{-2} < \omega < 0.2\ k_BTnm^{-2}$.[52] In our experiments we utilize electrostatic interactions to induce particle binding. To achieve this binding, we varied the amount of DOPC, DOPS, and DOTAP lipid in the membrane. DOPC is zwitterionic (containing a charge dipole in the phosphocholine headgroup) and has been found to support adhesion of both anionic and cationic particles, of which more discussion included below. DOPS is anionic with a phospho-L-serine head group and DOTAP is cationic with a trimethylammonium-propane headgroup. Both lipids are used to dope the base DOPC membranes according to the desired charge density. All three types of lipids share the same 1,2-dioleoyl-sn-glycero-3 "DO" unsaturated tails to keep the lipids in the liquid disordered phase at room temp.

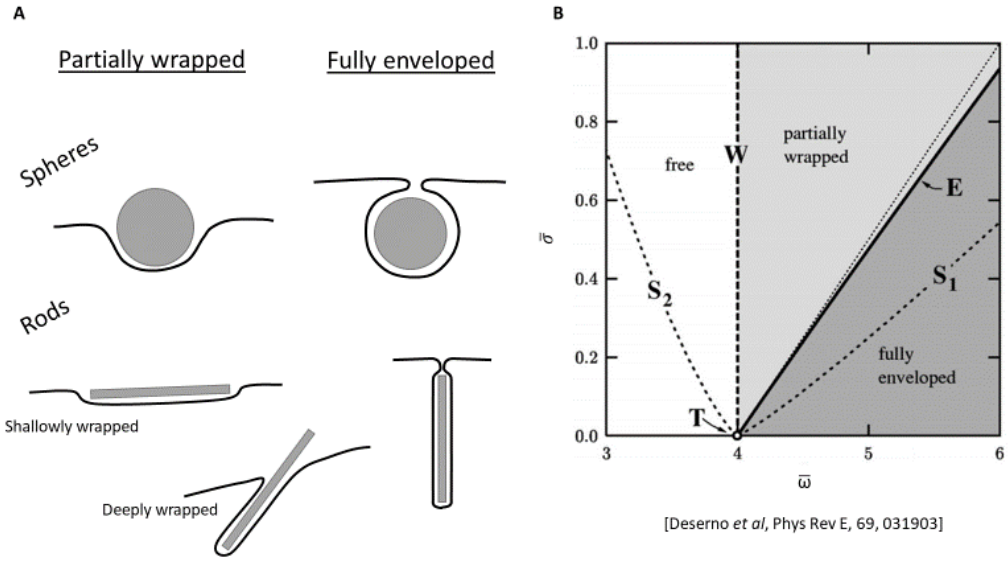

Figure 1.2: Wrapping configurations for spherical and rod-shaped particles

(A) Illustration of the partial and complete wrapping states of nanospheres and nanorods.[31] (B) Wrapping phase diagram in the plane of reduced adhesion constant (horizontal axis) and reduced lateral tension (vertical axis). There are three distinct states; free, partially wrapped and fully enveloped. For the case of zero tension we observe a triple point where the particle goes directly

from free to fully enveloped for sufficiently high reduced adhesion constant. The dashed line W marks the continuous transition at which partial wrapping sets in. The bold solid line E indicates the discontinuous transition between partially wrapped and fully enveloped. The S1 and S2 are the spinodal belonging to E. The fine dotted line close to E indicates where the fully wrapped state has zero energy.[13] The plot of (b) is copied from [Deserno et al, Phys Rev E, 69, 031903].

Section 2: Non-spherical nanoparticles on lipid membranes

Next, we consider non-spherical particles. Most of the physical arguments made for spherical particles still apply and interactions are still dominated by bending and adhesion for non-spherical nanoparticles. Now, however, particle shape and orientation determine the membrane deformations. Rather than just the particle radius for spheres, for more general shapes the inhomogeneous surface curvature of particles will correspond to energy barriers for wrapping.[31,53,54,55] Unlike spherical particles non-spherical particles can have stable partial wrapped states even at zero membrane tension. Size, aspect ratio, particle orientation and local particle surface curvature govern the wrapping of non-spherical particles.[31,53,54,55]

Elongated particles like ellipses and rods can be oriented parallel or perpendicular to the membrane so as to minimize the free energy of the system. The preferred orientation of an elongated particle bound to the membrane depends on the particle's shape, the membrane elastic properties and membrane-particle interactions. Elongated particle-membrane interactions are more complex than those of spheres, and this point is made readily apparent in the case of particle's envelopment. For rod shaped particles, the region of the membrane where it returns to the far-field shape costs energy that is not paid for by adhesion.[31,37,56] This is not the case for spheres since the far-field shape of the membrane is a catenoid, a minimal surface (with zero total curvature). One can however approximate the far-field shape of non-spherical particles as a catenoid in the case of full envelopment if the rod is oriented normal to the plane of the interface. This depiction is accurate and not an estimate for rods with hemi-spherical ends.[13,31]

For rod-like particles, energy minimization predicts three binding states; shallowly wrapped, deep wrapped and completely wrapped.[13,31,57] For very small adhesion strengths, energy minimization predicts they readily bind with their length perpendicular to the membrane. For rods with small aspect ratios (length/width less than 2)[31] they will remain in this orientation until they reach the completely wrapped state. Increasing the adhesion energy causes the rods to transition from shallow-wrapped to deep-wrapped and from deep-wrapped to completely-wrapped, both transitions are discontinuous.[31,58]

Rods can bind perpendicular or parallel to the membrane depending on energy minimization and during a dynamic engulfment process can transition between these two orientations. For example, simulation results demonstrate that for high aspect ratios or round edges rod-like particles will bind first perpendicular then rotate to be parallel to the membrane for the shallowly wrapped state.[31] If the adhesion strength is increased, the rods will again rotate to be perpendicular to the membrane in the deep wrapped state. No matter the dynamics, however, all deep-wrapped states are perpendicular to the membrane, as shown in figure 1.2 a.[31,58] Experimental observations of budding filamentous viruses agree with this theoretical prediction.[59,60] Dynamic simulation can also be used to calculate the reorientation dynamics for elongated particles on lipid bilayer membranes.[58,61] One way of doing this is by analyzing the local free energy of the membrane-particle system and then incrementally changing the nanoparticle orientation toward the lowest energy configuration.[58] Doing so allows one to determine the most likely wrapping pathway. A convenient way to characterize the wrapping states of the various particle geometries is to create a wrapping diagram based on energy minimization this is analogous to phase diagrams in thermodynamics.[13,31,62] With such an analysis one can easily predict what the anticipated

binding configuration of a particle will be and determine the tunable parameters capable of transitioning the particle between states.

Section 3: Membrane mediated interactions of many particle systems

This description is vastly more complicated when considering multiple particles since deformations in the membrane caused by individual particles are not additive. The computational labor to compute the membrane shape due to the deformation of just two particles is cumbersome but progress has been made in this area. Modeling membrane shape can be simplified by describing the membrane-particle interactions using an effective contact angle. The contact angle is defined as the angle between the membrane and the plane that contains the particle rim. Local curvature dictates the contact angle, and at equilibrium the local curvature is constant. Work done by Deserno, *et al*., has numerically derived interaction potentials between two spherical particles absorbed on a membrane as a function of distance and contact angle.[20] For small contact angles it is predicted that particles with azimuthal symmetry will repel each other. For large contact angles these same particles experience a long-range repulsion and a short-range attraction (on the order of the diameter of the particle). Rod shaped particles were predicted to always repel.[13]

Simulations done by Šarić et al. find that strongly adsorbed particles experience an effective attractive interaction over short distances resulting in hexagonal and linear aggregates.[63] This is confirmed by the simulation work of Bahrami, *et al*., that found not only an attractive interaction but also linear aggregates which protrude into the membrane.[64] Still other simulation efforts confirm the aggregation of nano- and microparticles on membranes in both linear and hexagonal aggregations.[36,65,66] Experimental work by Li et al. shows the migration of micron sized Janus particles on elongated vesicles. This particle migration is dependent on high membrane

tension.[67] In the low-tension regime work by van der Wel et al. shows that strong wrapping leads to attractive forces.[39] There is a lot of evidence for membrane mediated attractive interactions for strongly bound particles. However, there are few experiments to test these findings in physical systems.

The problem becomes increasingly difficult when one tries to extend these calculations to the realistic hundreds of particles seen in biological phenomena. This is where simulation and experimental work are needed to help drive progress in the understanding of such interactions. Indeed, many-particle (or virus) experiments and simulations have been conducted and show intriguing and potentially useful cooperative particle interaction mediated by the membrane. Experiments have shown that membrane mediated interactions between particles have led to: cooperative particle dynamics, attractive interactions between particles,[39] clustering,[64,65] tubulation of the membrane,[68,69,70,71] and internalization of particles.[14,38] Similarly, simulation and calculation have found hexagonal and chain-like aggregations,[61,66] budding or tubulation of the membrane,[15,20] and internalization.[35,45]

More work is needed to explore the wide range of phenomena observed in collective particle behaviors. Additionally, further research is required to be able to tune membrane shape for application or to understand how cell membranes function. The work described in this thesis adds systematic new studies and new insights to this body of knowledge. In doing so the hope is to be able to control morphologies of the membrane, providing a useful model of cell membranes, as well as opening the door to applications.

The following chapters will expand upon and address the topics presented in this introduction. Chapter two presents the methods and materials utilized to obtain the results reported in this document and provides details on protocols and specific techniques. The third chapter

presents results related to the binding of many spherical nanoparticle to lipid bilayer membranes and how the observed phenomena is related to the theory describing individual membrane-particle interactions. The fourth chapter present a similar study done with nanorods and expands upon the techniques utilized to observed dependence on particle binding, membrane tension and particle concentration. The last chapter presents a summary of the results presented in this dissertation, provides context for their significance, and presents suggestions for future research.

CHAPTER 2

MATERIALS AND TECHNIQUES

Chapter two outlines the methods, techniques and materials used in the experiments presented in this thesis. The first section presents the lipids used, the reason for their selection and the process of GUV fabrication. The second section describes the particles used, the motivation for their selection and where the particles were sourced. Next, we describe in detail the chambers used for first, the spheres experiments in section three and then upgraded microfluidic chambers constructed for the rod experiments in section four. Section five elaborates on the various microscopy techniques utilized in both the spheres and the rod experiments. Lastly, in section six we present details on the vesicle tracking software that was developed and utilized for vesicle destruction analysis.

Section 1: GUV Preparation – Electroformation

Lipid composition was selected carefully to ensure first that the membrane remained in the fluid phase for the duration of experiments and secondly to control the charge density of the membrane. Lipids with unsaturated (1,2-dioleoyl-sn-glycero-3 or "DO") tails were selected to keep the membrane in the liquid-disordered phase. Lipids with a variety of charged or polar groups were selected and combined to control the charge density of the membrane. For most of the experiments presented here the base lipid used to form GUVs was 1,2-dioleoyl-sn-glycero-3-phosphocholine (DOPC), which has a zwitterionic headgroup. We found that both positively and negatively charged particles bound to the DOPC membranes. [72] This seems surprising in view of findings that DOPC vesicles have a slightly negative electrostatic (zeta) potential of -9 mV

(electrophoretic mobility with 0.1 mM NaCl)[73] and might therefore be expected to repel negatively charged nanoparticles. We attribute the binding in this case to the static dipole of the zwitterionic PC headgroup, which can reorient to attract charged objects of either sign.[74] Previous experimental studies have also found that anionic particles were able to bind to DOPC vesicles.[75,76] When working with cationic particles we increased the interactions by doping the DOPC membrane with the anionic lipid 1,2-dioleoyl-sn-glycero3-phospho-L-serine (DOPS) to tune the adhesion of such particles to the membrane. Conversely, we used cationic 1,2-dioleoyl-3-trimethylammonium-propane (DOTAP) to control the adhesion of anionic particles to the membrane. To visualize the membranes when doing confocal microscopy, we added a small amount of headgroup-labeled lipid 1,2-dioleoyl-sn-glycero-3-phosphoethanolamine-N- (lissamine rhodamine B sulfonyl) (ammonium salt) (Rh-DOPE). For a few experiments we also used the anionic 1,2-dioleoyl-sn-glycero-3-phospho-(1'-rac-glycerol) (sodium salt) (DOPG) as well. All the above-mentioned lipids, DOPC, DOPS, DOTAP, Rh-DOPE and DOPG where purchased from Avanti Polar Lipids pre-dissolved in chloroform in ampules. Lastly a few experiments were conducted using lipids derived from soy lecithin powder (Phospholipon 85G) acquired from the American Lecithin Company. These lipids all have a phosphatidylcholine (PC) head group, but the length of the fatty acid tails varies. All lipids were stored under nitrogen in a -20°C freezer.

Once the appropriate combination of Lipids was selected, GUVs (10-100 μm diameter) were formed using electroformation. Electroformation also known as electroswelling is one of the most common methods for producing GUVs due to the techniques success in quickly producing reasonably monodisperse, defect-free vesicles. The method was pioneered by Angelova and Dimitriov in 1989,[77] and later studied in detail by Herold *et al.*[78] GUVs are formed by modulating the spontaneous swelling of lipids in an aqueous solution via the application of an external electric

field. In our application we used indium tin oxide (ITO, from Delta Technologies, Part # CB-50IN-S111) glass cover slips as our substrate to apply the thin layer of lipids. The coverslips had a conductive copper tape (from 3M, sold by SPI, part # 5012-AB) applied to one end on the conductive side of the glass to help with the attachment of electrodes during the electroformation process (Fig. 2.1a).

The first step in the process of electroformation is to clean the glass slides using acetone and a Kimwipe. Next the lipid solution was prepared by carefully combining the desired ratio of base lipid (typically DOPC) with doping lipid (DOPS, DOTAP, etc.). The total volume of fluid was around 50 μl. The lipids were mixed thoroughly by first agitated the fluid by extracting and expelling with a syringe 20 times and then vortexed for 1 minute to ensure homogeneity among the resulting vesicles. Lipids were then deposited on two coverslips being careful to spread the lipids evenly over the surface of the slide with the tip of a syringe. The coverslips were dried in a vacuum chamber for at least two hours to remove all chloroform solvent leaving only a few thin layers of lipid on the ITO slides.

During the drying process, the hydrating solution was prepared. For the experiments outlined in this document all vesicles were prepared with the same 175 mOsm/L sucrose for hydration. Later, after vesicle formation,180 mOsm/L glucose solution was used to dilute the vesicle suspension, as described below. Experience showed this combination to reliably produce high quality vesicles. The two different solutions were selected to help provide contrast in the visualization of the vesicles via bright-field microscopy and promote the sedimentation of the vesicles. The difference in osmolarity made for slightly floppier vesicles which were less prone to bursting and easier to handle using micropipette aspiration.

After the ITO slides have finished drying, they are removed from the vacuum chamber and the slides are combined with a Teflon spacer and the sucrose solution to form a chamber for the hydration and electroformation process. The Teflon spacer is custom designed to be the same length and width as the glass slide and when sandwiched between the two glass slides forms a close chamber that can hold the sucrose solution (Fig. 2.1a). The Teflon spacer is coated with vacuum grease and set between the two glass slides lipid side inward. The spacer is secured using four small binder clips. Once secured a 22-gauge syringed is threaded through one of two small holes on the side of the Teflon spacer and the sucrose solution is deposited within the open cavity making sure to exclude all air (Fig. 2.1c). The holes are sealed with vacuum grease and the chamber is now ready for electroformation. Note during this process care is made to move quickly and minimize exposure of the dried lipids to the air to avoid oxidation.

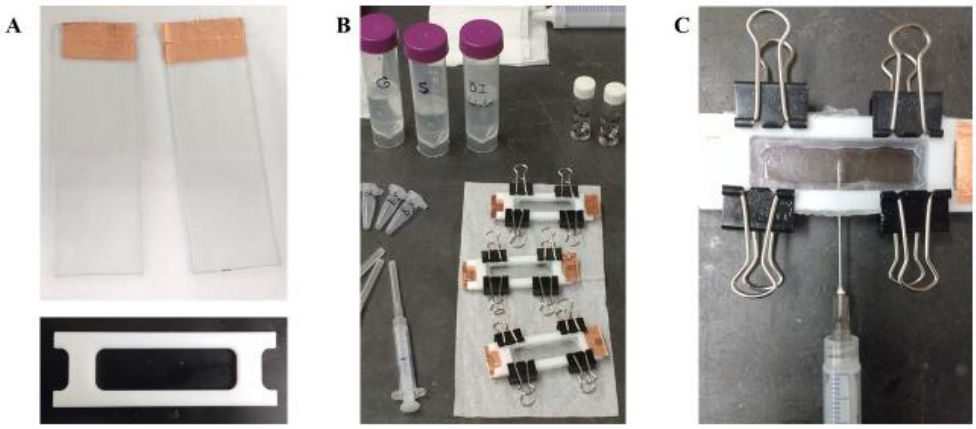

Figure 2.1: Electroformation chambers

Shows photographs of the different components used in the assembly of the electroformation chamber. (A) The top images show the ITO slides used; the bottom shows the Teflon spacer. (B) shows three fully assemble chambers, the syringes for extraction, prepared glucose and sucrose solutions and storage containers. (C) shows a close up on the fully assembled chamber and how the syringe threads into the chamber via wholes on the side.

The chamber is then placed in an oven which has been preheated to 50°C. As the chamber is placed in the oven two alligator clips are attached to the glass slides one on each slide opposite

each other where the copper tape has been applied. The alligator clips are connected to a function generator which applies the external electric field essential to the electro formation process. The function generator should be set at a 2.4 peak-to-peak voltage, with a sine-wave oscillation at 100 Hz. The vesicles form in the solution over the course of two hours. Once finished the chambers are removed from the oven and the vesicles removed from the chamber by withdrawing the solution within the chamber out through the same holes the original solution was introduced. Movements should be slow without any sudden accelerations when extracting the solution (30 s) to not rupture the vesicles. The vesicles are then deposited in an Eppendorf tube and combined with equal parts glucose solution. The vesicles should be allowed to sediment to the bottom of the tube overnight and are stable for about a week.

Lastly, the ITO glass slides should be thoroughly cleaned by rinsing with acetone and de-ionized water repeatedly until spotless upon inspection against a bright light. Avoid washing with detergents as any residue will prevent the formation of vesicles. This is not only a courtesy to others using the glass but also essential for successful vesicle formation as a dirty slide will ruin a batch.

Section 2: Particles

For the experiments outline in this document two classes of nanoparticles were utilized: spherical and rod-shaped. Among the spherical particles the one most utilized were the cationic gold nanospheres made by YiWei Lee and Li-Sheng Wang in Vincent Rotello's group (Dept of Chemistry, University of Massachusetts Amherst). The cationic nanoparticles have a gold core functionalized with surface ligands consisting of a thioalkyl tetra(ethylene glycol)ated trimethylammonium (TTMA) ligand.[79,80] The tetra(ethylene glycol) spacer was added to keep the

particles stable in suspension. Particles were synthesized using the Brust–Schiffrin two-phase synthesis method[81] and then functionalized with TTMA ligands via place exchange reactions.[82] The core diameter was 2 nm (transmission electron microscopy), the hydrodynamic diameter was 6.7 ± 0.4 nm (dynamic light scattering, DLS), and the zeta potential in suspension was 18.2 ± 0.8 mV (electrophoretic mobility).[79] The ligand coating on these spheres was dense and uniform allowing for even charge density and the distribution on sizes was narrow. The even charge density comes from the permanent positive charge on the quaternary ammonium group at the ligand terminus. The particles were strongly dissociated and not sensitive to pH. These properties made them ideal candidates for the core of our exploration of GUVs with nanospheres.

To expand upon and confirm that our results where not dependent on the material, functionalization, or lipid composition our analysis was extended to other types of spheres. Anionic silica particles, Ludox AS-30 and Ludox SM (Sigma-Aldrich) were selected. The mean particle radii were a = 11.3 nm and 12.6 nm, respectively (DLS, measured in the same solution conditions as our vesicle experiments). Additionally, 30 nm diameter gold spherical nanoparticles (Aldrich) stabilized in a suspension of citrate buffer were explored briefly in a few experiments. Lastly the use of large patchy micro sized particles was explored. The particles were synthesized by Zhe Gong from the group of Prof Stefano Sacanna (Dept Chem, New York University). The particles were 2.5 μm in diameter with a cationic matrix and anionic patches. The bulk of these patchy particles are composed of amidinated polystyrene (PS). The patches of the particles are anionic 3-(Trimethoxysilyl)propyl methacrylate (TPM). The entire surface is coated in triblock copolymer Pluronic F108 to the particles to further stabilize. The particles are then suspended in a 0.5%wt. F108 aqueous solution. The particles were chosen due to their heterogenous binding to the membrane preventing them from being fully enveloped. They could then be used to track

diffusion on the membrane with and without nanoparticles present.[83] All nanospheres were stored at 2-8°C.

A variety of nanorods were utilized in the experiments outline in this document. The primary rod used was an anionic DNA origami nano rod designed by Masha Siavashpouri (Dept. Physics, Brandeis University) and then modified and synthesized by Thomas Gerling (Dept. Physics, Technical University of Munich). The rods are formed from six-helix DNA-bundles that are 420 nm by 6 nm with single basepair insertions every 42 bases per helix resulting in a global right-handed twist (360 degrees). The reaction mixture contained homemade p7560 scaffold DNA at a concentration of 50 nM and oligonucleotide staple strands at 200 nM each (purchased from IDT). The folding buffer included 5 mM TRIS, 1 mM EDTA, 5 mM NaCl (pH 8), and 20 mM MgCl2. The reaction mixture was subjected to a thermal annealing ramp using a Tetrad (MJ Research, now Bio-Rad) thermal cycling device. After a 15-minute thermal denaturation step at 65°C, the mixture was annealed from [60 - 20°C] for 60min/1°C. The reaction mixture was purified from excess staple strands by performing one round of PEG precipitation.[84] The resulting pellet was dissolved in folding buffer (5 mM tris, 1 mM EDTA, and 5 mM NaCl) including 5 mM MgCl2. The final volume was chosen to get a monomer concentration of 150 nM. The sample was equilibrated at 40°C and 450 rpm overnight in a shaker incubator (Thermomix comfort from Eppendorf).

The rods were specifically designed with strategically placed additional thymidine groups and then exposed to ultraviolet light which induces cross-links between adjacent thymidines to increase the structural integrity at low ionic strength conditions.[85] To this end, every staple terminus and every staple crossover features two additional, unpaired thymidines. For UV irradiation, we used a 300-W xenon light source (MAX-303 from Asahi Spectra) with a high

transmission bandpass filter centered around 310 nm (XAQA310 from Asahi Spectra). We used a light guide (Asahi Spectra) to couple the light into the sample by placing it directly on top of an open 0.65-ml reaction tube and irradiated the sample for 70 minutes in an ice bath (~16 mW/cm2). To reduce aggregates in the PEG purified sample, we spun the sample for 20 minutes at 21,000 rcf (relative centrifugal force) and 4°C and kept the supernatant. Finally, to decrease the amount of PEG molecules in solution, we performed four rounds of ultrafiltration (Amicon Ultra 500 µl with 100k cutoff). Ultrafiltration was carried out at 20°C and 14k rcf (Eppendorf 5424R) with folding buffer (5 mM tris, 1 mM EDTA, and 5 mM NaCl; including 5 mM MgCl2). The final concentration of the sample was adjusted to 150 nM. All procedures were performed as previously described.[86] From this stock solution rods were diluted using the same sucrose and glucose solution used to create and dilute the vesicles. The specific concentration is denoted per experiment.

Prior to the updated design of the DNA origami nanorods to include strategically placed additional thymidine groups unmodified versions of the DNA origami nanorods were utilized. They were found to disintegrate under the low ionic conditions required for experiments looking at the charge interactions between lipids and nanoparticles and thus the modifications were required. These other DNA origami nanorods include four varieties of six-helix DNA-bundles rods: 415 nm length with 360 degree left handed twist, 295 nm with 360 degree left handed twist, 243 nM with no twist, and 326 nm wit 720 degree right handed twist. All the rods were in the same buffer: 250mM NaCl and 20mM tris base ph8.[87]

Lastly a few experiments where done using the rod-shaped mutant type of the filamentous bacteriophage fd wild-type virus, fd-Y21M. This “rod” like virus was produced by Marc Ridilla and Zhenkun Zhang (Brandeis University, MRSEC) and could be produced in both anionic and

cationic varieties. The viruses are 800 nm long by 5 nm and consist of a single-stranded circular DNA molecule coated with a protein layer.[88,89]

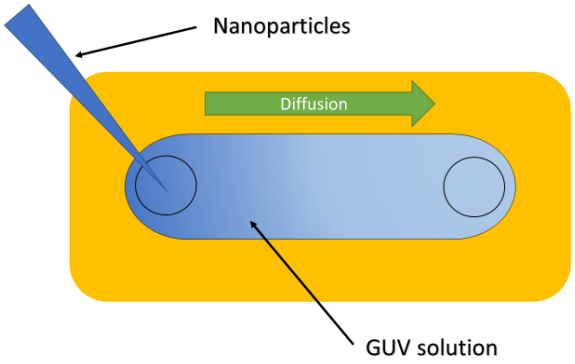

Figure 2.2: Prefusion chambers

Illustration of perfusion chamber used for imaging the dynamics of nanoparticle/vesicle interactions.

Section 3: Perfusion chambers

In preparation for an experiment the first step was to dilute the nanoparticles in the same solution as the GUVs. For example, in the case of experiments with the TTMA gold nanospheres 2 μL of stock nanoparticle solution (10 mM nanoparticles in H_2O) was diluted with 10 μL of 175 mOsm/L sucrose and 10 μL of 180 mOsm/L glucose. By doing this we dilute the nanoparticles to the desired concentration as well as balance the osmolarity of the particle solution to the GUVs to prevent osmotic shock. The nanoparticle/sugar solution was vortexed for two minutes at a high speed to ensure even mixing, then sonicated for 90 seconds to break apart any aggregates. The GUVs were also prepared prior to observation by taking 5 μL of concentrated GUV solution and dispersing it in 10 μL of 175 mOsm/L sucrose and 10 μL of 180 mOsm/L glucose. The solution was then mixed gentle using the end of a pipette tip.

The process of mixing vesicles and nanoparticles was monitored in situ using optical microscopy so that the early stages of adsorption could be visualized. To this end, we first added vesicles into a long, narrow perfusion chamber (CoverWellTM; Grace Bio Labs, with #1½ cover glass). The perfusion chambers allowed for clear visibility, were easy to load and were reusable. See Fig. 2.2. We then placed the chamber on the microscope and waited a few minutes to allow the vesicles to settle onto the coverslip. Next, we added 5 μL of nanoparticle suspension (approx. 1 mM of nanoparticles plus approx. 178 mOsm/L of glucose + sucrose with osmolarity checked) into one end of the perfusion chamber. (In some experiments, the nanoparticles were suspended in 180 mOsm/L of glucose + sucrose; these samples were not distinguishable from the others.) Particles then diffused further into the sample. This method allowed observation of the vesicles as the nanoparticles bound. Vesicles that were farther from the point of nanoparticle addition had a lower nanoparticle concentration.

This same procedure of preparation and then observation was used for the other spherical particle experiments and some nanorod experiments as well. Each experiment diluted the nanoparticles to the desired concentration using the same solution the GUVs were suspended in (equal parts sucrose and glucose). For experiments with added NaCl, GUVs and nanoparticles were diluted in a solution of sucrose, glucose and NaCl where the ratios were selected to maintain matching osmolarity with the interior of the vesicles while varying the amount of NaCl and thus free ions in solution. The primary purpose for diluting the GUVs beyond experiments including NaCl was to prevent overcrowding. No matter the preparation, nanoparticle and GUV solutions were combined *in situ* and interactions observed. Specific experimental conditions are outline as they are relevant in later chapters.

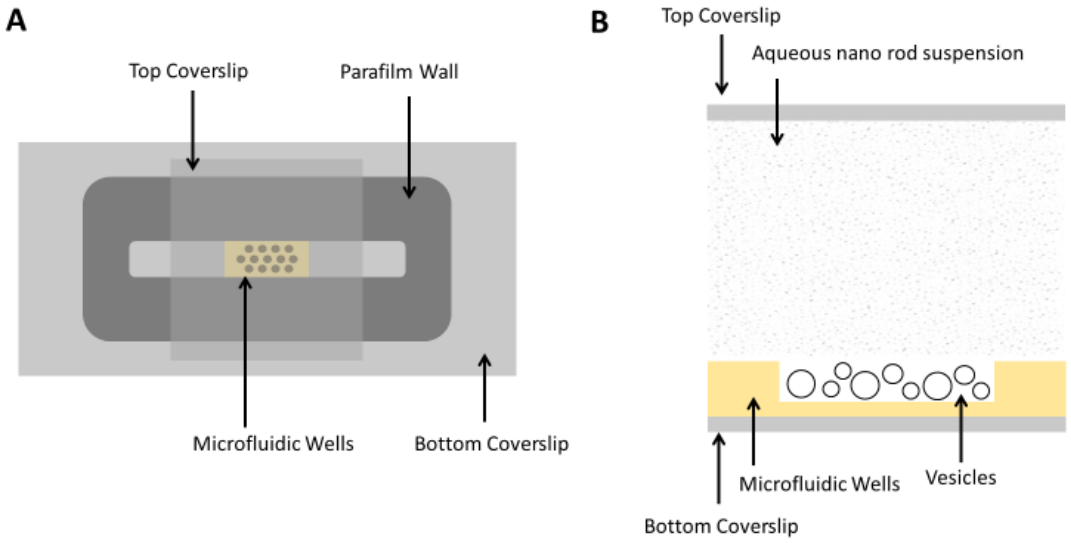

Figure 2.3: Microfluidic chambers

(A) Top view of the microfluidic chambers used for imaging the dynamics of the nanoparticle/vesicle interactions. (B) Side view of a single well.

Section 4: Microfluidic chambers

The primary drawback to the perfusion chambers used in experiments with spherical particles is the lack of control of the concentration gradient of particles and their mixing with GUVs in the sample chamber. To address this issue and expand our experimental capabilities custom microfluidic devices were designed and fabricated with the help of Maria Eleni Moustaka of Seth Fraden's group (Dept Physics, Brandeis). These devices enable the confinement of the GUVs to microwells at the bottom of the chamber. This confinement allowed for a rapid full exchange of the volume of the chamber without drastically disrupting the vesicle. Additionally, the confinement of the vesicles allowed for easy long-term tracking of multiple vesicles over the course of the experiment. This was not possible with the perfusion experiments which suffered from a large amount of fluid flow. GUV and nanoparticles solutions were prepared in the same

way as is outlined in section 3. Specific concentrations of nanoparticles and osmotic conditions are denoted where relevant in Chapter 4.

The first step in making the microfluidic chambers was designing the micro wells using Autodesk AutoCAD® and then sending the photomasks out to be printed commercially (Front Range Photomask Co. LLC). The dry photoresist photolithography technique described by Khalkhal *et al.*[90] was used for the fabrication of the photoresist masters. Specifically, we used stainless steel wafers with 3'' in diameter and 0.0293'' thickness supplied by Stainless supply. The dry photoresist films are the DuPont Riston dry-film photoresist GM120 with thickness 50 μm. Lamination was performed with the Fellowes Saturn 2 95 Laminator at 150 °C. After aligning the photomask on the wafer with the dry photoresist layer, we UV-exposed it with a UV lamp (UVP 8W UVL -28) for 30 minutes. The master was developed in a bath of potassium carbonate 10g/l, under a fume hood. For casting the microfluidic device, we used 10-15 g of PDMS (Dow Corning SYLGARD® 184 Silicone Elastomer Kit) with 10:1 base and cross linker ratio mixed with a centrifugal mixer (Heraeus Labofuge 400) at 1000 rpm for 6 minutes. After depositing the PDMS layer on the master, we degas the PDMS for 10 minutes in a vacuum chamber until all bubbles are removed. We then placed a 25 mm x 75 mm thin plasma-cleaned glass slide on top of the master with the PDMS substrate and both bottom and top surfaces were covered with a sheet of Mylar® and a thermal Kapton sheet. For plasma cleaning the glass slide, we used the Jelight UVO-Cleaner model #42. For curing the PDMS we used a thermal press (Dulytek DM1005) and we pressed for 2 hours at 70°C, hand tight. When curing was completed, we carefully separated the final microfluidic device from the master. To create the flow chamber micro-wells were placed carefully on top of a large glass coverslip. Then parafilm spacers were placed around the microwells and lastly a small cover slip was placed on top of the spacer leaving a gap at each end

of the channel to allow for fluid to be flowed in and out of the chamber. This setup was thermally sealed, and no leakage was observed. The final fluid volume of the chamber was about 20 μL while the volume of an individual well varied from 3-30 nL. Figure 3.3 shows the structure of the final microfluidic device.

The process of combing vesicles with nanoparticles was monitored *in situ* using optical microscopy so that the full dynamics of the process could be observed. The bottom of the wells was only a few microns thick, thin enough to easily view through the bottom of the optically clear PDMS wells. The walls of the wells were fifty microns tall allowing for the confinement of one or two layers of vesicles. Any vesicles stacked too high in the well were washed away when the bulk fluid was exchanged. The micro wells were roughly circular in shape with a diameter ranging from 300-900 μm (Fig. 2.3). Vesicles were injected into the chambers and then allowed to sediment into the PDMS wells at the bottom of the chamber. Once the vesicles had sedimented the bulk fluid of the chamber, 20 μL, was replaced with a solution at the relevant concentrations required for specific experiments. The whole chamber was mounted to an optical microscope and interactions were observed from beneath.

Section 5: Microscopy of GUVs

Samples were viewed using a variety of microscopy techniques each providing a unique probe into our experimental system. The techniques used include: brightfield, darkfield, confocal and transmission electron microscopy. Numerous objectives, condensers and cameras were also utilized as was required for each of the microscopy techniques or experimental setups. Specific cameras used in each experiment are denoted within the chapters those results are reported.

Brightfield microscopy is a standard and simple technique where in the sample is illuminated producing an image where the sample appears dark against a bright background. Darkfield microscopy is a technique where light is shown at a wide angle such that the path of the light from the condenser does not pass through the objective unless it has scattered off of an object in the sample plane. The resulting images shows the sample as bright with a black background. Brightfield is easy to implement and provides good resolution. Darkfield, though more difficult to implement, provides higher contrast as well as being a direct measurement of the relative amount of material in the sample plane. Brightfield was utilized to observe the bulk behaviors of both spherical and rod-shaped nanoparticles as they interacted with GUVs. Darkfield was employed to observe the increase in intensity on the GUVs as particles accumulated on the membrane. Both techniques have the advantage of not requiring any additional tags, dyes, or labels to image the system which could interfere with the resulting interactions.

Confocal microscopy is an optical imaging technique that uses the excitation of fluorescent dyes to image a sample. The technique works by focusing laser light of a specific wavelength to a small point on the sample plane and then scanning that point across the full area of the region of interest. The laser then excites the florescent label in the sample (which is selected to fluoresce when excited by a specific wavelength of light). The excited light is then observed via an objective by a camera and the image is rendered. The advantage of this technique is the high-resolution imaging that is possible. The resolution far surpasses that of traditional brightfield microscopy and varies depending on the type of confocal utilized. The disadvantage of confocal microscopy however is the requirement of a florescent label. In the case of our experiments we utilized the labeled lipid Rh-DOPE. The addition of even a small amount of label can have dramatic effects especially when the interactions are on a nanometer scale.[91] To confirm that the effects observed

are not affected by the florescent label control experiments utilizing brightfield or darkfield are required. The use of confocal microscopy allowed us to get higher resolution images of the deformations caused by the binding of nanoparticles to GUVs.

Lastly, we consider Transmission Electron Microscopy or TEM. This is a highly advanced imaging technique that allows for ultra-high magnification images with resolution on the sub-nanometer scale. This is compared to the previously described techniques with resolution limits around a few microns to several hundred nanometers for confocal microscopes. Standard TEMs work by showering the sample with a beam of electrons of which those that are then transmitted through the sample form an image. It is the small wavelength of electrons compared to visible light that enable them to produce higher resolution images. The resulting image has a bright background where electrons freely transmitted and a dark sample where electrons interacted with or were blocked by the sample. The intensity values of the image are directly correlated to the thickness of the sample at that location. The disadvantage of electron microscopy is that it is difficult to do, requires highly advanced equipment and requires the sample to be put under high vacuum. The last issue is particularly egregious considering all our experiments are done in the aqueous phase and drying the sample would fundamentally alter the structure. To resolve this Cryogenic TEM was utilized. Cryo TEM is a technique where in the sample is plunge frozen preventing ice crystals from forming and resulting in amorphous ice. Amorphous ice is just H_2O in a solid disordered phase where the individual water molecules are frozen faster than they can organize into a crystalline structure. This is essential for preserving the structure of the sample prior to freezing and allows for a snapshot of the aqueous phase structure of the sample. The sample is kept in liquid nitrogen until it is viewed in the Cryo-TEM which continues to hold the sample at -180°C. This

highly advanced technique was used to view the nanoscale structures and interactions observed between spherical and rod-shaped nanoparticles and lipid bilayer membranes.

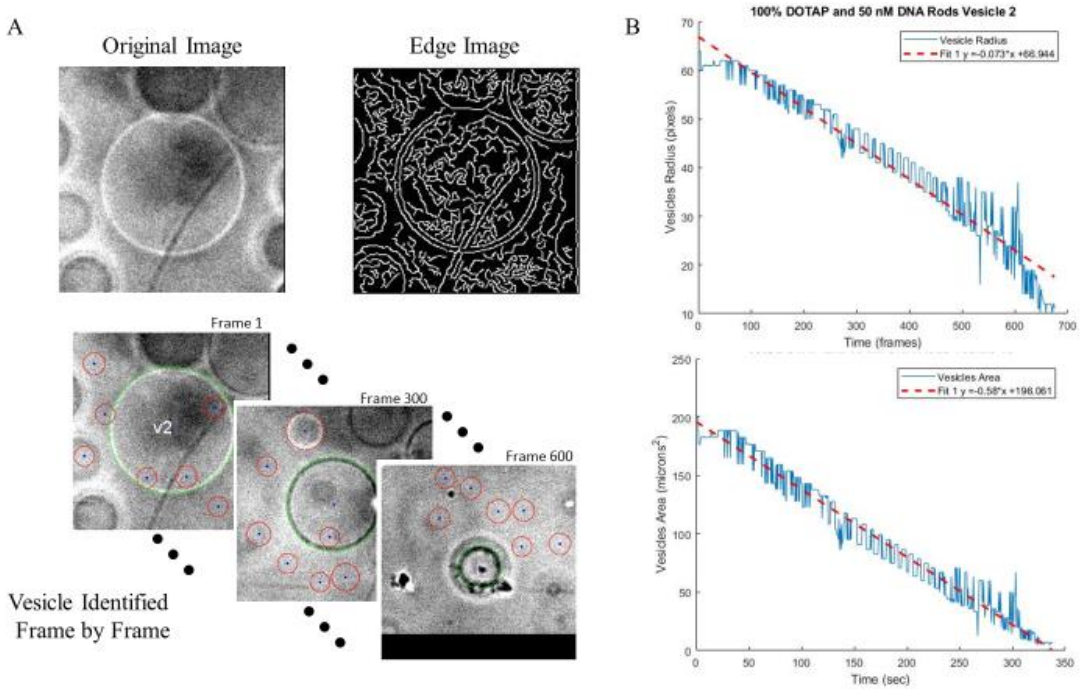

Figure 2.4: Vesicle tracking software

(A) Shows the analysis steps undergone during the edge finding and circular Hough transform. (B) The top figure shows the observed radius of the vesicles in pixels verses frames. The bottom plot shows the observed area of the vesicle verses seconds both fitted with a linear fit for comparison.

Section 6: Vesicle tracking software

The use of microfluidic chambers rather than perfusion chambers enabled the careful observation of numerous vesicles (20-100) over long periods of time (30-90 minutes). The typical frame rate for experiments presented was 2 frames per second. Dozens of vesicles observed over thousands of frames over dozens of individual experiments provided significant statistical observations. Something that has never been attempted in a dynamic GUV system on this scale. However, the immediate issue was how to manage the shear quantity of data. To tackle that issue, we implemented an image analysis technique known as the Circular Hough Transform[92] to track

individual vesicles during their life span in an experiment. This vesicle tracking software was developed specifically to measure the rate of size reduction observed during the destruction of vesicles induced by the binding of nanorods. This analysis can be extended and modified to apply to any system of circles where the size of the circle is desired.

The Circular Hough Transform (CHT) is a digital image processing technique used to detect circles in imperfect images. The method was more effective for viewing our low contrast images of vesicles that are often crowding each other or have debris floating past them. Our analysis works by first taking the original image, in our case a single frame, and transforming it into an edge image, see Fig. 2.4 a. An edge image is one that is completely black and white with black as the background and small amounts of white lines at the edges of the objects in question. In our analysis the Canny Edge detection method was used to transform our images. The edge image is then given to the transform as an input along with the range of radius required to search over. The method will scan the image for circles in the range of radius specified and identify the top ranked circle in the image. The analysis then outputs an image file with the top 8 circles traced in red and the top ranked one in green, (Fig. 2.4 a). It also returns the radius of the circle as well as the position of the center. This process is then iterated for each frame of the vesicle destruction track and a plot of the radius reduction is produced along with a linear fit of the rate, (Fig. 2.4 b). The results of this analysis are reported in chapter 4.

The full script along with related functions are included in the appendix. This analysis method was adapted from an open source project create by David Young in 2016.[93]

CHAPTER 3

THE EFFECT OF CHARGED SPHERICAL NANOPARTICLES ON LIPID BILAYER MEMBRANES

This chapter presents the results of work looking at the interaction of nanospheres with lipid bilayer membranes. The first section introduces the major scientific questions we seek to illuminate while also emphasizing potential applications. The second section outlines the methods and materials used to conduct experiments. Section three provides a full overview of the results. The final section provides discussion and concluding remarks on the work presented. This work represents a continuation and expansion of work conducted by Dr. Derek Wood during his dissertation studies. These results have been previously published and can be found in the journal Nanoscale, where both Derek and I are co-first authors.[72]

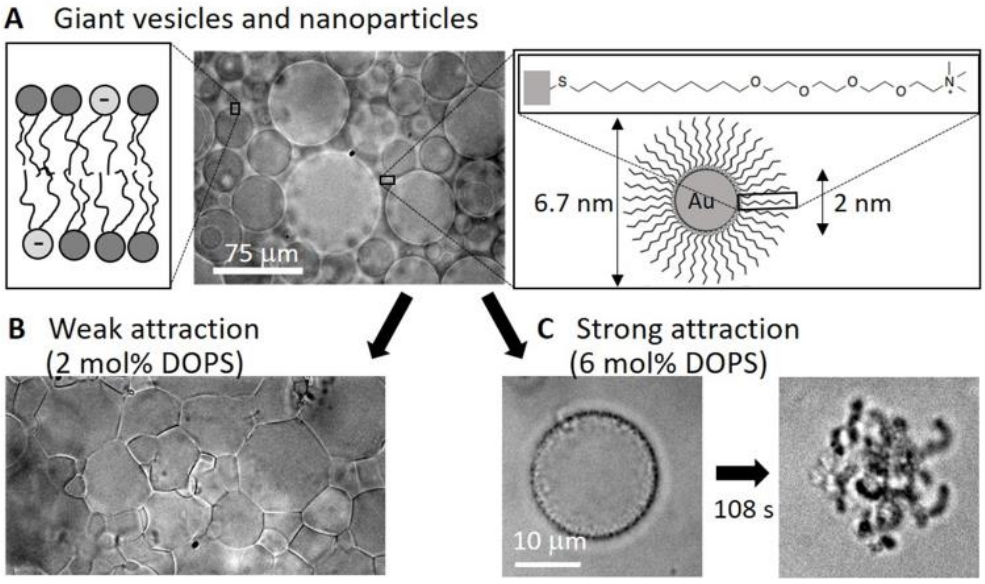

Figure 3.1: Schematic overview of spherical particle results

(A) Schematic overview of giant unilamellar vesicles (GUVs) with controllable anionic charge density exposed to cationic gold nanoparticles (Au-TTMA). The microscope image shows GUVs composed of 96 mol% DOPC and 4 mol% anionic DOPS without nanoparticles. (B) Microscope image of GUVs + nanoparticles that have adhered to one another forming a solid gel. (C)

Microscope images of a single GUV undergoing rapid tubule formation and destruction upon Au-TTMA nanoparticle binding. We also report similar behaviors for anionic nanoparticles with cationic vesicles.

Section 1: Introduction

Here we report the results of three different well-defined systems of lipid membrane and nanoparticles that allowed us to tune the interaction strength, ω, between the two components. We used giant lipid-bilayer vesicles (10–100 μm) with varied amounts of charged lipid to induce adhesion to oppositely charged nanoparticles. The majority of our studies focused on 6.7 nm-diameter cationic Au-TTMA nanoparticles (Fig. 3.1A).[79] We chose these particles because they have a dense ligand coating, are stable against aggregation, and have a permanent positive charge on the quaternary ammonium group at the ligand terminus. We made the vesicles with a mixture of zwitterionic DOPC and anionic DOPS, so that the molar ratio of DOPS could be tuned to set the binding energy per unit area, ω. When the DOPS fraction and ω were small, the nanoparticles caused the vesicles to adhere to one another and form a soft but solid gel (Fig. 3.1B). By contrast, when ω exceeded a threshold value, the vesicles were destroyed in a remarkably complex but highly repeatable process that included vesicle shrinkage, invagination, pore formation, runaway tubule formation, and possibly vesicle inversion (Fig. 3.1C). We also carried out experiments with negatively charged silica nanoparticles mixed with vesicles doped with positively charged DOTAP lipid and found similar results. With this silica system, we investigated two slightly different particle sizes and found that the threshold lipid composition was noticeably lower for the larger particles. Our computer simulations also showed a transition from partial to complete wrapping of nanoparticles and subsequent membrane rupture when the dimensionless ratio $\omega a^2/\kappa$ exceeded a threshold value of approximately 0.5. The sequence of morphologies leading to destruction was consistent in each case.

When a single nanoparticle, virus, or protein binds to a membrane, the adhesion can force the membrane to deform. Treating the membrane as a continuum elastic body, (see chapter one section 2 for more details) deformation is driven by free-energy reduction from binding and opposed by the free-energy increase from bending or stretching the membrane.[13,14,15] Defining the binding free energy per unit area of contact as ω, the radius of a spherical particle or virus as *a* and the membrane bending modulus[14] as κ, earlier theory work predicted a crossover from mild deformation to full wrapping of the bound object by the membrane when $\omega a^2/\kappa = 2.$[27,79] On the other hand, if the membrane were subjected to high mechanical tension, τ, this could play the dominant role instead of κ if the dimensionless ratio $\tau a^2/\kappa \gg 1.$[94,95] For lipid bilayer membranes having non-covalent interactions (*e.g.*, electrostatic double-layer), particles that are a few nm in size lead to $\tau a^2/\kappa$ values that are typically small, while $\omega a^2/\kappa$ can vary from $\ll 1$ to $\gg 1$. Therefore, for objects of this interesting size scale (which are relevant for biology and nanoparticle applications), deformations should be tunable via w and should range from weak adhesion to partial or full wrapping under common conditions. For individual particles, calculations and simulations[15,35,36,37,79] and experiments support the idea that $\omega a^2/\kappa$ is the key control parameter.[13,38,39,40]

When many particles or viruses are present, cooperativity leads to richer phenomenology. Experiments showed that cooperative interactions lead to in-plane attraction between particles[65] and particle clustering,[65,96] tubulation or pearling of the membrane[35,41,64,70,97,98,99,100] and internalization of particles within the vesicles.[13,37] Similarly, simulations and calculations found hexagonal or chain-like particle aggregates,[98,101] budding or tubulation of the membrane,[35,64,70,97,98,99,41,100] or internalization.[45,95] Despite the wide range of reported

phenomenology and theory, it is still not known how to predict and control these particle-membrane behaviors – especially when many particles are present.

The ability to tune the morphology and shape-changing dynamics of vesicles provides a useful experimental model of cell lysis and opens the door to new applications. These findings could be used to create cargo-carrying vesicles with the ability to rupture when bound particles are stimulated[11] or, potentially, when ω is tuned by an external trigger. These results also show how to engineer soft solid gels that can encapsulate cargo. They may also provide a unified picture for the wide variety of phenomena reported in cells and vesicles, which likely correspond to different regions of a phase space defined chiefly by ω, κ, a, and particle concentration.

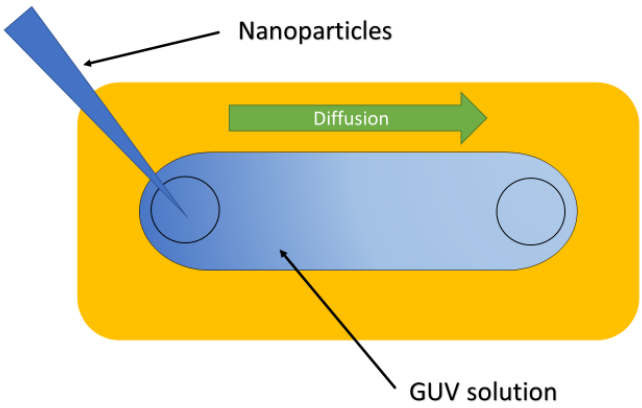

Figure 3.2: Perfusion Chamber

Top view of perfusion chamber used for imaging the dynamics of nanoparticle/vesicle interactions.

Section 2: Methods and materials

Giant unilamellar vesicles (GUVs) were prepared by electroformation using methods described in detail in Chapter 2 and in earlier publications.[78] The majority lipid was the zwitterionic mono-unsaturated 1,2-dioleoyl-sn-glycero-3-phosphocholine (18:1 DOPC; Avanti Polar Lipids). Charged lipids with the same fatty-acid tail (to suppress demixing) were added to induce particle

adhesion. Anionic 1,2-dioleoyl-sn-glycero-3-phospho-L-serine (18:1 DOPS; Avanti Polar Lipids) was added when using cationic Au-TTMA particles. Cationic 1,2-dioleoyl-3-trimethylammonium-propane (18:1 DOTAP; Avanti Polar Lipids) was added for experiments with anionic silica particles. In some cases, we added a small amount of headgroup-labeled lipid 1,2-dioleoyl-sn-glycero-3-phosphoethanolamine-N-(lissamine rhodamine B sulfonyl) (ammonium salt) (Rh-DOPE; Avanti Polar Lipids). All vesicles reported here were formed in 175 $mOsm\ L^{-1}$ sucrose solution and then diluted with an equal volume of 180 mOsm L^{-1}glucose solution, then left for a day to make the vesicles slightly floppy (so that $\tau a^2/\kappa << 1$). Where explicitly stated, a controlled amount of NaCl was also added to the exterior solution to test for electrostatic effects.

The cationic nanoparticles have a gold core functionalized with surface ligands consisting of a thioalkyl tetra(ethylene glycol)ated trimethylammonium (TTMA) ligand (Fig. 3.1A).[72,80] The tetra(ethylene glycol) spacer was added to keep the particles stable in suspension. Particles were synthesized using the Brust–Schiffrin two-phase synthesis method[81] and then functionalized with TTMA ligands via place exchange reactions.[82] The core diameter was 2 nm (transmission electron microscopy), the hydrodynamic diameter was 6.7 ± 0.4 nm (dynamic light scattering, DLS), and the zeta potential in suspension was 18.2 ± 0.8 mV (electrophoretic mobility).[72] Anionic particles were silica, Ludox AS-30 and Ludox SM (Sigma-Aldrich). The mean particle radii were a = 11.3 nm and 12.6 nm, respectively (DLS, measured in the same solution conditions as our vesicle experiments).

To observe binding dynamics, we injected vesicles into a long, narrow perfusion chamber mounted on an optical microscope (Fig. 3.2), then added 5 μL of nanoparticle and sugar suspension (178 mOsm L^{-1} glucose + sucrose) into one end of a perfusion chamber. See Chapter 2 for more information.

Molecular dynamic simulations were conducted by collaborators at Brandeis University and included in the final publication for our nanospheres results.[72] This material is adapted from that paper and helps to provide context for interpreting our experimental results. Molecular dynamics simulations were preformed to determine how the particle-membrane adhesion strength changed dynamics and the steady-state configuration. The membrane was represented by the coarse-grained solvent-free membrane model,[102] which is computationally tractable while capturing the relevant features of biological membranes. The lipids were represented three beads, one bead for the head and two beads for the tails. There are short-ranged attractive interactions between pairs of tail beads that represent hydrophobic effects, and short-range repulsions between pairs of head beads and head-tail pairs. Nanoparticles and membrane-head beads interacted through a Lennard-Jones potential, with well-depth ε_{att} determining the strength of the nanoparticle-membrane attraction (which was tuned by salt concentration or lipid composition in the experiments). To represent excluded volume, there were also repulsive interactions between nanoparticles and lipid tail beads and nanoparticle– nanoparticle pairs. Membranes were initially planar, approximating the fact that in the experiments the radii of curvature of the initial vesicles was much greater than a. A 170 × 170 nm membrane was initialized in the center of a box of height 150 nm. Tension was held near zero. Next, n nanoparticles were initialized in the upper half of the box, so that the nanoparticle area fraction (if all nanoparticles adsorbed) was given by $p_{np} = n\pi a^2/L^2$, where L is the lateral membrane dimension. Periodic boundary conditions applied in the plane of the membrane, ensuring that nanoparticles remained on one side of the membrane (unless it ruptured).

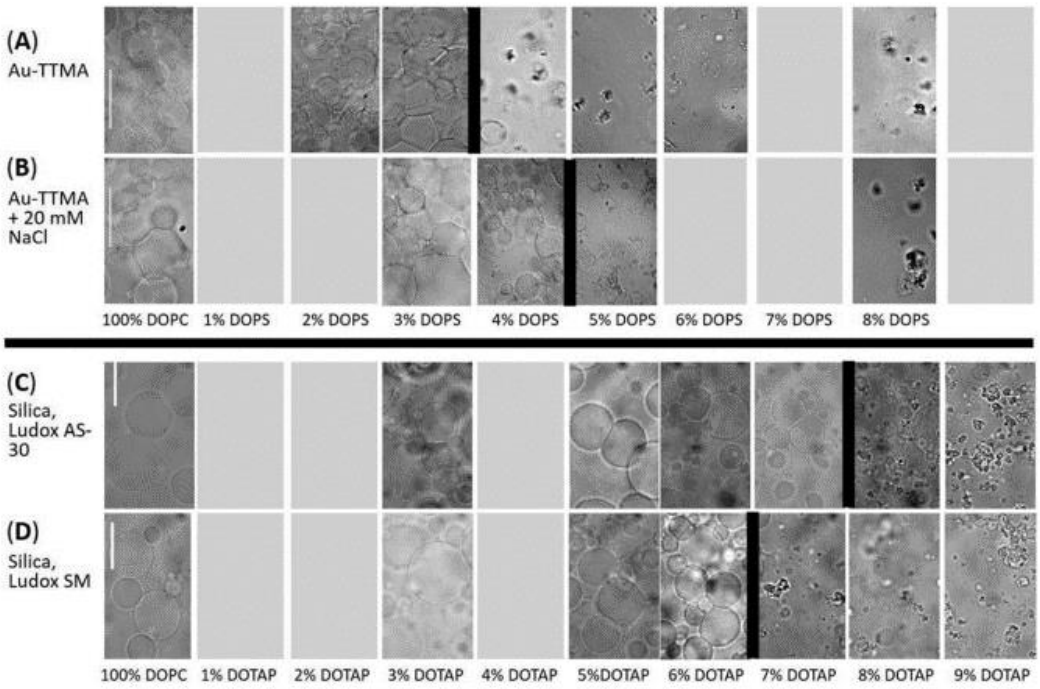

Figure 3.3: State diagram of spherical particle interactions

Bright-field optical micrographs show state diagrams of GUVs with varying lipid composition in the presence of three different types of nanoparticles. The fraction of charged dopant lipid increases from 0 to 9 mol% from left to right. The heavy black lines indicate the boundary between samples that showed adhesion and gel formation vs. those that underwent tubulation and destruction. (A) Cationic Au-TTMA particles with anionic DOPS lipid. (B) Same as (A), but with 20 mM NaCl added (still osmotically balanced), which shifts the threshold. (C) Anionic silica (Ludox AS-30, a = 11.3 nm radius by DLS) with cationic DOTAP lipid. (D) Anionic silica (Ludox SM, a = 12.6 nm by DLS) with DOTAP lipid. Scale bars are 20 μm and each applies to images in the same row.

Section 3: Results

In this section, we describe the phenomenology of the gel and destruction regimes. Throughout, we focus primarily on the cationic Au-TTMA-nanoparticle results, and then later show a comparison to the anionic silica nanoparticle results. We then describe molecular dynamics simulations that show a similar crossover from weak binding to destruction. Finally, in the Discussion section, we describe the underlying mechanisms and compare to prior work.

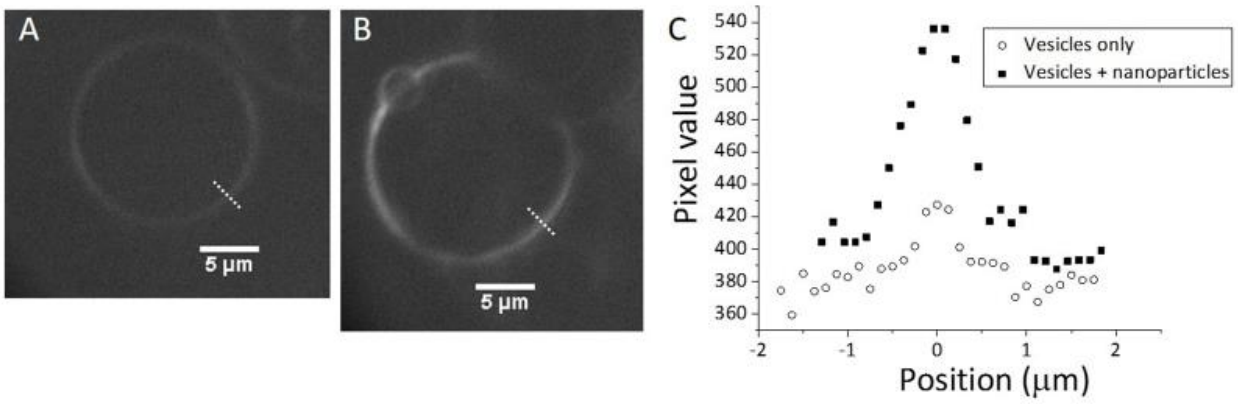

Figure 3.4: Darkfield image of vesicle, spherical nanoparticles

(A) Dark-field image of a vesicle, showing faint contrast owing to light scattering from the membrane. (B) Dark-field image of a vesicle in the presence of nanoparticles, showing additional scattering by bound nanoparticles. (C) Plot of camera-pixel intensity vs. position along line segments shown by the white dashed lines in A, B. We estimated the extent of light scattering by the difference between the peak and background intensities. The values were approximately 140 and 40 with and without the particles, respectively. This approximately 3-fold enhancement of the scattering is attributed to the bound nanoparticles.

Subsection 3.1: Overview of the phenomenology

We studied the response of vesicles in situ after nanoparticles were added to the surrounding suspension. By adjusting the charged-lipid content of the vesicles, we tuned their average surface charge and thereby the adhesion energy per area, w, between the lipid bilayer and the oppositely charged nanoparticles. We took care to match the osmotic strength of the added nanoparticle suspension to that of the vesicle suspension, so that osmotic shock did not play a role in these processes. Fig. 3.1 summarizes the two distinct behaviors that we observed with cationic Au-TTMA particles: adhesion and vesicle-gel formation at low DOPS fraction, and vesicle tubulation and destruction at high DOPS fraction. Remarkably, these two regimes of behavior were separated by a well-defined threshold charged-lipid fraction. Fig. 3.3 shows ‘state diagrams’ for these systems, in the form of images of the steady-state structure as a function of dopant lipid mol%. For Au-TTMA (a = 3.4 nm) and DOPS without added salt, the threshold value was 4 mol%

(Fig. 3.3A). With 4 mol% DOPS, a minority of vesicles survived in the steady state, whereas (for example) with 8 mol% DOPS, a negligible number of GUVs survived in the steady state. We attribute the surviving vesicles to statistical variations in lipid composition of individual GUVs, so that a few individual vesicles may have been below the threshold 4 mol%. The behavior of the GUVs was found to be unchanged if the exterior sugar solution was 180 $\mathrm{mOsm\ L^{-1}}$ (as described in the Experimental section) or lowered to 170 $\mathrm{mOsm\ L^{-1}}$ before exposure to the nanoparticles. Fig. 3.3B shows the AuTTMA particles with 20 mM NaCl in solution (while still balancing osmolarity inside and outside). Here we found a higher threshold, 5 mol% DOPS. Other observed phenomena such as increased contrast and dark mobile particle aggregates also appeared at threshold, similar to the case without added NaCl. We attribute the threshold shift to screening of the electrostatic attraction, which meant that more DOPS was needed to achieve the same adhesion energy. All observed interactions were consistent with an effective decrease in the electrostatic interaction realized as a shifting of all charge-dependent behaviors uniformly. Below we describe the electrostatic interaction in terms of charged double-layer theory. This treatment of the role of added salt, though simplistic, captures the main effect. A similar threshold behavior was found for anionic silica particles of two different sizes, with added cationic DOTAP lipid (Fig. 3.2C and D). In these cases, the thresholds were 8 mol% and 7 mol% for particles with a = 11.3 and 12.6 nm.

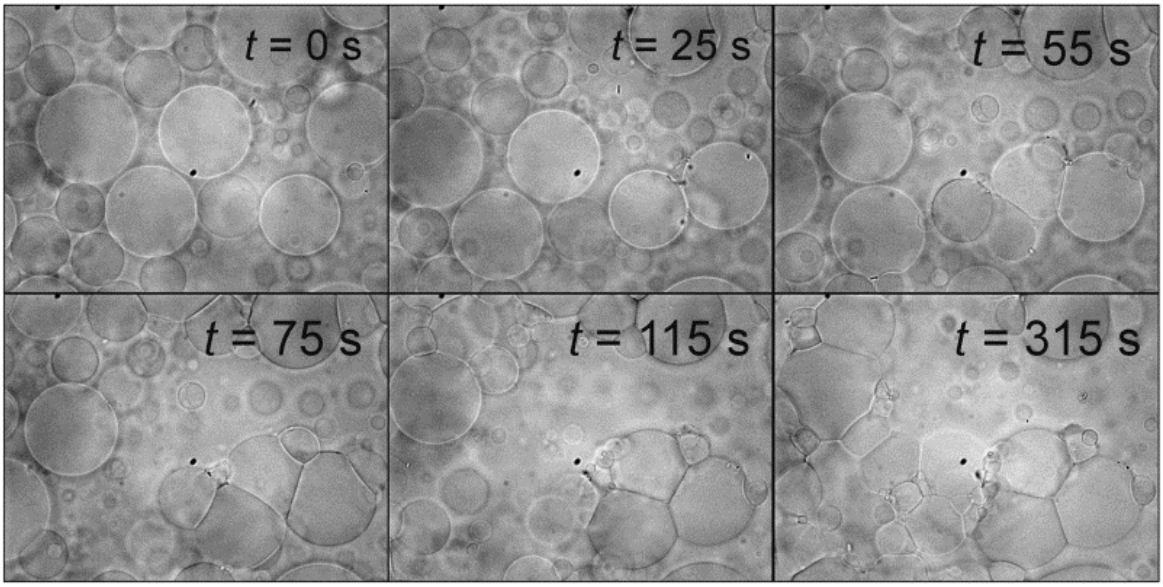

Figure 3.5: Time lapse of vesicle gel, spherical nanoparticles

Time lapse images in bright-field mode show the adhesion process of DOPC vesicles (without DOPS) as Au-TTMA nanoparticles diffused into the imaged region from the right.

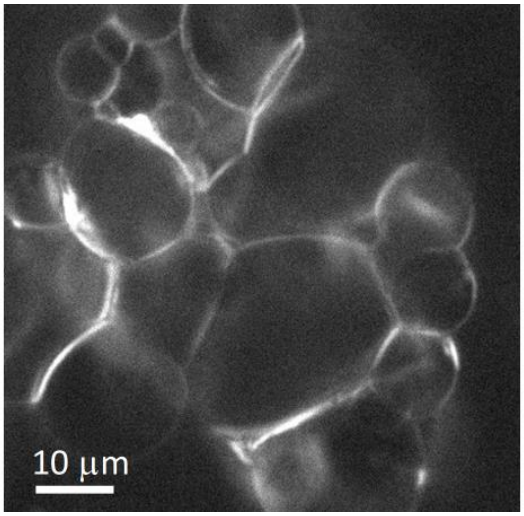

Figure 3.6: Darkfield image of vesicle gel: spherical nanoparticles

Dark-field image of a vesicle gel, showing scattering from Au-TTMA nanoparticles in the adhesion regions. The membrane is composed of DOPC only.

Subsection 3.2: Weak binding: vesicle adhesion and gel formation

When the DOPS content in the membrane was <4 mol%, the Au-TTMA nanoparticles bound to the vesicles' surfaces without any discernible deformation. The particles were able to

spread laterally on the membrane with no observable aggregation. Evidence of particle binding is provided by dark-field optical microscopy. This microscopy technique indicates where the nanoparticles are concentrated. The image intensity comes from light that is scattered in the sample plane and the gold particles scatter much more strongly than lipids. Fig. 3.4 shows example dark-field images, providing evidence that the nanoparticles have bound on a vesicle's surface. When the concentration of vesicles was high enough so that vesicles touched one another, the membranes adhered to one another owing to the nanoparticles' forming an adhesive bridge between them. The adhesive contact area grew over a typical time on the order a few minutes before reaching a steady state (Fig. 3.5).

Even in the absence of DOPS, we still observed nanoparticle binding, consistent with earlier findings that DOPC vesicles have a slightly negative electrostatic (zeta) potential of −9 mV (electrophoretic mobility with 0.1 mM NaCl[73]) and that they adhere to cationic particles.[70,103]

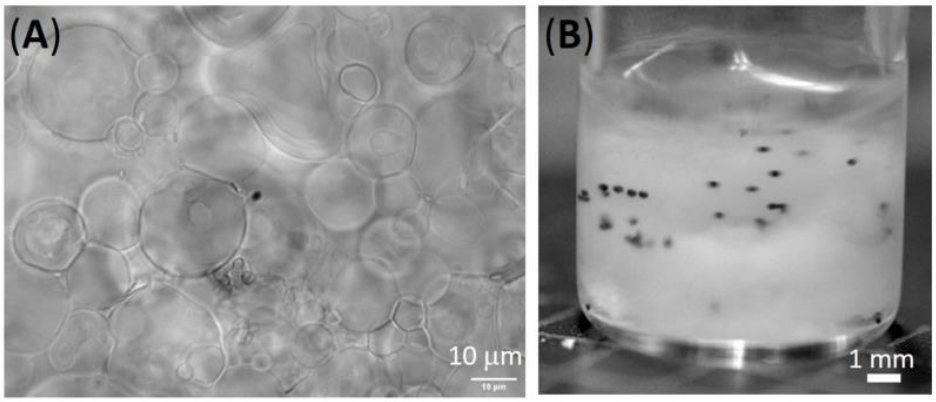

Figure 3.7: Vesicle Gel

Images of a gel composed of soy-lecithin PC vesicles with polycation (PDADMAC) added. (A) Optical micrograph showing that the vesicles remain intact. (B) Photograph showing that 270-μm-diameter copper beads were suspended within the gel, showing that the gel could resist shear stress and was a solid.

Adhesion led to a network of fluid vesicles, which we call a "vesicle-gel." In appearance, the approximately polyhedral vesicles (Fig. 3.1B) resembled bubbles in a dry soap foam, except

that here the interior and continuous phases were both aqueous. Fig. 3.6 shows a dark-field image of a steady-state gel, composed of DOPC vesicles, in which strong light scattering is clearly visible at the adhesion sites between vesicles. Nanoparticles accumulated at the vesicle–vesicle junctions because of their ability to bind to both membranes. No systematic variation of morphology was found in images of samples where the DOPS fraction varied between 0 and 3 mol%.

Large quantities of adhered vesicles act as a solid: To probe the mechanical properties of the vesicle-based gels, we developed an alternative system that can be made in large quantity using inexpensive, food-grade soy lecithin phosphocholine lipid (SLPC). Success in making large (50-mL) quantities shows the potential of this method for widespread application. To further expand the range of materials that can be used to form the gel, we added cationic polymer (either poly-L-lysine (150 kDa) or the more highly charged polydiallyldimethylammonium chloride (PDADMAC, 200 kDa)). With concentration 0.1% wt/vol, each polycation successfully caused aggregation of the vesicles into a gel. In all cases with polycations, we observed vesicle-vesicle adhesion and gel formation. As in the vesicle gels made with added nanoparticles (main text. Fig 1B), these vesicles remained intact as shown in Fig 7A. Even with up to 15 mol% DOPS, we never observed the destruction process, which indicates that the rigid particle shape is necessary to trigger the destruction.

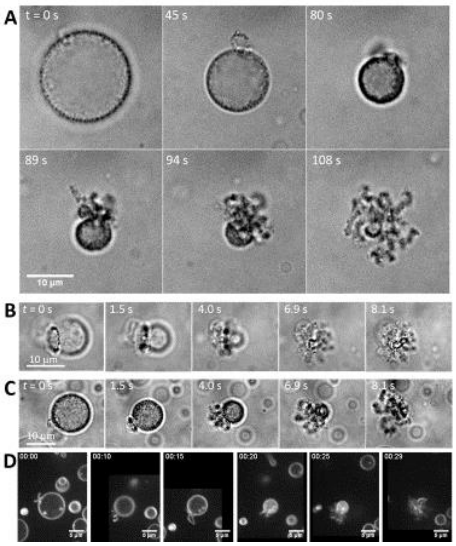

Figure 3.8: Vesicle Destruction, spherical nanoparticles

Microscope images showing the disruption process above threshold binding strength. (A) Bright-field images of 6 mol% DOPS; (B) Confocal fluorescence images of 5 mol% DOPS with <1 mol% Rh-DOPE. (C) Bright-field image of surface spots in GUV with 6 mol% DOPS. (D–F) Images of vesicles with a long-lasting pore. (D) Bright-field image, 6 mol% DOPS. Interior sugar solution can be seen escaping the pore, as indicated by white arrow. (E) Confocal image, 5 mol% DOPS + 1 mol% Rh-DOPE. (F) Dark-field image highlighting nanoparticles, 4 mol% DOPS.

We found that a 50 mL-volume sample of the SLPC vesicle gel, see figure 3.7B, with PDADMAC was able to support 270 μm-diameter copper beads against gravity for several hours, which indicates a low-frequency shear modulus and a yield stress of at least a few. (In a sample of vesicles without adsorbing polymer, the copper beads settled to the bottom of the vial.) The net force on the copper beads due to gravity is on the order of μN, so that each bead applied an average pressure of roughly 10 Pa, putting a very rough lower limit on the gel's yield stress. Hence, these materials are solid, albeit quite soft. Their closed-cell structure allows the gel to encapsulate a large volume of liquid within a series of robust interior partitions. The potential as a useful delivery vehicle for drugs, dyes, or reagents will be discussed below.

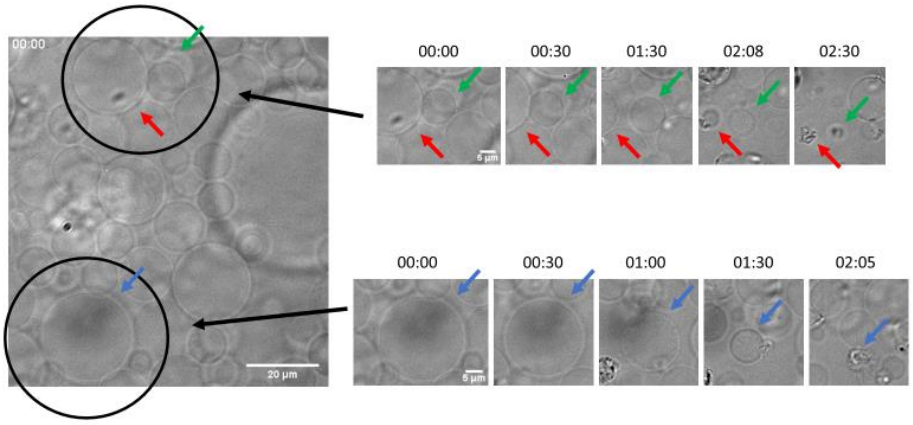

Figure 3.9: Vesicle destruction comparison

Bright-field images of three different GUVs in the same field of view as they undergo destruction. The sample contains Au-TTMA particles and GUVs with 94 mol% DOPC and 6 mol% DOPS. The red, blue, and brown arrows each point to a given vesicle over time. The initial vesicle diameters were 11, 21, and 25 µm, respectively. Times of each image are shown in the format, minutes: seconds.

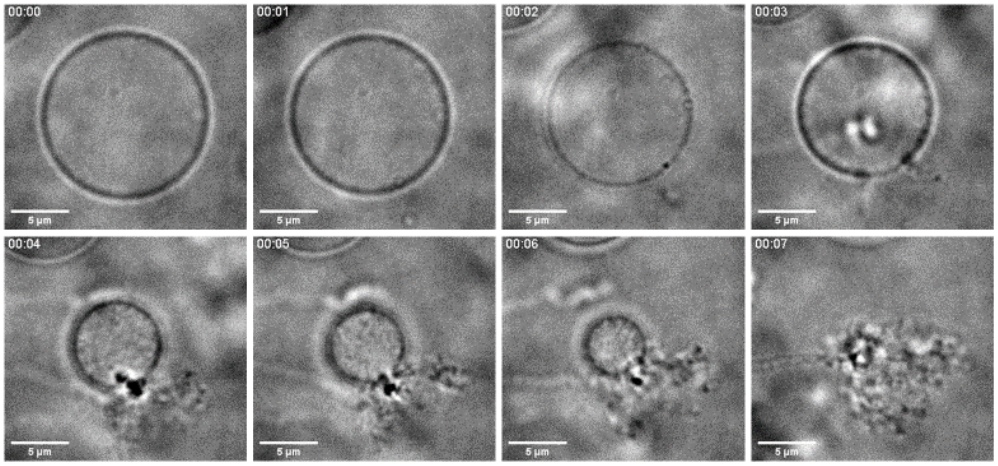

Figure 3.10: Vesicle destruction montage

A montage of brightfield micrographs showing the disruption process above threshold binding strength. This vesicle contained 29 mol% DOTAP and was exposed to silica (Ludox AS30) nanoparticles. Scale bars are all 5 µm.

Subsection 3.3: Strong binding: the stages of destruction

By contrast, when the DOPS content reached a threshold value (approx. 4 mol%), Au-TTMA nanoparticle binding caused complete vesicle disruption in a multi-stage process (Fig. 3.8). Although each vesicle differed in detail, the stages were common across hundreds of vesicles in

dozens of different samples. We begin with a brief synopsis here, then provide details in the following paragraphs, and propose mechanisms in the Discussion section. First, the vesicle diameter steadily decreased over a typical duration of several seconds to minutes as the membrane became loaded with nanoparticles. Vesicles developed nanoparticle-rich spots that diffused on the surface. Vesicles that shrank faster than a rate of 300 $\mu m^2 s^{-1}$also developed a single, long-lived pore, through which the interior solution was expelled. Remarkably, these pores maintained stable diameters in the range of 1–10 μm. Finally, these vesicles underwent a complete destruction, wherein the spherical vesicle rapidly shrank until the folding and compression of the surface caused the vesicle to unfurl into a network of lipid tubules coated in nanoparticles. Vesicles that did not form a visible pore earlier in the process continually shrank and then suddenly ruptured and tubulated. There was no discernible dependence of threshold composition or other behavior on the GUV size. Figure 3.9 shows an example of three GUVs whose diameters varied by more than a factor of 2. In multilamellar vesicles, the outer layers of the vesicle peeled off one by one as they were attacked by the nanoparticles, until only one inner layer remained. A similar sequence of apparent shrinkage, pore formation, tubulation and destruction is show for anionic silica (Ludox AS30) exposed to cationic-lipid-doped vesicles above threshold in figure 3.10.

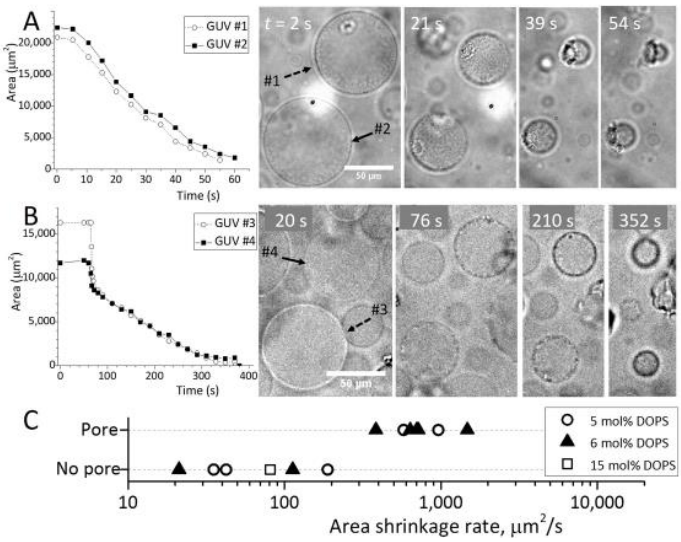

Figure 3.11: Rate of vesicle destruction, spherical nanoparticles

Measured surface areas over time for vesicles attacked by Au-TTMA nanoparticles. (A) 5 mol% DOPS; nanoparticles were added at t = −5 min. The average rate of area reduction was 500 $\mu m^2 s^{-1}$. Both vesicles developed a surface pore (visible at t = 21 s), then gradually inverted through the pore as they shrank. (B) 5 mol% DOPS; nanoparticles were added farther away, at t = −50 min and the local concentration of nanoparticles was lower than in (A). The average rate of area reduction was approx. 35 $\mu m^2 s^{-1}$. The vesicles suddenly ruptured at t ≈ 400 s without having first formed a visible pore. (C) A plot of area shrinkage rates of 13 vesicles and various DOPS composition above threshold. All vesicles that shrank faster than 300 $\mu m^2 s^{-1}$ developed a pore (upper row of symbols) and none of the slower ones did (lower row of symbols). (data acquired by Derek A. Wood and adapted from ref. 1)

At the start of the disruption process, the diameter of the vesicles steadily decreased. As shown in Fig. 3.11, vesicles close to one another tended to shrink at similar rates (data acquired by Derek A. Wood and published in ref. 1). Fig. 3.11A shows vesicles that were close to the site of Au-TTMA nanoparticle addition; for most of the shrinkage process, these two vesicles lost apparent surface area at an average rate of approx. 500 $\mu m^2 s^{-1}$. Surprisingly, the appearance of a large pore on the surface of each vesicle had no discernible impact on the shrinkage rate. Fig. 3.11B shows vesicles that were farther from the point of nanoparticle addition, so that the local nanoparticle concentration was reduced by their diffusive spread throughout the sample. The sharp initial decrease in radius was observed in many vesicles and is attributed to excess area in the initial configuration. Following this rapid decrease, the steady area-shrinkage rates were approx. 35 $\mu m^2 s^{-1}$, about 14× lower than in Fig. 3.11A. In separate experiments, we added nanoparticles

with a 14× reduced concentration and found that the average shrinkage rate decreased to 0.004 $\mu m^2 s^{-1}$, and the rupture process required an hour or more to complete. These data show that the rate of vesicle shrinkage was strongly correlated with nanoparticle concentration. This point will be discussed below.

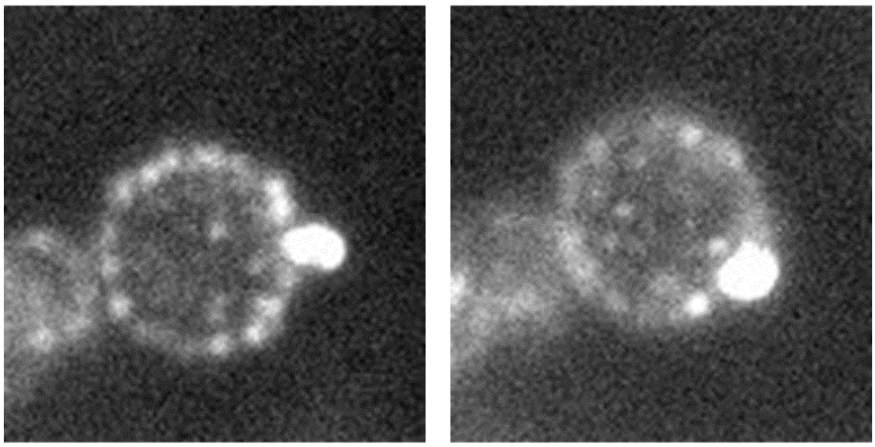

Figure 3.12: Darkfield image of dark mobile aggregates, spherical nanoparticles

Vesicles showing surface spots when the DOPS fraction exceeds the threshold value. Dark-field imaged, 4 mol% DOPS with Au-TTMA particles.

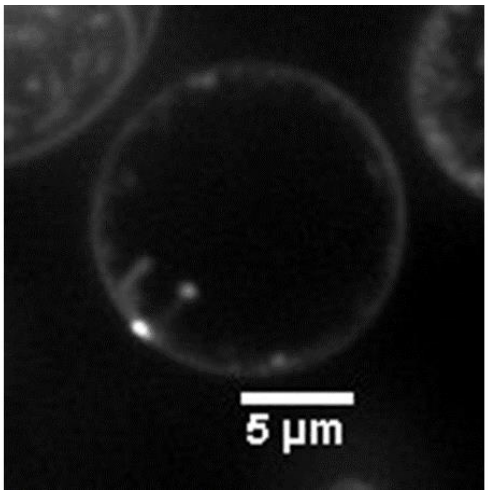

Figure 3.13: Confocal image of inward tubules, spherical nanoparticles

A confocal microscope image of a vesicle containing 5 mol% DOPS + approximately 1 mol% Rh-DOPE, exposed to Au-TTMA nanoparticles. Inward-facing tubules (invaginations) are clearly visible in the image.

As the diameters of the vesicles shrank, spots appeared on the surfaces (Fig. 3.8C). These spots were always similar in size to the microscope's resolution limit, so that their true size could not be measured accurately. The spots were bright under dark-field imaging (Fig. 3.12), indicating that they were enriched in Au-TTMA nanoparticles. Figure 3.8C of the main text shows a similar phenomenon on bright-field, where the scattering of light by the particles made the clusters appear dark. We never observed nanoparticle aggregates in solution; they were only found on the vesicle surfaces above threshold. These observations indicate an attractive interaction between particles that was mediated by the deformed membrane. Throughout, the spots remained mobile on the vesicles' surfaces. As the vesicle shrank, these spots visibly increased in concentration but did not increase in apparent size. Every vesicle that we imaged above threshold DOPS had these dark spots in conjunction with surface shrinking. Nanoparticle clusters were not found in solution; they were only found on the vesicle surfaces. Confocal microscope images show lipid-nanoparticle tubules extending toward the vesicle's interior (Fig. 3.13). In the Discussion section, we propose that the vesicles turned inside out during the final stage, so that these tubules extended outward.

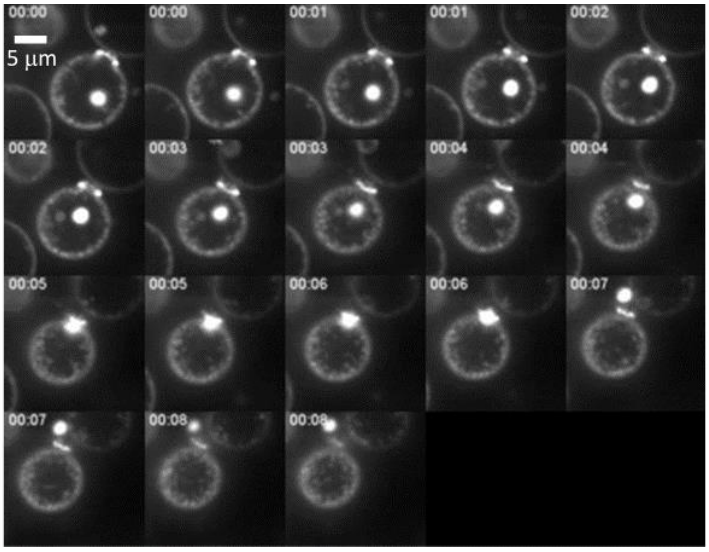

Figure 3.14: Montage of lipid mass expelled through pore, spherical nanoparticles

A montage of images acquired with confocal fluorescence microscope. This vesicle contained 5 mol% DOPS + approximately 1 mol% Rh-DOPE and was exposed to Au-TTMA nanoparticles. Scale bar is provided in the first image. Initially, there was a large solid lipid-based object inside the vesicle. Over time, this object was forced out through the pore by the internal pressure. While this particle was inside the vesicle, it diffused slowly. It was then trapped in the pore for 3 frames, and then finally ejected a distance of more than 3 μm in the following frame (t = 7 s).

Formation of an open, micron-sized pore that persisted for at least several seconds is a striking and unique feature of our results. Fig. 3.8D–F show that these pores are truly open. In Fig. 3.8D, escape of the encapsulated fluid (175 $\mathrm{mOsm\,L^{-1}}$ sucrose) can be seen because it has a different index of refraction than the exterior fluid (87.5 $\mathrm{mOsm\,L^{-1}}$ sucrose + 90 $\mathrm{mOsm\,L^{-1}}$ glucose), leading to a visible fingering effect. Furthermore, the confocal image Fig. 3.8E shows an open hole without lipid. A time-series of images of this vesicle shows that the bright lipid particle inside the vesicle was pushed out through that pore (Fig. 3.14). Observing vesicles that contained smaller vesicles inside them, we found expulsion of the interior contents through the pore (Fig. 3.15). We found a characteristic 'pearl necklace' morphology at the outer rim of each pore, consisting of clearly discernible clusters that surrounded the rim of the pore. The dark-field image of Fig. 8F shows that these clusters were enriched in Au-TTMA nanoparticles, visible by their strong scattering.

Fig. 3.11C shows the rate of area shrinkage for 13 vesicles with various DOPS fractions above 4%, (data acquired by Derek A. Wood and published in ref. 1). In the plot, the shrinkage rate varied from 20 to 2000 $\mu m^2 s^{-1}$. The plot also shows whether or not each vesicle formed a visible pore. There is a striking pattern: only vesicles whose surface area decreased faster than approximately 300 $\mu m^2 s^{-1}$formed a visible pore, regardless of the DOPS content of the vesicle (as long as it was above the threshold). Based on our results from the previous paragraph, we conclude that the particle concentration determined the rate of vesicle shrinkage and this rate, in turn, controlled pore formation.

The final stage of the disruption process was the complete destruction of the vesicle structure, resulting in a network of tube-like structures (e.g., Fig. 3.8A and B). From the optical images, we estimate that tubules had a typical diameter of approximately 1–2 μm. We found no evidence that the initial vesicle size or DOPS content (as long as it was above the threshold) affected the rate of shrinking of the vesicles or the sizes of the remaining tubule structures. In multilamellar vesicles, the outer layers of the vesicle peeled off one by one as they were attacked by the nanoparticles, until only one inner layer remained (Fig. 3.16).

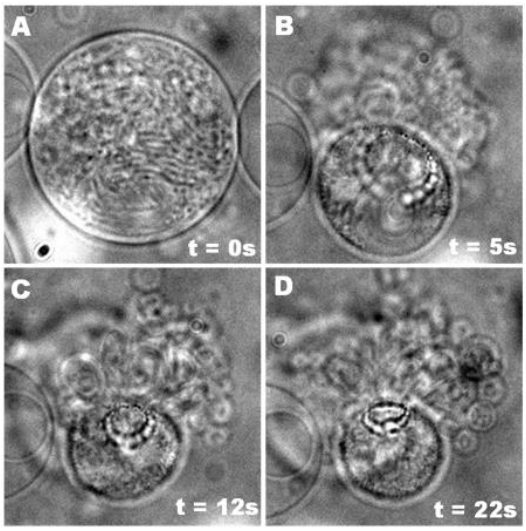

Figure 3.15: Vesicle with pore, spherical nanoparticles

Bright-field microscope images show the interior contents of a vesicle with many interior compartments spilling out through a pore on the vesicle's outer surface as Au-TTMA nanoparticles bound. (5 mol% DOPS) The relative times of the images are shown in the lower right corners. The magnification was the same in all of these images.

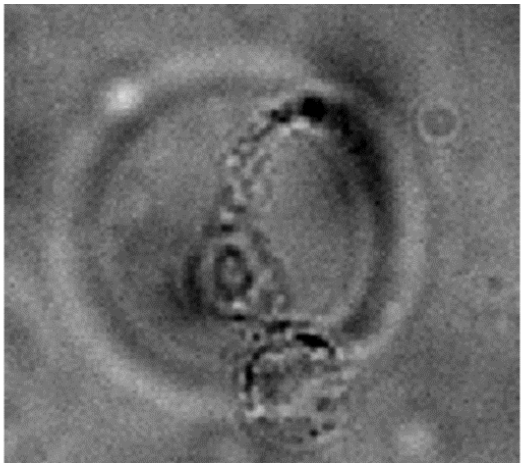

Figure 3.16: Multi-lamellar vesicle

Bright-field image of a multi-lamellar vesicle (5 mol% DOPS), in which the outermost lamella has been 'attacked' by Au-TTMA nanoparticles and peeled away.

Subsection 3.4: Computer simulations of nanoparticle binding

Our collaborators at Brandeis, Guillermo R. Lázaro and Michael F. Hagan, carried out Brownian dynamics computer simulations of spherical nanoparticles binding to adhesive membranes to explore this system in microscopic detail and establish the mechanisms underlying its behavior. Here a = 5 nm and the membrane bending modulus[14], κ, equal to 8.2×10^{-20} J, appropriate for DOPC.[104] Like the experiments, simulations were in the regime of $\tau \ll \kappa/a^2$ and $\omega a^2/\kappa$ tunable from 0 to more than 1.

Fig. 3.17 shows the steady-state configurations obtained with increasing particle-membrane adhesion for various surface concentrations (area fractions). When $\omega a^2/\kappa < 0.5$, simulations showed that particles adhered to the membrane without membrane tubulation or destruction. In the regime where $\omega a^2/\kappa > 0.7$, the simulations show a trend from partial buds to tubules to membrane-rupture as the particle area fraction was increased. Tubules began as a linear cluster of two or more particles lying on the plane of the membrane; the cluster was then enveloped

by the membrane and reoriented as a tubule (see Fig. 3.18 for snapshots of typical trajectories). In the intermediate regime, $0.5 < \omega a^2/\kappa < 0.7$, the ruptured configuration was pre-empted by linear arrays of particles. It may be that these linear-array states might eventually nucleate tubules, as has been suggested previously.[71]

In our experiments, the particle area fraction was not fixed, but increased over time as more particles bound to vesicles. The simulations' trend of partial buds, tubules and rupture with increasing particle density therefore correspond closely with the observed process of invagination (tubule formation) and pore formation over time in the experiments.

A key result of the simulations is a well-defined value of $\omega a^2/\kappa = 0.5$ that defines a crossover from binding to tubule formation. In most cases (especially above 0.6), the simulations showed membrane rupture. This finding is consistent with the threshold behavior seen in the experiments and explains many of the observed stages of destruction

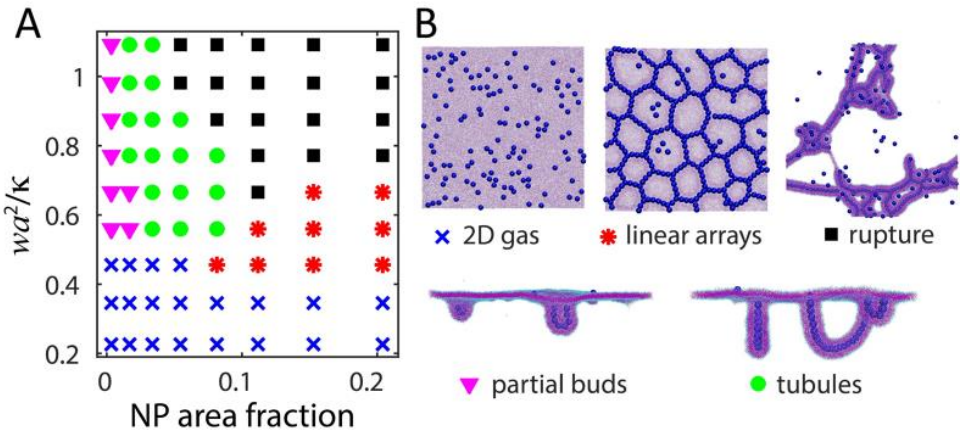

Figure 3.17: Nanosphere simulation steady-state diagram

(A) Diagram showing the steady-state configurations found in simulations as functions of dimensionless adhesion free energy and particle concentration. The symbols correspond to the states illustrated in (B). Particles are rendered in dark blue and membrane headgroups are in violet.

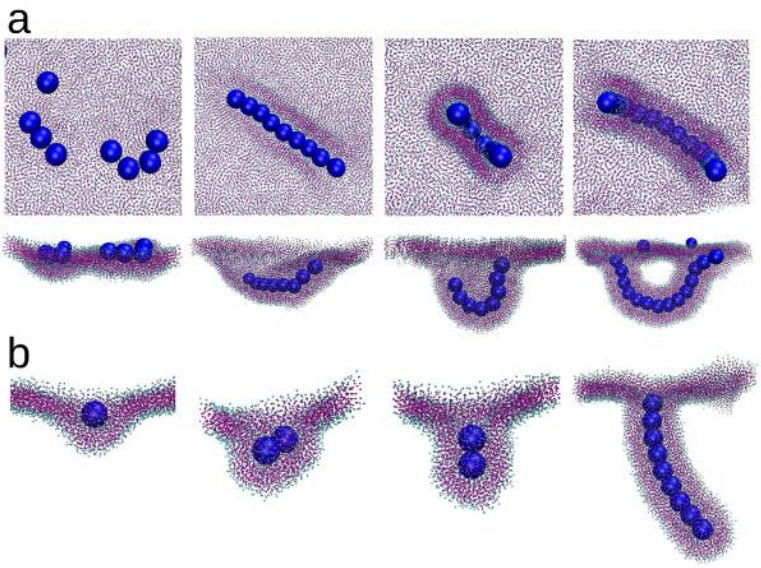

Figure 3.18: Simulation trajectories

Representative simulation trajectories illustrating the pathways of tubule formation. (a) Snapshots showing the formation of a 'U-tubule', meaning that the tubule is connected to the membrane at both ends. Particles initially formed a linear aggregate on the relatively flat membrane; subsequently the membrane wrapped the aggregate leading to tubulation. (b) Snapshots showing, I-tubule formation, meaning that the tubule is connected to the membrane only at one end. Formation began with envelopment of two NPs, forming a duplet oriented normal to the membrane. The tubule then extended through diffusion and association of additional NPs.

Section 4: Discussion

Our results show that vesicle adhesion and destruction were triggered by the binding of the nanoparticles, not by osmotic stress. In all of our experiments, there was a large excess of nanoparticles relative to membrane area. The key parameter was the fraction of DOPS or DOTAP in the membrane, which served to tune the adhesion strength ω between particles and the membrane by means of an electrostatic double-layer attraction. According to our simulations, the threshold from adhesion to destruction corresponds to a sharp crossover at the particle-scale from weakly-bound to fully enwrapped particles. The particle-scale wrapping transition is also consistent with our experimental findings and can explain many aspects of the destruction process. Below threshold, the nanoparticles bound to the membrane, were able to diffuse laterally, and

spread throughout the outer leaflet of the membrane until the steady-state surface coverage was attained. Above threshold, the membrane continually enveloped particles and left unbound membrane exposed. Such a process of continuous envelopment should continually generate in-plane strain and force an overall remodeling of the membrane shape. A schematic overview is given in Fig. 3.19.

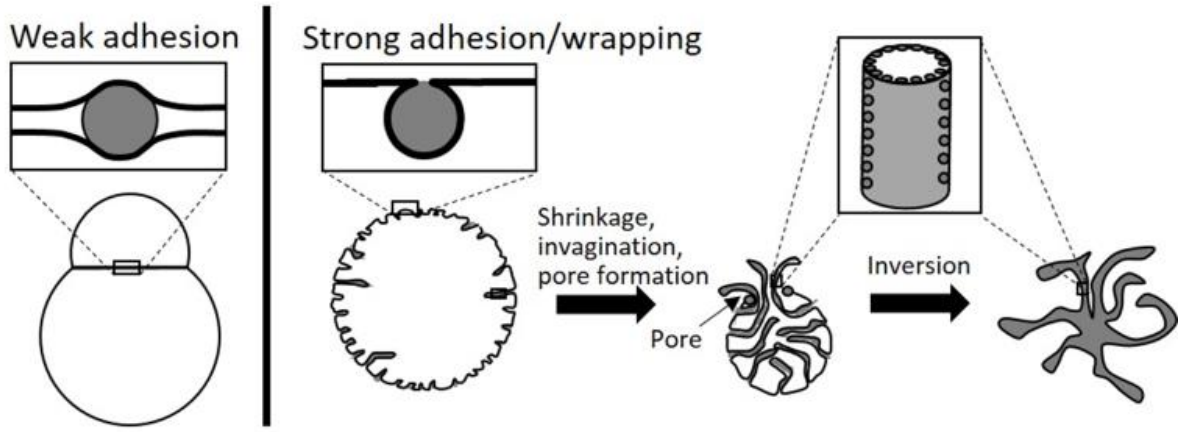

Figure 3.19: Illustration of adhesion, spherical nanoparticles

Illustrations of the adhesion (left) and the multi-stage destruction process (right).

In continuum theory, this wrapping transition for a single spherical particle was predicted from the Helfrich model of the membrane, accounting for large-amplitude deformations where linear superposition fails.[79,105] When the membrane tension $\tau = 0$ and the interaction is of short range, the transition is discontinuous and occurs when $\omega a^2/\kappa = 0.2$. Membrane tension is predicted to shift the discontinuous transition to higher[79], ω, while a finite range of interaction softens the transition.[14] The threshold can be reduced below 2 if there are many nanoparticles, as suggested in a theoretical study with three or more particles.[99] Our computer simulations with

many particles showed a crossover to tubulation and destruction at a considerably lower threshold, $\omega a^2/\kappa$ near 0.5. The linear particle arrays in our simulations (Fig. 3.17B) and in ref. 71. suggest a crude but simple approximation, in which a linear particle aggregate is treated as a long cylinder lying in the plane of the membrane. The energy of bending around a cylinder of radius a is 4× smaller than for bending around a sphere of radius a because the membrane curves only in one direction. In the continuum limit and with a finite concentration of bound nanoparticles, this implies a wrapping threshold when $\omega a^2/\kappa = 1/2$. Although this approximation does not account accurately for the details of the membrane shape, it is consistent with the simulations. Whatever is the exact numerical value of the threshold, the continuum theory and our simulations all suggest that the dimensionless combination $\omega a^2/\kappa$ is the key parameter setting the threshold.

Guided by the simulations, we used the threshold criterion that $\omega a^2/\kappa = 1/2$, where ω is the adhesion free energy per area, a is the particle radius (3.4 nm in the Au-TTMA experiments), and κ is the membrane bending energy (8.2×10^{-20} J, appropriate for DOPC[79]). We used Poisson-Boltzmann theory to account for the electrostatic double-layer interaction between the membrane (treated as a plane) and the spherical particle. The dopant lipids were treated as a mean-field charge density, which is justified by the fact that the patch of membrane wrapping each particle had, on average, several charged lipids (*i.e.*, more than one). Assuming the lipids were uniformly distributed, the number of charged-lipid molecules per nanoparticle area, per membrane leaflet at threshold was approximately eight for the Au-TTMA system, 183 for the silica Ludox AS30, and 200 for Ludox SM.

The membrane potential can be taken as the sum of the pure-DOPC potential (-9 mV from electrophoretic mobility[13]) plus the potential coming from a charge of - e per DOPS, where e is the fundamental charge, 1.6×10^{-19}C. We consider only the charge on the outer leaflet of the

membrane. The Au-TTMA surface charge density can be obtained from the ligand density (77 ± 4 per particle[14]). The quaternary ammonium groups at the ligand termini have a permanent positive charge, which gives a charge density of approximately $0.5\ e/\mathrm{nm}^2$. (Extracting charge density from the measured zeta potential of 18 mV gives a much lower density of roughly $0.2\ e/\mathrm{nm}^2$ but this is not a reliable method to obtain surface charge[15]. The same caution applies to the pure DOPC membrane, but we have no other means to estimate surface charge density.) Using these estimates and applying the condition $\omega a^2/\kappa = 1/2$, we estimate a threshold composition as low as 3 mol% DOPS, or as high as 70 mol% DOPS for the (likely inaccurate) lower estimate of the nanoparticle charge from zeta potential.

This estimate neglects two phenomena that may be quantitatively important. First, the DOPS lipids should tend to accumulate near the nanoparticles, which increases the double-layer interaction at the cost of lowering their entropy. A prior theoretical treatment of this effect estimated that in a zwitterionic PC-lipid membrane with 10 mol% anionic lipid, in-plane rearrangements enhance the binding free energy of a cationic rod-shaped particle by a factor of approximately 1.7.[27] In the present case, the effect seems to us likely to be of the same order of magnitude. Second, treating the nanoparticle-membrane interaction in terms of adhesion per area is a crude approximation because the range of interaction (set by the Debye length of 2 nm or more) is comparable to particle size.

Nonetheless, the rough estimate serves to show that a threshold composition of a few mol% DOPS is consistent with the prediction of $\omega a^2/\kappa = 1/2$. These estimates also guide predictions of how parameters such as charge density, salinity and membrane modulus should affect the threshold composition.

For the silica/DOTAP systems, the overall behaviors were similar, but the measured thresholds were different from AuTTMA/DOPS. Even though the silica particles were larger than the Au-TTMA, the thresholds were higher. In part, this is because of the negative potential of the DOPC, which has to be overcome by added DOTAP. It is also likely that the magnitude of the surface charge density of the silica particles differs from that of the Au-TTMA. We did find, however, that the slightly larger particles (by DLS) had the slightly lower threshold. This finding is consistent with our proposal that the threshold corresponds to a constant value of $\omega a^2/\kappa$, so that the threshold ω should vary as $1/a^2$.

As particles bind and are wrapped by the membrane, the projected surface area of the membrane shrinks because of the envelopment of each bound nanoparticle. If each nanoparticle-wrapping event reduces the projected membrane surface area by an amount equal to the surface area of the nanoparticle, $4\pi a^2$, a steady area-reduction rate of 500 $\mu m^2 s^{-1}$. on a 15000 μm^2 membrane (as in Fig. 3.11A) corresponds to a flux of roughly 200 particles per μm^2 per s binding to the membrane. If the particle flux were limited by their diffusion through water, the flux would be $3\phi D/(4\pi a^3 R)$, where D is the nanoparticle diffusion constant, R is the vesicle radius, and ϕ is the volume fraction of nanoparticles. From the known concentration of added nanoparticles, we verified that the diffusion-limited flux is high enough to account for the measured rate of vesicle shrinkage. This model explains why the area reduction rate depends on the local nanoparticle concentration.

We propose that as the effective surface area shrinks, the interior vesicle volume can only decrease at a rate limited by water permeation through the membrane. If the binding is too fast, then τ should increase and eventually reach the lysis tension, at which point the membrane should form a pore. If the area shrinkage is slow, however, the water permeation can keep pace with the

area reduction and the tension stays below lysis; in such cases no pore is expected. In our experiments, long-lasting pores were only observed in vesicles whose projected area shrank at a rate faster than 300 $\mu m^2 s^{-1}$ (Fig. 3.11C). Using the reported permeability and lysis tension of DOPC membranes,[106] we estimated a crossover shrinkage rate of order 0.1 $\mu m^2 s^{-1}$, which is far below the measured value. Moreover, our estimate neglects the osmotic stress that would arise if only water and not sugar can permeate the membrane; this would further slow the efflux of water and further increase membrane tension. This difference suggests that the membranes may be far more permeable to water and possibly sugar than expected, perhaps because of particle binding, as proposed previously.[70] The possible change of permeability with particle binding remains an important topic for further research.

Without nanoparticles, tension-induced pores generally close very rapidly[107] but with nanoparticles in our experiments, the pores were stabilized by the "pearl necklace" arrangement of particle-lipid clusters at the pore's rim (Fig. 3.8F). Since we never observed more than one pore on any vesicle, we conclude that pores allowed rapid expulsion of fluid so that τ remained below the lysis threshold.

The nanoparticle-rich spots (Fig. 3.8C) indicate clustering of nanoparticles, most likely because of attractive forces induced by the membrane deformation. Previous simulations showed that membrane-mediated attraction between particles occurs when the particles are strongly bound and highly wrapped.[63,20] Recent experiments with micron-scale particles confirmed this effect: weakly bound, partially wrapped particles had negligible lateral interactions, while fully-wrapped particles attracted one another over a distance of 3 particle diameters.[38] With many particles present, theory and simulations predict that membrane-mediated attraction can lead to linear aggregates[71,63] or compact clusters and tubulation.[14,66,107] Our experiments clearly show the latter,

while adding new information about the threshold behavior and the multiple steps in the tubulation and destruction process.

To form inward-facing, invaginated tubules (seen in our simulations and experiments, Fig. 3.13), the particles must reside on the interior, concave surface of the tubule. This configuration likely reduces the bending energy needed to enwrap the particles. Previous experimental[65,68,69] and numerical[14,63,97] studies of spherical particles or viruses also showed a tendency toward tubules with the particles on the inner, concave surface. Alternatively, it is possible that particle binding leads to a contraction of the outer leaflet of the bilayer, which would also favor concave curvature. Previous studies of cationic and anionic particle binding to phosphatidylcholine (PC) lipid membranes, however, indicated that cationic particles should tend to dilate the lipid layer, [74,108] which would more plausibly lead particles to favor positive (convex) curvature. Whatever the mechanism, the tubules invaginated such that particles remained on the concave surface while still remaining exterior to the vesicle.

In the final stage of destruction, each vesicle appeared to "erupt" into a network of particle-membrane tubules. This process was too rapid to see clearly with a confocal microscope but from our images we can identify two possible pathways. In the first possible mechanism, the vesicles turn inside out so that the tubules that had extended inward end up facing outward. Why would the vesicles turn inside out? To answer this question, we note that as tubules grew into the vesicle interior, they raised the interior pressure. This pressure is apparent in the time-series showing forcible ejection of an encapsulated lipid-based particle (Fig. 3.14). This pressure could therefore force the tubules to emerge through the open pore. In the final configuration, the particles still reside on the concave surface of the membrane tubules. In this state, however, the leaflet of the

membrane that was initially on the interior (luminal) side ends up on the exterior side: the membrane has inverted its topology.

As a second possibility, it may be instead that outward extended tubules very rapidly grow from the rim of the pore, rapidly consuming the vesicles' surface area. This latter mechanism strikes us as the less likely one, at least with the Au-TTMA systems, because in many cases the pores had already existed for extended periods with no discernible tubules growing from them. It seems to us unlikely that several tubules should emerge rapidly and (essentially) simultaneously after a delay. For the silica/DOTAP system, the images in figure 3.10 are more suggestive of tubules growing from the rim of the pore as you can clearly see tubules growing from a single location on the surface of the vesicles as it shrinks. However, this remains a topic for future investigation.

We anticipate a similar destruction process whenever small spherical particles are added to the exterior of vesicles, provided that the binding energy exceeds the threshold value. On the other hand, if such particles were added to the interior of vesicles or found their way inside through a pore, the same logic would predict outward-growing tubules (consistent with earlier experiments[65,68]) during the shrinkage stage and possibly a pore. The final state should also consist of a network of nanoparticle-lipid tubules, as was found here.

For a broader view of the full parameter space, it is useful to compare the present results to earlier findings that nanoparticles[69] or proteins[109] that bind on the exterior leaflet without wrapping can drive tubules extending outward from the vesicle. This finding was explained by a lateral pressure arising from steric interactions among the particles or proteins, leading to a dilation of the outer leaflet that then forms the convex (outer) surface of the tubule. The previous experimental system[70] consisted of cationic particles with DOPC lipids (i.e., in the weak-binding

regime) and with high enough particle concentration to induce the lateral pressure. In combination with our results, this suggests that systems could be specifically designed to form either outward- or inward growing tubules, pores, and inverted structures, depending on particle shape, concentration, and $\omega a^2/\kappa$.

Section 5: Conclusions

In our experiments and simulations, we exposed charged lipid bilayer membranes to oppositely-charged nanoparticles to understand how nanoparticle adhesion can be used to reshape the bilayer surface, a mechanism that could potentially be used to design novel responsive materials. We have successfully developed a membrane-particle system with tunable double-layer interactions, leading to the ability to form an adhesive network of vesicles (a bulk gel) or to drive a remarkable, catastrophic destruction of each vesicle leading to a network of tubules. The crossover between the adhesion/gel regime and the destruction regime was driven by the particle scale crossover from weak binding/deformation to complete wrapping. With cationic Au-TTMA spherical nanoparticles, this crossover threshold was approximately 4% mole fraction DOPS in sugar solution, or 5 mol% in sugar + 20 mM NaCl. For anionic Ludox silica nanoparticles with no added salt, the crossover threshold was 8% and 7% DOTAP for the two different sizes for particles with a = 11.3 and 12.6 nm. These behaviors were consistent despite the differences in particle size, surface functionalization, and lipid composition. According to our simulations, this threshold corresponds to $\omega a^2/\kappa$ equal to approximately 0.5. It is worth noting that at least in the initial state, interactions are dominated by ω and κ. While tension has a negligible effect since this system is in the limit $\tau a^2/\kappa << 1$.

The gel that we found at low ω is a macroscopically large aggregate of vesicles that form a cohesive, closed-cell network. The networks can support weight (copper beads) for many hours, indicating that they have a finite shear modulus and yield stress. These gels are more than 99% water. Their closed cell morphology is reminiscent of cellular tissue but is unusual among synthetic systems. Since the individual vesicles remain intact within the gel, they should be able to encapsulate multiple species in solution inside the gel. We envisage forming two or more different sets of vesicles, each one encapsulating a different reagent; the vesicles could then be dialyzed, mixed, and then made to form a vesicle gel. The two different species of reagent would not react with one another until the gel is ruptured in some way, causing their release.

Above the threshold lipid composition, nanoparticles were fully enveloped by the membrane, causing the vesicle membrane to be loaded with adhered nanoparticles and ultimately causing destruction of the vesicle. The envelope/destruction regime results in complete and irreversible release of the contents of the vesicle. These results may lead to vesicles that are tailor-made to rupture and release only in response to selected particles (that bind strongly) and not to others. Such a system could be very useful for delivery in myriad contexts.

The results obtained with this tunable system show a unified picture that could explain the wide variety of behaviors reported previously with vesicles exposed to nanoparticles, viruses, proteins, or polymers. Under conditions of matched osmotic strength (as here) and initially low tension ($\tau a^2/\kappa \ll 1$), the deformations are caused by particle adhesion energy per area, which competes with membrane bending stiffness. We found that nanoparticle concentration and membrane permeability do not affect the threshold but do play an important role in the dynamics: if the particle flux is high enough, then the vesicles shrink fast enough to form a long-lasting pore.

CHAPTER 4

THE EFFECT OF CHARGED NANORODS ON LIPID BILAYER MEMBRANES

Chapter 4 presents the results of work measuring the interactions between nano-rods and lipid bilayer membranes. The first section introduces the experiments done, an overview of the results and the major scientific questions being addressed. The second section provides an outline of the methods and materials used to conduct these experiments. Section three presents our detailed experimental findings. Discussion of the results is presented in section four. Lastly section five presents concluding remarks on the results and their significance.

Section 1: Introduction

Here we report the results of a well-defined system of lipid membrane and nanoparticle interactions wherein we can tune the interaction strength, ω, membrane tension, τ, and particle concentration, c_{rod}. For particles, we used anionic DNA origami nanorods that are 420 nm long by 5 nm in diameter. These particles were selected due to their monodisperse nature, uniform charge density and stability at experimental conditions. We used giant lipid bilayer vesicles (GUVs) ranging from 10 -100 μm in diameter composed of a combination of a zwitterionic lipid (DOPC) and a cationic lipid (DOTAP). The binding energy, ω, was tuned by varying the amount of the DOTAP in the membrane, x. We studied the dynamics and steady state of the system using bright-field, dark-field and fluorescence optical microscopy and we used cryo-electron microscopy to image the rods at the nanometer scale. We found that for low x, and thus low ω, and low c_{rod}, particles deformed the membrane into tubules and other shapes For high c_{rod} and low x, we saw

vesicle-vesicle adhesion and the formation of a vesicle-based gel. With higher x we saw a transition into rupture of vesicles simultaneous with vesicle-vesicle adhesion. At still higher x, we found a second crossover to rupture of individual vesicles without vesicle-vesicle adhesion. The process of single vesicle destruction was complex, involving the formation of aggregates, tubules, sudden drops in the vesicle's radius, and a shrinking of the size of the vesicle until final rupture. The sequence of events found in single vesicle destruction were highly repeatable and consistent over a large portion of the state space. To probe for the effects of tension, we also prepared vesicles with excess area by exposing them to a hypertonic solution and observed that the excess area shifted the second crossover. Cryo-TEM images provide the first evidence of membrane-mediated interactions among rods, leading to parallel alignment of membrane-bound rods in some regions of the membrane, and aster-like rod formations and a new mode of deformation in other regions. We present these results in the form of a state diagram and conclude that the two crossovers arise from the two separate wrapping transitions that occur at the single-particle scale. Compared to our earlier study of spherical particles, the rods exhibit many of the same behaviors such as inducing the formation of a bulk vesicle gel at low adhesion and causing vesicle destruction at high adhesion. However, rods have an additional intermediate state where in vesicle adhesion followed by rupture is observed, (Fig. 4.1). Cryo-TEM images also demonstrate in-plane ordering of the rods on the membrane cause by membrane mediated attraction.

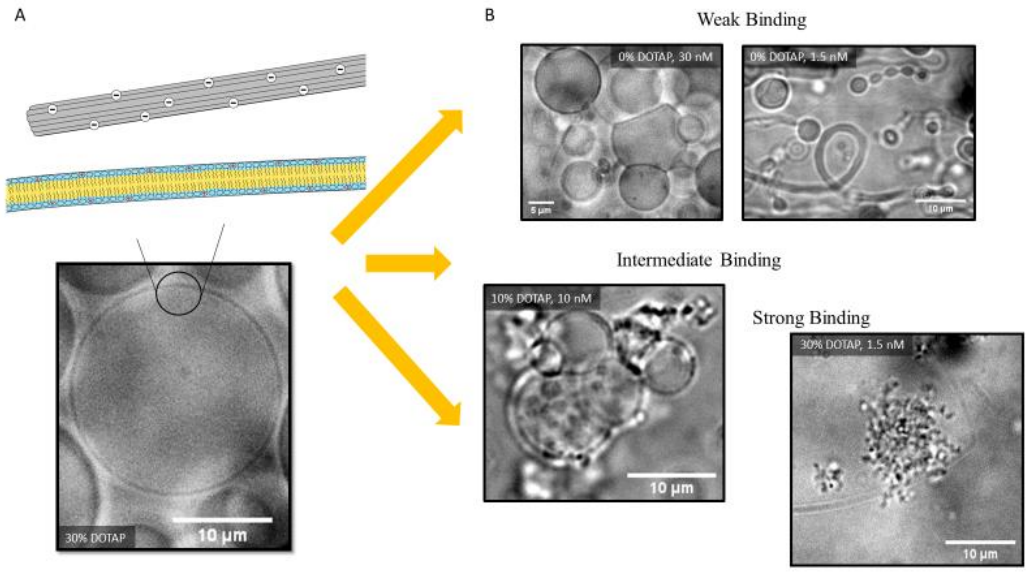

Figure 4.1: Schematic overview of nanorod system

(A) Schematic overview of giant unilamellar vesicles (GUVs) with tunable charge density controlled by the amount of cationic lipid present in the membrane interaction with anionic DNA origami nanorods. The micrograph image shows a GUV composed of 70% DOPC and 30% DOTAP prior to the addition of nanorods. (B) Microscope images of GUVs combined with nanorods with increasing amounts of DOTAP associated with weak, intermediate, and strong binding of particles to the membrane resulting in deformation, adhesion and/or rupture of the vesicles.

It is worth reflecting on and compare to our results with spherical particles described in chapter 3. Theory, simulations, and experiments have shown that when one spherical particle (radius a) binds weakly, it deforms the membrane. The deformation comes from a competition between adhesion energy per area, ω, which competes with the membrane's bending stiffness, κ or tension, τ .[13,14,15,110] With stronger adhesion (when $\omega a^2/\kappa$ exceeds a threshold of order 1), the particle is fully wrapped by the membrane.[13,31,72] When many particles are present, the deformed membrane shape leads to in-plane particle interactions and assembly that can amplify the membrane response and cause large-scale shape reorganization.[1,3,20,97,111,112] Chapter 3 describes the results of our combined experimental and simulation study that demonstrated that spherical nanoparticles binding to vesicles with controlled adhesion strength show a sharp and tunable crossover from binding with weak deformation (leading to adhesion among neighboring vesicles)

to binding and wrapping of particles (leading by a well-defined sequence of stages to destruction of the vesicle).[72]

The results with spherical particles lead us to ask whether less symmetric particle shapes would induce different behavior because the energy cost of bending the membrane changes. Earlier work has shown that rod-shaped particles have more than two wrapping configurations, and that between each is a distinct cross over determined by the same dimensionless ratio scaled by the aspect ratio of the rod. As is the case for spheres theory and simulation predict that the binding and envelopment of the rods by the membrane is dependent on the length, l, particle radius, a, adhesion energy per area, ω, membrane bending stiffness, κ, and tension, τ.[31,53,54] Tension it is not relevant for initial wrap however its effects are seen for higher degrees of wrapping and in the many particle case which will be discussed later. The question we seek to answer is how does the increase in unique regions of curvature for rod shaped particles expand the possible binding configurations of the rod to the membrane and what effect does this have on the bulk interactions in the many particle system.

The ability to tune morphology opens the door to smart responsive membrane-based materials as well as a variety of applications in targeted encapsulation and release. They could be used to motivate the creation of cargo-carrying vesicle gels that rupture when exposed to external stimuli,[113] or for the design of controlled release over extended periods of time. They also provide a remarkably detailed presentation of the phase space defined by ω, κ, τ, and c_{rod}. The wide variety of phenomena observed, and their well characterized dependences make this system an ideal comparison for theory and simulation.

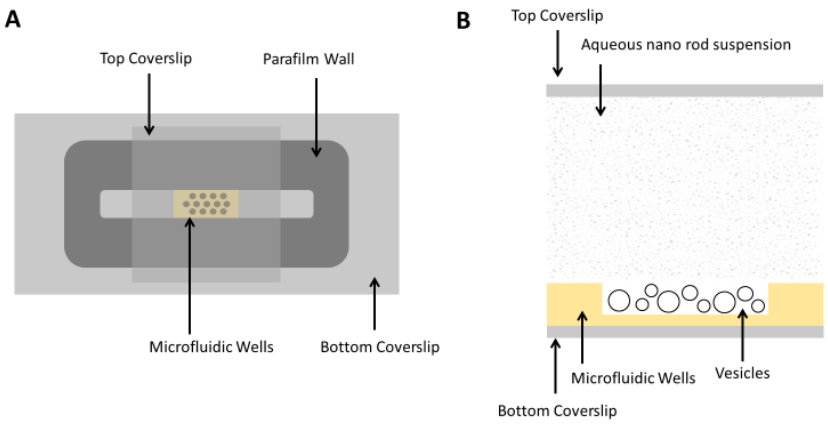

Figure 4.2: Schematic of microfluidic chamber

(A) Top view of the microfluidic chambers used for imaging the dynamics of the nanoparticle/vesicle interactions. (B) side view of a single well.

Section 2: Methods and materials

Giant unilamellar vesicles (GUVs) were formed using electroformation. Details are given in Chapter 2. The membranes were formed from mixtures of a weakly anionic and a strongly cationic lipid. of the former part was composed of zwitterionic mono-unsaturated 1,2-dioleoyl-sn-glycero-3-phosphocholine (18:1 DOPC; Avanti Polar Lipids). To tune the charge density of the membrane a cationic lipid was added to the membrane. Cationic 1,2-dioleoyl-3-trimethylammonium-propane (18:1 DOTAP; Avanti Polar Lipids) was selected as it has the same fatty-acid tale as DOPC (to suppress demixing). In order to visualize the membrane using confocal microscopy we added a small amount of headgroup-labeled lipid 1,2-dioleoyl-sn-glycero-3-phosphoethanolamine-N-(lissamine rhodamine B sulfonyl) (ammonium salt) (Rh-DOPE; Avanti Polar Lipids). Care was also taken to control the osmolarity of the vesicles. Vesicles which above are referred to as balanced were formed in a sucrose solution at 175 mOsm L^{-1} and then diluted in an equal volume of glucose solution at 180 mOsm L^{-1}. The vesicles were then left overnight to sediment as well as equilibrate. Vesicles which above are referred to as floppy were prepared in

the same way initially but where then diluted a second time in a glucose solution at 200 mOsm L^{-1} immediately before experimental observation. The 10% difference in the interior and exterior osmolarity resulted in floppier vesicles with excess area.

Anionic DNA Origami nanorods were utilized in our experiments. The rods where formed from six-helix DNA-bundles into rods that were 420 nm by 6 nm with right-handed twist (360 degrees).[87] The rods were specifically designed with strategically placed Thiamine groups and then exposed to ultraviolet light which induces cross-links between adjacent pyrimidines in a method known as Thiamine Welding.[114] The rods were synthesized and finally stored in a 1xFOBMg5 buffer composed of 5mM TRISm 5mM NaCL, 1 mM EDTA and 5 mM MgCl1 at pH 8. The final concentration of rods was 150 nM. From this stock solution rods were diluted using the same sucrose and glucose solution used to create and dilute the vesicles. The specific concentration is denoted per experiment. More details can be found in chapter 2.

Experiments were conducted in custom flow chambers with microfluidic wells which enabled the real time visualization of particle membrane interactions. The experiment chambers also allowed for careful control of the bulk solution, see Fig. 4.2. Vesicles were injected into the chambers and then allowed to sediment in to PDMS wells at the bottom of the chamber. Once the vesicles had sedimented the bulk fluid of the chamber was replaced with a solution at the relevant concentrations required for specific experiments. The whole chamber was mounted to an optical microscope and interactions were observed from beneath. See chapter 2 for more information.

Brightfield and Darkfield images were acquired using a CoolSnap HQ2 camera (Roper Scientific) and Zeiss 100x oil immersion objective with an adjustable 1.4 -.7 NA. Confocal images were taken with a custom modified VT-Infinity3 (VisiTech) scanning pinhole confocal system.

The camera used was a Hamamatsu ORCA-flash2.8 with a Zeiss 100x oil immersion objective (1.4 NA) and VOXCell software.

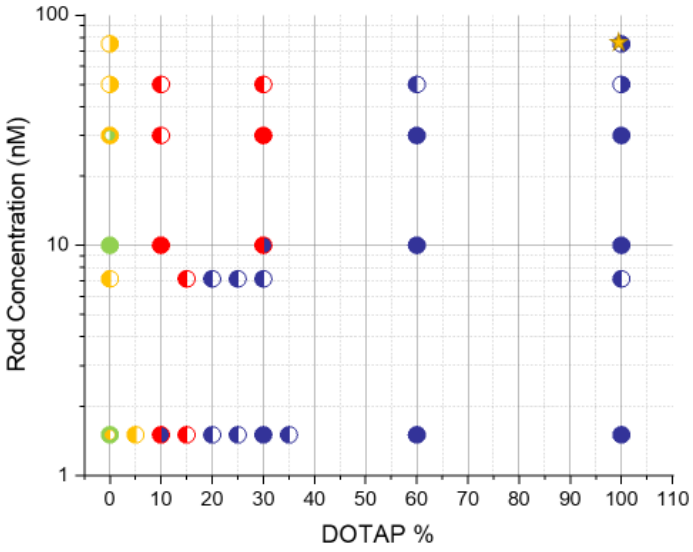

Figure 4. 3: State diagram, nanorods

State diagram of the observed interactions of GUVs with DNA Origami nano rods. Increasing the DOTAP % is directly correlated to an increase in the adhesion strength between the particles and the membrane. Green denotes vesicles in the DXX domain (Deformation, no adhesion, no rupture). Yellow denotes vesicles in the DAX domain (Deformation, Adhesion, no rupture). Red denotes vesicles in the DAR domain (Deformation, Adhesion, Rupture). Blue denotes vesicles in the DXR domain (Deformation, no adhesion, Rupture). Right-handed semicircles denote results for vesicles that are osmotically balanced. Left-handed semicircles denote results for vesicles that are floppy due to exposure to a hypertonic solution. Full circles represent results for both balanced and floppy vesicles.

Section 3: Results

In this section, we describe the phenomenology observed due to the deformation of lipid bilayer membranes by DNA Origami nanorods. This description is divided into six sections. The first section provides an overview of the phenomenology and presents a state diagram of our results (Fig. 4.3). The next four described the four primary behaviors depicted in our state diagram. In the final subsection we present results from cryogenic transmission electron microscopy (cryo-TEM)

micrographs for rods in the strong binding regime. Finally, in the Discussion section, we present a hypothesis for the underlying mechanisms and compare to previous literature.

Subsection 3.1: Overview of the phenomenology: regimes of deformation, adhesion, and rupture

We studied the response of vesicles in situ after the introduction of anionic DNA origami nanorods. The vesicles were captured and confined using microfluidic wells and the bulk suspension was replaced with a fixed concentration nanorod solution. This allowed us to characterize the effect of rod concentration on interactions and vary the concentration in a controlled fashion. Increasing the concentration of nanorods effectively increases the binding rate of nanorods onto the membrane. We also tuned the adhesion energy per area, ω, between the lipid bilayer and the oppositely charged nanorods by increasing the amount of cationic lipid content in the vesicles and thus tuning their average surface charge. To probe the dependence on membrane tension, τ, we examined two populations of vesicles, those that were osmotically balanced (referred to as balanced) and those that where saturated in a hypertonic solution (referred to as floppy). Care was taken to ensure that osmotic shock did not play a role in the processes described here. In control experiments without rods we observed only intact vesicles without adhesion. In the presence of rods, dark-field microscopy provided direct evidence that rods bound to the membrane (Fig. 4.4).

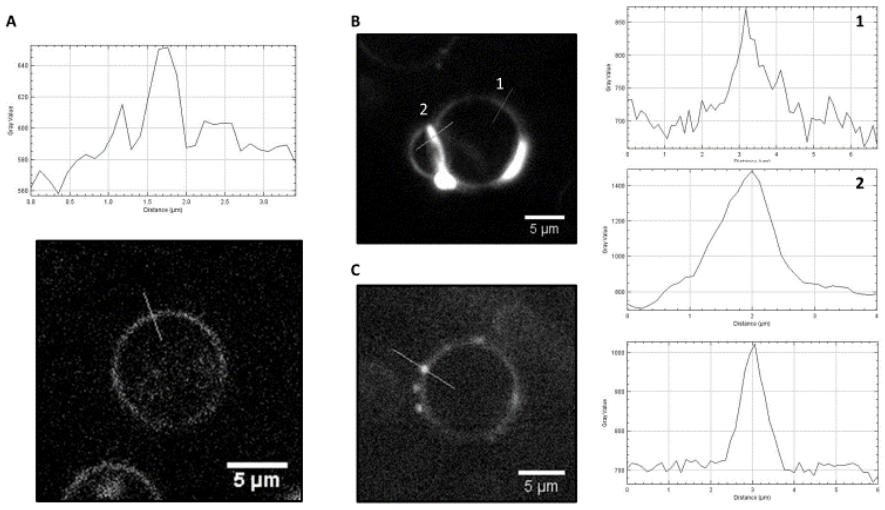

Figure 4.4: Darkfield micrographs, nanorods and vesicles

Darkfield micrographs of nanoparticles binding to 20 mol % DOTAP vesicles and plots of associated gray scale values. (A) Image of a single vesicle and the intensity profile along the line intersecting the membrane for a vesicle before nanorods have been added. (B) Image of two vesicles adhered to one another and the plot of the intensity across the free edge of one of the vesicles and along the line bisecting the intersection of the two vesicles. (D) Image of a vesicle with dark mobile aggregates and the plot of the intensity across one of these aggregates.

Fig. 4.3 depicts a state diagram for the system, showing the behavior in steady state depending on c_{rod}, x, and excess area. Figure 4.5 depicts the same state space of domains as well as outlining the subdomains where specific morphologies are observed. In all cases, we observed some combination of three distinct behaviors and the presence or lack of these behaviors defined four primary regimes in the state diagram. The primary responses to the binding of nanorods to the vesicles are membrane deformation (D), vesicle-vesicle adhesion (A), and vesicle rupture (R). Remarkably, the onsets of these behaviors were sharply defined in Fig. 4.3, so that we could define transitions between regimes corresponding to the various behaviors. At low DOTAP concentrations we observed the DXX and DAX regimes where vesicles deformed in shape and adhered to one another but remained intact after the introduction of rods. At higher DOTAP concentration, x, we found a crossover to the DAR regime, wherein vesicle rupture and destruction were observed. With still higher, x, we found a second crossover to destruction of individual vesicles with no adhesion (DXR). For intermediate DOTAP (10 -30 mol%), increasing the rod

concentration, $c_{rod,}$ led to a crossover from DXR to DAR, corresponding to the onset of inter-vesicle adhesion. We also found that increasing the excess area in the vesicles (making them floppy at the start) shifted the system toward DXR rather than DAR, and hence tended to favor singe-vesicle destruction.

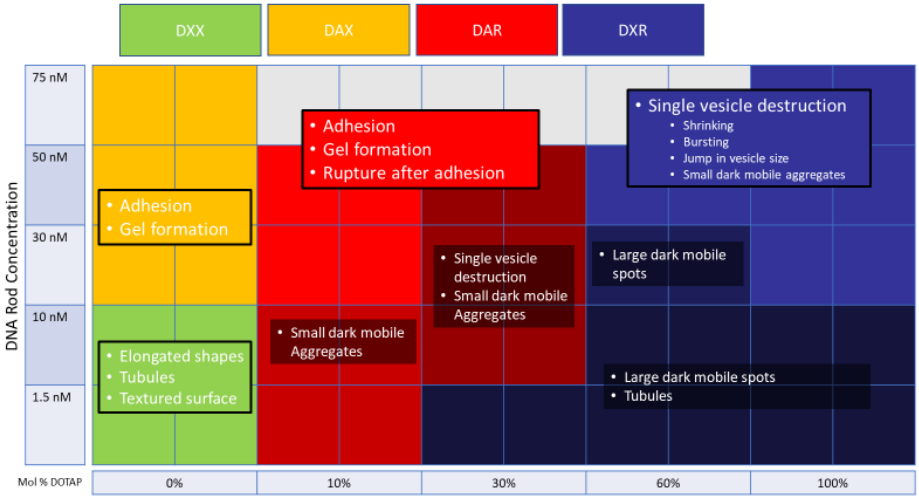

Figure 4.5: State diagram subdomains

Grid representation of the state space with text and colors depicting the domains and subdomains of morphologies we observed. Text outlined in black are universal features of the domain. Different shades represent different subdomains and the smaller text boxes described morphologies that are unique to those subdomains. Green denotes vesicles in the DXX domain (Deformation, no adhesion, no rupture). Yellow denotes vesicles in the DAX domain (Deformation, Adhesion, no rupture). Red denotes vesicles in the DAR domain (Deformation, Adhesion, Rupture). Blue denotes vesicles in the DXR domain (Deformation, no adhesion, Rupture).

Subsection 3.2: DXX regime: deformation of individual vesicles

For membranes without DOTAP and low rod concentration we saw nanorods binding to vesicles, leading to deformation of the vesicles without vesicle-vesicle adhesion. Particles adhered to the vesicles reconfiguring the membrane into three morphologies: elongated shapes, tubules, or dense textured surfaces on the vesicles (Fig. 4.6, green region). The elongated configuration was observed for the majority of vesicle in this domain. Previously spherical vesicles were elongated into tubular configurations that were sometimes as narrow as only a few μm in diameter. Some vesicles were dramatically elongated while others developed only mild elongation with aspect

ratios closer to 2:1, while still others kept their spherical shape. Tubules defined here as narrow tubular protrusions from roughly spherical vesicles, were also very common for both spherical and elongated vesicles. We observed both internal and external tubules with external tubules being the most common. These tubules were stable for the duration of the experiment. The third morphology seen in the DXX regime (1 or 2 vesicles out of 100 in a typical field of view) was spherical vesicles with highly textured surfaces. Two examples are given in the DXX portion of Fig. 4.6. The patterned surface was only seen on spherical vesicles and was never accompanied by tubules. The pattern was stiff, barely fluctuating or deforming. The elongated shapes, tubules and textured surface were observed for both balanced and floppy vesicles without any discernible dependence on tension.

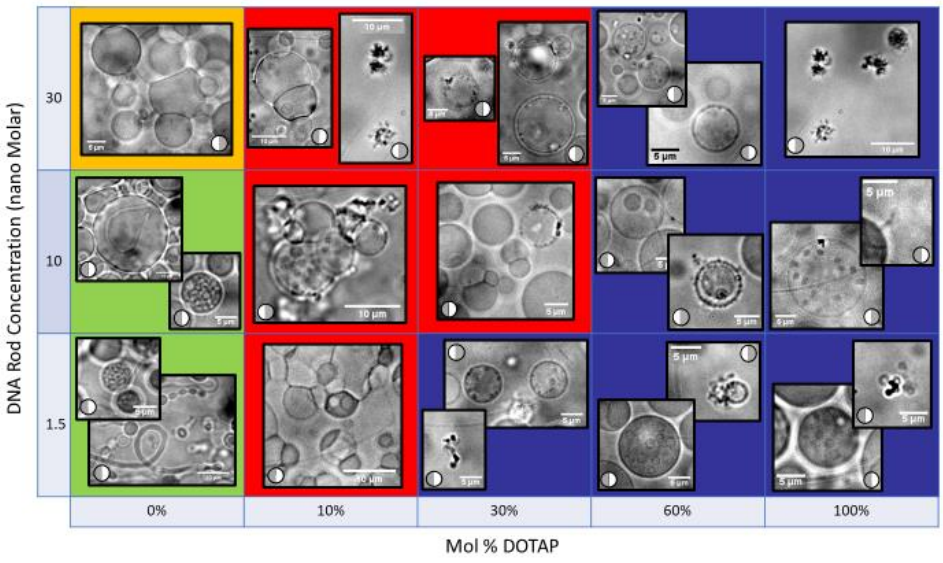

Figure 4.6: State diagram of morphologies, nanorods

Pictorial representation of the state space with micrograph images depicting the most common observed phenomena in each domain. Green denotes vesicles in the DXX domain (Deformation, no adhesion, no rupture). Yellow denotes vesicles in the DAX domain (Deformation, Adhesion, no rupture). Red denotes vesicles in the DAR domain (Deformation, Adhesion, Rupture). Blue denotes vesicles in the DXR domain (Deformation, no adhesion, Rupture). Right-handed semicircles denote results for vesicles that are osmotically balanced. Left-handed semicircles denote results for vesicles that are floppy due to exposure to a hypertonic solution. Full circles represent results for both balanced and floppy vesicles. Scale bars length is denoted in each micrograph.

Subsection 3.3: DAX regime: deformation and vesicle-vesicle adhesion

In other samples at low DOTAP, and particularly at higher c_{rod}, we found adhesion between vesicles as well as deformation (DAX). The membranes of neighboring vesicles adhered to one another due to the bound nanorods forming an adhesive bridge between vesicles. Darkfield micrographs indicate where nanoparticles have bound and aggregated on the membrane. The image intensity comes from light that is scattered in the sample plane. The more material that is present in the sample plane the more light is scattered as is the case when comparing bare membrane verses membrane coated with nanoparticles. Fig. 4.4 shows examples of darkfield images and their corresponding intensity profiles measured in a line across the membrane. Fig. 4.4 also shows strong light scattering at the adhesion sites between vesicles caused by the nanorods accumulating at these junctions due to their ability to bind to both membranes. The adhesive contact area grew over the course of a few minutes until a steady state was reached (Fig. 4.6, yellow region). In samples where the vesicle concentration was high enough, adhesion led to a solid network of fluid vesicles which we call a "vesicle-gel".[72] The structure of this gel was like that of a dry soap foam with vesicles forming polyhedral configurations when confined by their neighbors. In the case of the vesicle-gel, however, the interior and the continuous phases are both aqueous.

For some trials with 100 mol % DOPC we observed both DAX and DXX behavior at the same rod concentration. No clear boundary between the DXX and DAX was determined for 100 mol% DOTAP. We attribute this variation to the fact that different samples may have different rates of mixing in the rods or have different concentrations of vesicles so that the rates of binding and vesicle-vesicle adhesion could vary. By contrast the other behaviors reported here (DXR, DAR) were highly repeatable.

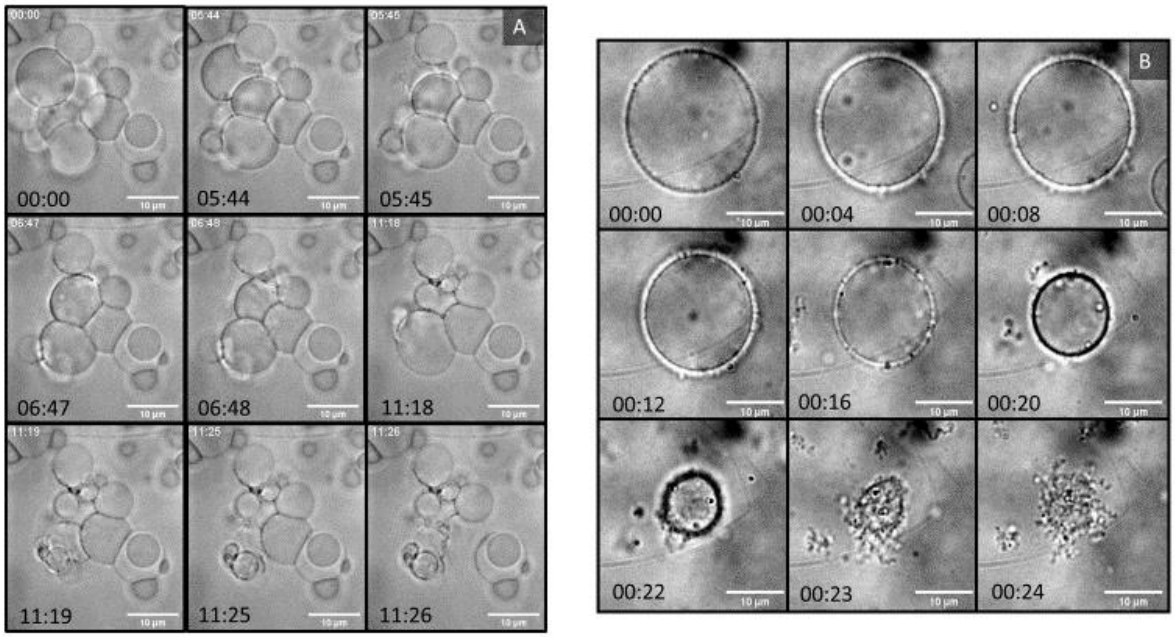

Figure 4.7: Montage of destruction, nanorods

(A) A montage of brightfield micrographs showing the disruption process for vesicles in the DAR domain. The vesicles contained 10 mol% DOTAP and were exposed to DNA origami rods at 1.5 nM. (B) A montage of brightfield micrographs showing the disruption process in the DXR regime. The vesicle contained 30 mol% DOTAP and were exposed to DNA origami rods at 1.5 nM. Scale bars are all 10 microns.

Subsection 3.4: DAR regime: deformation, vesicle-vesicle adhesion, and rupture

At intermediate DOTAP content (10-30 mol%), we observed vesicle-vesicle adhesion followed by vesicle rupture (Fig. 4.7). Rupture involved the total collapse of the vesicle's spherical structure, typically in a bursting or shrinking event. In the DAR regime, the rupture process always occurred simultaneous with or after vesicle-vesicle adhesion, resulting in the accumulation of membrane-nanorod aggregates attached to vesicle aggregates.

The progression of events in this regime consisted of first the formation of the vesicle gel within the first few minutes of the experiment. Over time, individual vesicles in the gel cluster burst suddenly. The destruction process was most often very fast (<500 ms; see Fig. 4.7(A)) but a few events (< 1 out of 1000) happened more slowly over a few seconds. The fraction of vesicles

destroyed and the rate of vesicle destruction events both varied with c_{rod} and x. Fig. 4.8 shows qualitatively how the rate of destruction varies with c_{rod}.

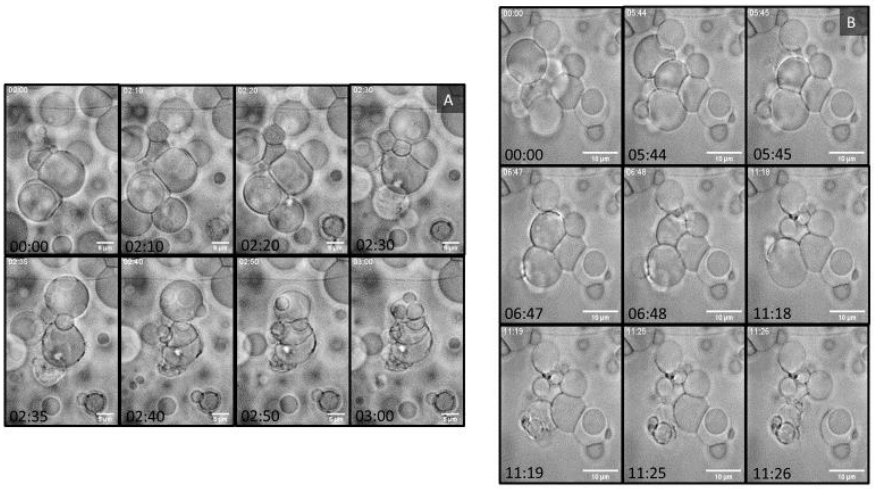

Figure 4.8: Montage of vesicle gel destruction

(A) A montage of brightfield micrographs showing the disruption process for vesicles in the DAR domain. The vesicles contained 10 mol% DOTAP and were exposed to DNA origami rods at 10 nM. (B) A montage of brightfield micrographs showing the disruption process in the DXR regime. The vesicle contained 10 mol% DOTAP and were exposed to DNA origami rods at 1.5 nM. Scale bars included in micrographs

In some vesicles within DXR, we could see dark aggregates that diffused on the surface of the vesicles. These dark mobile aggregates were enriched in rods (as is clear from the scattering) and were too small for us to resolve their size (Fig. 4.4 D). These aggregates were visible in samples with x = 10 mol% and $c_{rod} \leq 10$ nM but not when $c_{rod} > 10$ nM.

The DAR regime is also dependent on membrane tension as well as rod concentration. The dependence on rod concentration is plainly seen for the case of vesicles with 30 mol % DOTAP. Here there was a transition from DXR to DAR by increase the concentration of rods from 1.5 nM to 10 nM. There is also a transition from DAR to DXR at 10 mol % DOTAP and 1.5 nM of rods as well as 30 mol % DOTAP and 10 nM of rods when you use floppy vesicles with excess area rather than balanced vesicles. The dependence on rod concentration and available membrane area may be hinting at similar requirements on the membranes tension verses the binding strength of

the rods to the membrane. No other membrane deformation or systematic variation of morphologies were found in samples in the DAR domain.

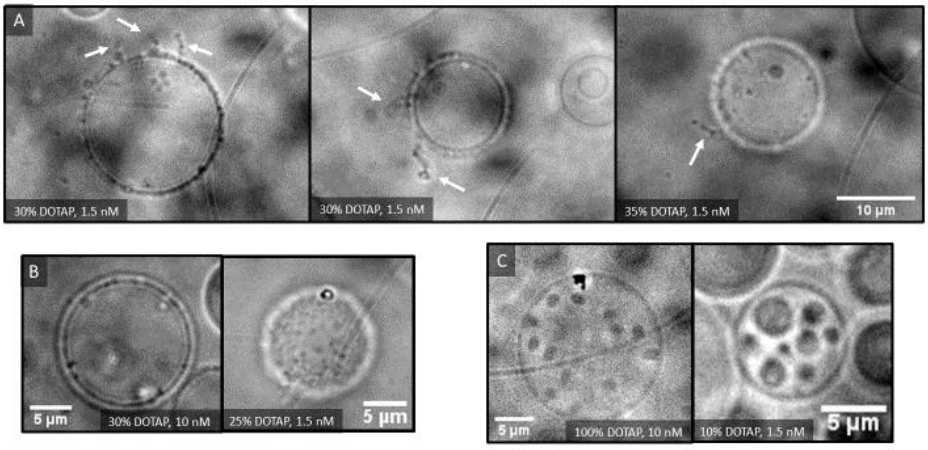

Figure 4.9: Morphologies

(A) The first two images depict brightfield micrographs of vesicles containing 30 mol% DOTAP. The third image was taken using confocal microscopy and is of vesicles containing 60 mol% DOTAP. All three images show examples of external-facing tubules and are within the DXR domain. (B) Brightfield micrographs of vesicles containing 25 mol% DOTAP. Particle aggregations are clearly visible as dark mobile spots. These aggregates are typical for vesicles in the strong binding regime. (C) Brightfield micrographs of vesicles containing 100 mol% and 10 mol% DOTAP. Large mobile spots are observed on the surface of the vesicles. This behavior is seen for vesicles with low rod concentrations.

Subsection 3.5: DXR regime: deformation and rupture

At still higher DOTAP content, we observed a crossover to a new behavior, consisting of destruction of individual vesicles *without* vesicle-vesicle adhesion. In this DXR regime, vesicles were destroyed individually in a multi-stage process (Fig. 4.7B). We emphasize that the concentration of vesicles was the same throughout the state diagram and that vesicles had ample opportunity to adhere. We regularly observed vesicles colliding with each other, being pushed into one another via convective flows or layered on top of one another without any evidence for vesicle adhesion. The absence of vesicle-vesicle adhesion indicated a true lack of adhesive forces.

The process of destruction in the DXR domain was common for hundreds of different vesicles over dozens of different samples varying in lipid composition, rod concentration and membrane tension. During the process of destruction, we observed no change in vesicle morphology for a period of time ranging from seconds for high particle concentrations and tens of minutes for low particle concentration (more particles resulted in a faster response), followed by a sudden drop in size, and then immediately followed by a slow and steady decrease in size until final rupture. Starting radii were typically 5-25 μm and the magnitude of the sudden drop ranged from 1-10 μm in roughly 500-1000 ms. In a minority of cases, the vesicle did not survive this sudden drop in radius and instead ruptured at this step. Most vesicles, however, survived the initial drop then showed a steady decrease in the radius over a typical duration of several seconds to minutes. The rate of shrinkage depended on x and c_{rod}, this dependence will be discussed further below. Within a given field of view, vesicles close to each other tended to shrink at similar rates. As the vesicles shrank, they developed nanorod-rich dark mobile aggregates which diffused along the surface of the vesicle. (Some vesicles had dark mobile aggregate formation before the jump, but the feature was universal after the jump.) In cases of low rod concentration (< 30 nM) roughly one in 100 vesicles developed tubules in addition to the dark mobile aggregates (Fig. 4.9A) Finally, the vesicles underwent complete destruction, wherein at some small radius the vesicles unfurled into a contorted mass of lipid membrane and nanorods with tubule-like tendrils at its periphery. This process is outlined in Fig. 4.7. Examples of the final form of the lipid-nanorod mass are included in Fig. 4.6 for various combinations of DOTAP content and rod concentration.

Within the DXR regime, the sequence of steps did not depend on vesicle size, lipid composition, or membrane tension. In rare cases, the vesicle burst immediately after the sudden drop in radius (no discernible shrinkage process). In other rare cases, we observed the slow

shrinkage and spots but no sudden drop in radius preceding it; in such cases the radius drop might have happened out of frame.

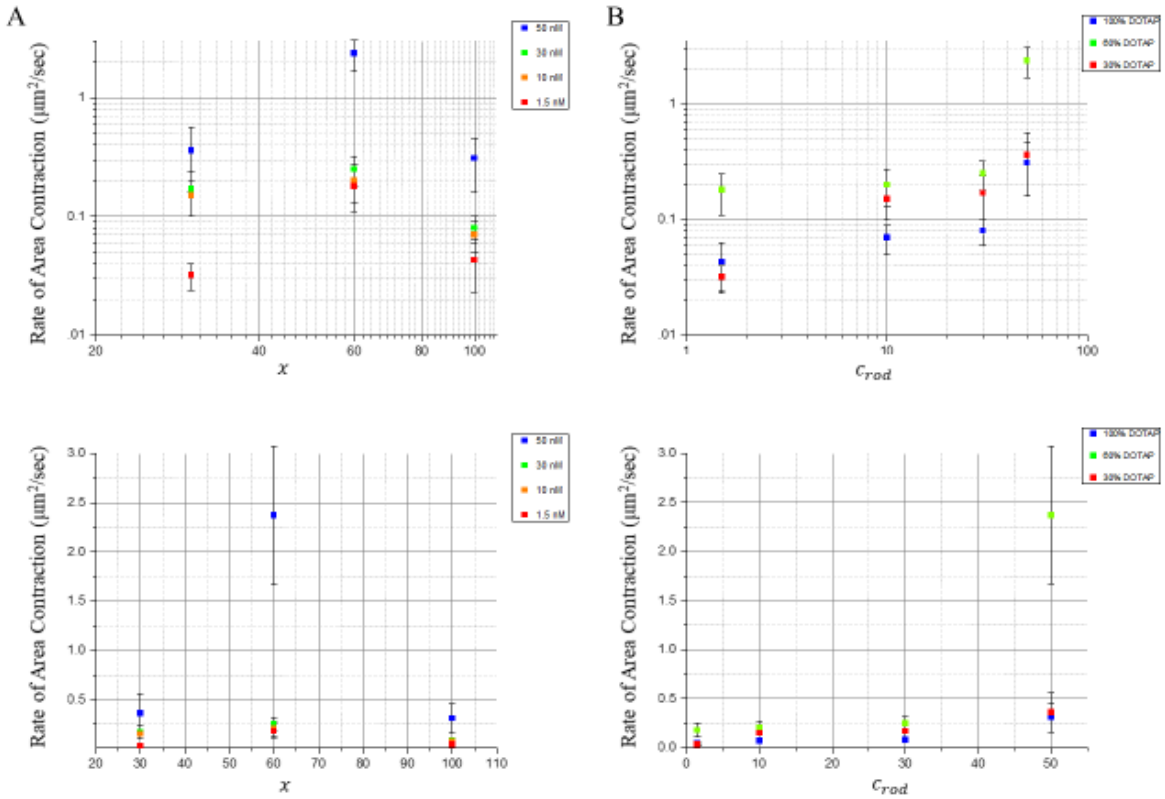

Figure 4.10: Average rate of destruction, nanorods

(A) Plots in the first column depict the average rate of area contraction (μm²/s) versus the mol% DOTAP, *x*, in the membrane for vesicles being destroyed via the binding of nanorods. The colors correspond to the concentration of nanorods in solution: blue for 50 nM, green for 30 nM, orange for 10 nM and red for 1.5 nM. (B) Plots in the second column depict the average rate of area contraction (μm²/s) versus the concentration of rods, c_{rod}. The colors correspond to the mol % of DOTAP in the membrane: blue for 100 mol %, green for 60 mol % and red for 30 mol %.

The average rate of area contraction (Fig. 4.10) was measured for vesicle populations of 30, 60 and 100 mol% DOTAP and rod concentrations of 1.5, 10, 30 and 50 nM. The average rate of contraction was found by tracking the radius of the vesicle frame-by-frame during the shrinking process after the jump and before final rupture (Fig. 4.11). It was observed that the rate of shrinkage depended both on *x* and c_{rod} (Fig. 4.12). For higher c_{rod}, the rate of shrinking increased universally for all DOTAP fractions measured. The dependence on *x*, was found to be nonmonotonic with the fastest shrinkage rates being found at 60 mol % DOTAP across all rod concentrations. The fastest

rate observed was 2.4 ± 0.7 μm^2/sec for 60 mol% DOTAP and 50 nM of rods. The Lowest rate observed was 0.03 ± 0.008 μm^2/sec for 30 mol% DOTAP and 1.5 nM of rods. These rates are much slower than those reported in chapter 3 for spherical particles which averaged around 35 μm^2/sec. Additionally pores only formed in the case of spherical particles when the rate of shrinking exceeded 300 μm^2/sec. This differences in rates may account for absence of pores in the vesicle destruction process for rod shaped particles.

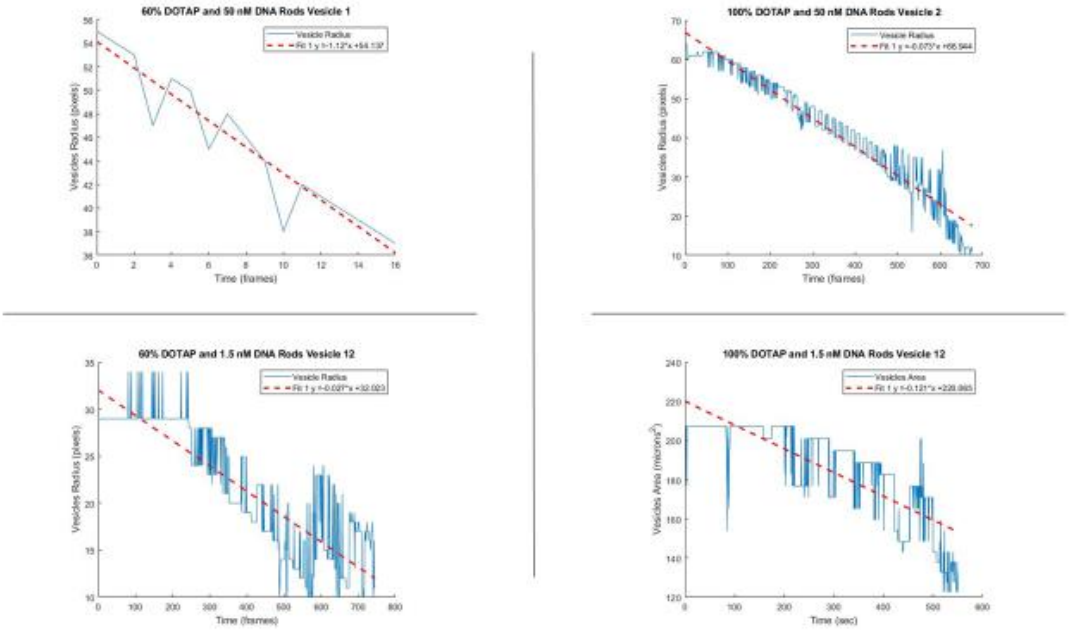

Figure 4.11: Vesicle Radius vs Frames

Representative plots of the vesicle radius in pixels verses frames recorded, (blue). The radius was measured using the Hough circular transform. A linear fit is shown as a reference (red).

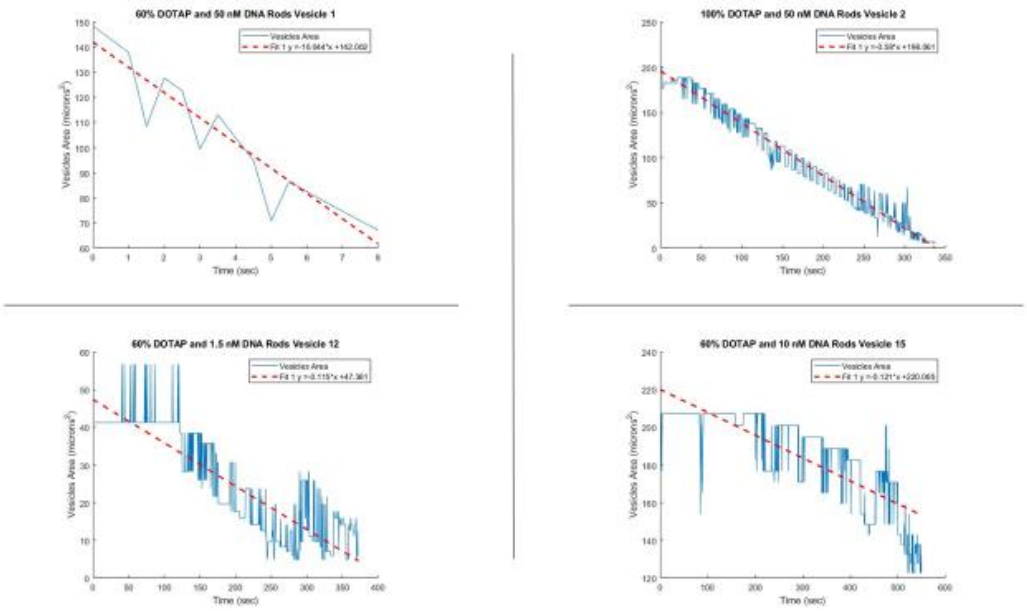

Figure 4.12: Vesicle Area vs Time

Representative plots of the vesicle area in μm^2 verses seconds, (blue). The area was calculated from the radius measured via the Hough circular transform. A linear fit is shown as a reference (red).

We now describe the main structural features in more detail, *i.e.*, the dark mobile aggregates, large (~2 μm) mobile spots, tubules, and the final unfurled rod/membrane structure.

The dark mobile aggregates described above were similar in size to the microscope resolution limit and so their true size cannot be measured accurately. The dots appeared bright under dark-field imaging indicating that they were enriched with nanorods (Fig. 4.4). We never observed particle aggregates in solution and only found these features on vesicles that experienced destruction, the DAR and DXR regimes. These observations indicate an attractive interaction between the like charged nanorods that was mediated by the deformed membrane. (Further evidence for membrane-mediated attraction came from cryo-EM, described below.) Throughout the destruction process these aggregates remained mobile on the vesicles' surfaces. As the vesicles shrank the concentration of aggregates increased with no observable change in their size. Every

vesicle in the DXR regime that underwent destruction during the duration of the experiment had dark mobile aggregates in conjunction with surface shrinking.

Large mobile spots were observed in some DXR vesicles with low to moderate c_{rod}. These spots were approximately 2 μm in diam. with dark edges. We observed them forming, fading, and diffusing on the surface of some vesicles prior to the drop in radius (Fig. 4.9C). We observed them diffusing freely on the surface of the vesicle for a period of several minutes. They could be seen fading in and out on the surface of the vesicle, but no merging events were observed. They differed from the small dark aggregates in several respects: by their larger size, weaker optical contrast, non-circular shape, their presence prior to the drop in radius and their disappearance after the radius drop. Their appearance and then disappearance also distinguished them from internalized vesicles (which we sometimes observed and were quite distinct). These spots occurred on a minority of vesicles at low c_{rod}; by contrast, the dark aggregates were common among all vesicles in DXR. These spots were never observed under darkfield indicating that the density of nanorods in these spots must be similar to the average density of rods on the surrounding membrane surface and much lower than the density of rods in the dark aggregates described previously. These features indicate some larger scale structure formed due to membrane mediated interactions of the nanorods, which we will discuss below. These spots were not a universal behavior of vesicles in the DXR regime and seemed to require slower binding of nanorods onto the membrane to form.

Tubules formed in the DXR regime only for $c_{rod} < 30$ nM. A similar trend was found in the DXX regime: tubules only formed at low c_{rod}, suggesting that tubule formation can be frustrated by the presence of too many nanorods. The lack of tubules in the DAR and DAX domains also suggests that tubule formation was frustrated by the formation of the vesicle gel. The reason for these restrictions on tubule formation will be explored in the Discussion section. In contrast to

tubules observed in the DXX domain, tubules formed in the DXR domain were small, 2-10 μm in length, 1-2 μm in diameter and almost exclusively external.

The final stage of the membrane disruption process was complete vesicle destruction, resulting in a contorted mass of lipid and nanorods with small protrusions on the periphery (*e.g.*, Fig. 4.6). The typical diameter was approximately 2-5 μm. There was no evidence of correlation between vesicle size or DOTAP content and the final structure. There was some variation in the structure of the final mass as a function of c_{rod}: when c_{rod} = 75 nM, the masses were more compact with smaller external protrusions. Additionally, for low rod concentrations the final mass was less compact and more likely to be slightly elongated (Fig. 4.6).

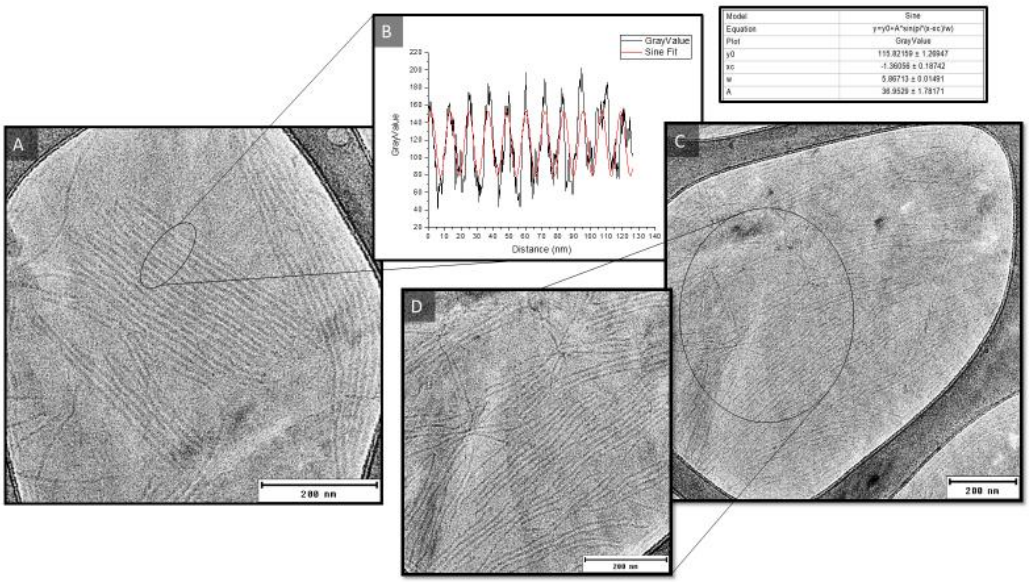

Figure 4.13: Cryo-TEM nanorods on membrane

Cryo TEM images of (A) DNA origami nanorods bound to 100 mol% DOTAP destroyed vesicles incubated for five days. When bound to the membrane the nanorods form bundles and demonstrate in-plane ordering. (B) The pixel intensity is be plotted verses the distance perpendicular the length of the rods to find the typical rod center-to-center spacing of 11.7 ± 0.03 nm. (C & D) DNA origami nanorods bound to 100 mol% DOTAP destroyed vesicles incubated for five days. Defects in the form of nanorod asters were found among the aligned rods bound to the membrane.

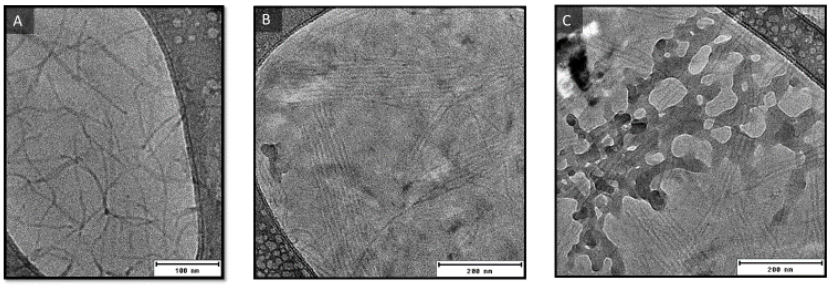

Figure 4.14: Cryo-TEM nanorods control and additional morphologies

Cryo TEM images of (A) DNA origami nanorods in aqueous phase, control. (B) DNA origami nanorods bound to 100 mol% DOTAP destroyed vesicles. (C) DNA origami nanorods bound to 100 mol% DOTAP destroyed vesicles exhibiting high degrees of membrane distortion.

Subsection 3.6: Cryo-electron microscopy at high DOTAP fraction and rod concentration

To image the rods with nm-scale precision, we used cryogenic transmission electron microscopy (cryo-TEM) to directly view the membrane-rod morphologies at the nanoscale. The cryogenic preparation preserves the arrangement of the rods and membrane, so that these images give a high-resolution snapshot of the structure. Fig. 4.13 depicts cryo-TEM micrographs of a sample with 100 mol % DOTAP and c_{rod}= 75 nM and left in suspension for 4 days. We obtained control images by observing regions of the grid that were devoid of sample material. These areas presented only amorphous ice suspended by the lacey carbon grid allowing us to compare the contrast against areas with sample. This confirmed that the background intensity value behind the rods in our sample images was in fact the lipid membrane and notice as they were significantly darker. It should also be noted that the dark curved edges surrounding regions with rods are the edge of the lacey carbon that composes the grid. The gaps in the mesh are truly holes with only the supported film of the sample (Fig. 4.14).

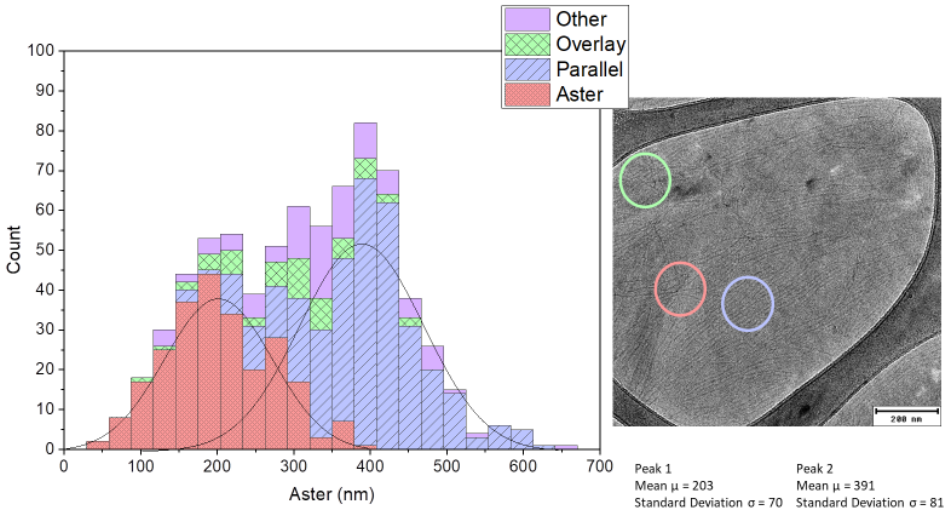

Figure 4.15: Histogram of nanorod alignments

Histogram of the population of each type of rod-membrane binding configuration. Four configurations were observed: parallel (blue), aster (red), overlaid (green), or other (purple). Examples of overlay, parallel and aster are circled in the micrograph with their respective color codes.

The images show nanorods bound to the membrane with high surface coverage and in-plane ordered patterns of two distinct and common types: parallel rafts and radially oriented asters. We defined parallel rafts as consisting of nanorods where at least half the length lay parallel to another rod that was within 10 nm. Rafts were typically composed of roughly a dozen evenly spaced rods aligned approximately tip to tip. The gap between rods in the rafts was found by measuring the intensity value along the width of the raft and then fitting with a sinusoidal function. The center-to-center spacing of the rods observed was 11.7 ± 0.3 nm, (Fig. 4.15 B). In other areas of the sample, we saw a different form of in-plane ordering: asters-like arrays. Nanorods in asters were defined by having one end within a small circular region of the sample (roughly 10 nm across) with the rod extending radially outward from that point. The average length of rods within the asters was observed to be 203 $\pm$ 25 nm, half the full length of the rods.

Fig. 4.16 shows a histogram of the population of each type of rod configurations in the sample with parallel being the most common and asters the second. To account for all the observed rods, we added two additional categories: overlaid rods were those that lay across parallel- aligned

rods. These were readily identified as a single rod lying askew across a bulk of rods. The last case includes all the others, primarily rods that were isolated from other rods. What is remarkable about all these configurations is that these rods were like-charged and should repel each other. Fig. 4.14 shows a Cryo TEM micrograph of the same nanorods in solution without membrane. These rods had random orientation with respect to each other. The existence of organized structures and rod packings is strong evidence for membrane mediated attractive interactions between the rods. We return to this point in the Discussion.

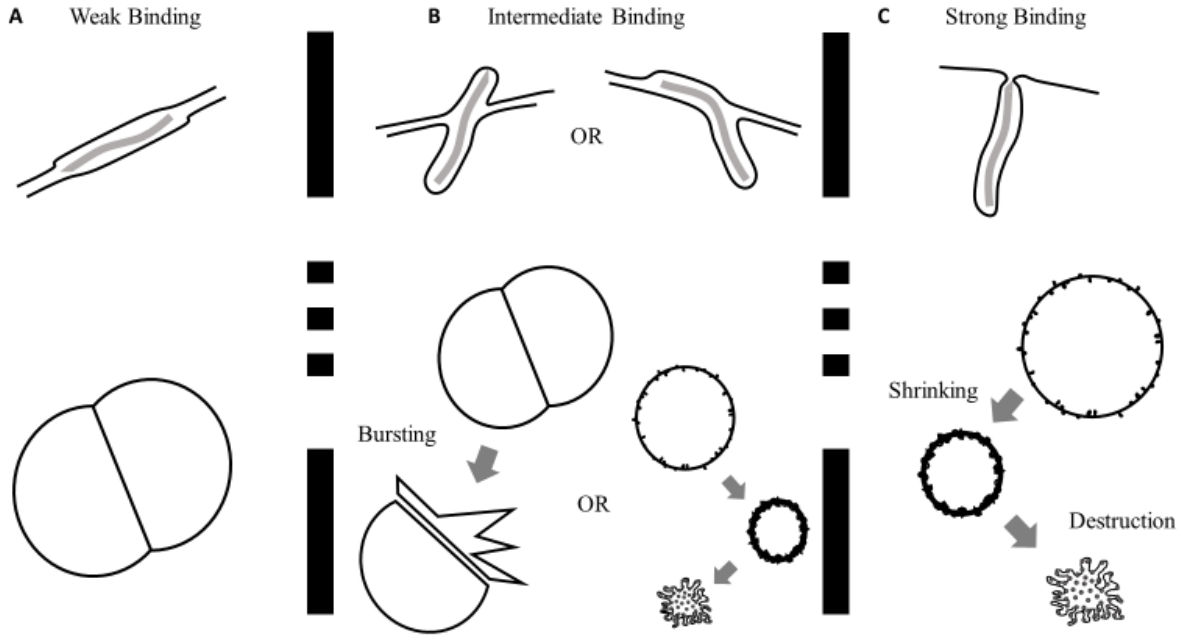

Figure 4.16: Illustration of wrapping of nanorods

Illustration of the wrapping configuration of rods to the membrane and their possible association with bulk phenomena observed.

Section 4: Discussion

Our results show that nanorod binding induces a variety of membrane morphologies, determined by particle-membrane adhesion strength (DOTAP fraction), particle concentration, and membrane tension (controlled by osmolarity). The primary behaviors observed were

membrane deformation (D), vesicle-vesicle adhesion (A), and vesicle rupture (R). We observed well-defined regions in parameter space with these behaviors and sharp transitions between them Within these well-defined regions, we saw deformed membrane morphologies such as tubulation, textured surfaces, small dark aggregates, and large aggregates.

The most prominent features of our observations arise from binding of the rods to the membrane driven by the electrostatic double-layer attraction between them.[72,115,116,117,118] We tuned the adhesion energy per area, ω, between particles and the membrane by means of DOTAP fraction, *x*. Direct evidence of particle adhesion is provided by darkfield experiment (Fig. 4.4), which show increased brightness on the surface of vesicles after the introduction of rods. We note that rods also bound to 100 % DOPC vesicles (x=0) and caused deformation. This seems surprising in view of findings that DOPC vesicles have a slightly negative electrostatic (zeta) potential of -9 mV (electrophoretic mobility with 0.1 mM NaCl)[73] and might therefore be expected to repel the negatively charged nanorods. We attribute the binding in this case to the static dipole of the zwitterionic PC headgroup, which can reorient to attract charged objects of either sign.[74] Previously we found that anionic silica particles were also able to bind to DOPC vesicles.[72,75,76] We will return to quantitative estimates of ω and *x*.

When a rod binds, the membrane bends around it to increase the adhesion area. This deformation leads to the observed interactions among the rods (Fig. 4.10) and leads to further deformations as reported in Fig. 4.3. The membrane deformation can be explained from a continuum approach, in which the energy of rod-membrane adhesion competes with the energy cost of bending and stretching the membrane and the loss of entropy when a free rod binds to a membrane. The energy of bending the membrane can be determined via the Helfrich model[119] and depends on the size and shape of the particle.[13,28] In the case of perfectly rigid rod-shaped

nanoparticles, simulation predicts three wrapping configurations: binding, shallowly wrapped, deeply wrapped, and completely wrapped in the case of rounded rods with small aspect ratios (length over width ranging from 1-3).[31] The existence of three wrapping configurations is ascribed to the inhomogeneous curvature distribution on the nanoparticle surface. The dimensions of the rod are characterized by its radius, *a*, and its length, *l*. Initial binding occurs even with vanishingly small adhesion strength.[31,37] Starting with small ω, the first bound state is shallow wrapping, in which the rod lies parallel and the membrane slightly deforms around it. When the membrane tension $\tau = 0$ the transition from shallowly wrapped to deeply wrapped requires the rod to tilt normal to the membrane so that one end of the rod is wrapped. This occurs when $\omega a^2/\kappa \geq 2$.[31,56] This transition is tension dependent and will shift to higher ω with increased τ .[13,31] To completely wrap the rod, the condition $\frac{\omega a^2}{\kappa}\left(\frac{2a+l}{8a+l}\right) \geq \frac{1}{2}$ must be satisfied. In this configuration the nanorod is oriented perpendicular with respect to the membrane with no exposed surface.[31] The neck that is formed where the membrane has closed in around the rod is a minimal surface called a catenoid which does not contribute to the membrane deformation energy.[13] Prior work assumed a perfectly straight, rigid rod, whereas in the experiment the rods can bend. Transitions between these configurations are predicted to be discontinuous in the binding energy.[31]

Once a membrane is deformed by a bound particle, bending elasticity mediates interactions among two or more bound particles. If these interactions are attractive, then they can lead to particle aggregates, which could have an amplified effect on the membrane shape (as shown, for example in simulations.[97] The structures that we observed in optical and cryo electron microscopy clearly point to strong rod-rod attractions, which we discuss below.

These particle-scale wrapping transitions are consistent with our experimental findings and can explain the existence of and transition between the major membrane morphology regimes in

our state space. In brief, we propose that DXX and DAX correspond to the shallow-wrapped state, that DAR corresponds to the deeply wrapped state, and that DAX corresponds to the fully wrapped state. We organize our discussion into weak, intermediate, and strong binding.

Subsection 4.1: Weak Binding, DXX and DAX

First, we consider the case of weak binding at low x (Fig. 4.16a). When the adhesion of the particles to the membrane is too weak to wrap the high curvature ends of the rod, theory predicts rods to be shallowly wrapped in equilibrium.[31] The two states associated with the lowest binding energy are DXX and DAX which are present for membranes with less than 10 mol% DOTAP. In the regime of DXX, shallow wrapping deforms the membrane and apparently causes tubules, elongated structures, and textured surfaces. Tubules and elongated shapes are plausibly due to cylindrical curvature induced on the membranes surface by the nanorods. The onset of adhesion in DAX is readily explained by a rod binding to one membrane, leaving one side exposed and able to bind to a second membrane, thus forming an adhesive bridge between the two membranes, and thereby leading to a macroscopic gel. A similar result was found using spherical particles with weak binding.[72] DAX tends to form with higher c_{rod}, suggesting that the vesicle-vesicle adhesion energy depends on c_{rod}, which agrees with a published statistical mechanical model of particle-based adhesion between surfaces.[120] We see indistinguishable behavior for the equiosmolar and floppy vesicles in this regime. Tubules exist also in the DXR domain but only for small rod concentrations. The dependence on low particle concentration suggests that tubule formation is a process that can be interrupted or frustrated by the jamming of particles or by increased membrane tension due to particle binding and area consumption or due to vesicle-vesicle adhesion. Further discussion on the formation of tubules is continued below when comparing to tubules formed in the DXR domain.

Subsection 4.2: Intermediate Binding, DAR

At intermediate adhesion energy ω, our observed transition to DAR (the onset of destruction) is attributed to the transition from shallow to deep wrapping at the individual particle scale (Fig. 4.16b). This configuration leaves a portion of the rod exposed, thus allowing it to form an adhesive bridge between vesicles resulting in a bulk vesicle gel. Unlike the shallow wrapping, however, deeply wrapped rods drastically deform the membrane and consume a substantial amount of projected surface area. This area consumption increases membrane tension resulting, in the runaway destruction of vesicles. Our key experimental observation that supports the deep-wrapping hypothesis is the sharp transition in parameter space between samples with no rupture and samples with rupture, which is consistent with the predicted sharp transition from loose to deep wrap.[13,31]

Subsection 4.3: Strong Binding, DXR

Lastly, we consider the transition to rupturing without adhesion (DXR) at highest adhesion ω. We hypothesize that this regime corresponds to complete wrapping of the rods (Fig. 4.16c). When a rod is completely enveloped by the membrane there is no exposed rod available to form an adhesive bridge, thus turning off vesicle-vesicle adhesion. The hypothesis of complete wrapping is further supported by several experimental observations. First, the transition from DAR to DXR is sharp, as is predicted for the single rod deep-to-complete wrap transition.[31] Second, DXR occurred at the maximum x for each c_{rod}, corresponding to the limit of strongest ω. Third, adding excess area to the vesicles (by exposing them to hyperosmotic conditions) favored DXR over DAR (at x, c_{rod} = 10%, 1.5 nM and at 30%, 10 nM). We hypothesize that adding excess area made it easier for the membrane to completely wrap the rods that bound, leading directly to rupture

without adhesion. Finally, a higher c_{rod} suppressed DXR and favors DAR, which indicates that a high concentration of bound rods suppressed complete wrapping, either because the rods take up a large amount of membrane and significantly raise the membrane tension or because steric hindrance among the bound rods prevents their being fully wrapped.

Subsection 4.4: Membrane-mediated interactions among rods

The dark mobile aggregates observed in the DAR and DXR regimes, can also be explained by the deep-to-complete wrapping transition. The dark mobile aggregates are nanorod-enriched spots (Fig. 4.4). Since the nanorods repel one another in suspension (by the electrostatic double-layer interaction), the aggregation is induced by membrane deformation. Previous simulations has shown that the membrane induces attractive interactions between nanorods and rod like structures bound to membrane.[55] Previous experiments with rod shaped proteins, DNA structures and viruses have demonstrated similar attractive interactions for bound particles,[55,121,122,123] as well as the formation of linear aggregates[124] and tubules.[1,111,125,126,127,128,129] The large mobile spots are similar in some respects to the dark mobile aggregates in so much that they imply some form of attractive interaction between the rods mediated by the membrane.

As in the DXX regime, tubules form at low rod concentrations. Tubules in the DXR domain are typically directed outward and are 1-2 μm in diameter and 2-10 μm in length. They may form due to cylindrical curvature induced on the membrane by the binding of the rods. The tubules formed in the DXR regime are typically smaller than those seen in DXX, and the DXX domain has both inward and outward-pointing tubules. Previous findings showed that nanoparticles130 or proteins[109] that bind on the exterior leaflet without wrapping, as in DXX, can drive tubules extending outward from the vesicles. This growth is driven by a lateral pressure arising from steric interactions among the particles or proteins, leading to a dilation of the outer leaflet that then forms

the convex (outer) surface of the tubule.[71,130] What is peculiar about tubules formed in the DXX domain is the presence of both interior and exterior of vesicles.

The cryo-TEM images (Fig. 4.13) show striking organization of the bound nanorods in the case of strong ω and high c_{rod} (x=100 mol% and c_{rod} = 75 nM). We found clear in-plane parallel ordering of the nanorods as well as aster like configurations. We found a comparable number of rods in each of those two configurations. The parallel rods had a mean surface-to-surface spacing of 6.7 ± 0.2 nm, the position of a minimum in the membrane-mediated interaction between rods. While the evidence for rod-rod attraction is very striking, we note that this result appears to provide clarity to conflict in prior theoretical work. For the case of infinitely long and rigid rods, theory predicts pairwise repulsion between the rods both for weak and strong deformation if they adhere on the same side of the membrane.[131,132] For finite length rods simulation work by Ghosh, *et al*., demonstrated both repulsive and attractive interactions between rods depending on the orientation of the rods with respect to one another.[123] Muller, *et al*. predicted the interaction between rods bound to the membrane to be repulsive for rods on the same side and attractive for rods on opposite leaflets.[133] The majority of these theories, however, do not account for the ends of the rods, nor for flexibility of the rods, nor do they consider the interactions among more than two rods. The earlier work, moreover, treated the rods as infinitely stiff and infinitely long, so they did not consider the membrane deformation at the rod ends. The earlier theory also only considered the case of two rods, whereas it is known that membrane-mediated interactions can be non-pairwise-additive, so that two might repel while several attract.[134] This is wholly inconsistent with our results as we observed the parallel alignment of pairs of rods in regions of low rod density.

The aster-like regions seen in the cryo-TEM were composed of rods that were shorter than the full length. From cryo-TEM, the average measured rod length in the bulk phase was around

341 ± 50 nm, which roughly matches the designed length of the rods. Similarly, the mean length in the parallel arrays was 391 ± 25 nm. However, rods in the asters were about half that length averaging 203 ± 25 nm (Fig. 4.16). Knowing the nature and structure of DNA origami nanorods it is highly improbable that short rods would form originally (and they were not found in the cryo-TEM images without membranes) or that long rods would be able to break cleanly. Therefore, we suspect that the rest of the body of the rods in the aster formation are deflected out of plane. These out of plane deformation make ideal locations for potential nucleation sites of tubules or protrusions on the membrane. We attribute the short, outward-forming objects seen during the destruction process and in the final aggregate structures, (Fig. 4.6), to these aster-like protrusions. The finite bending elasticity of the rods may allow for aster formation. Though the inclusion of rod flexibility may increase the complexity of simulation studies, however, accounting for this is more accurate to biological systems as well as many synthetic particles and is essential for fully describing the final binding structure.

Subsection 4.5: Dynamics of the destruction process

Single vesicle destruction events were observed for vesicles in the DAR and DXR domains. During this process vesicles experienced a sudden drop in radius followed by the steady shrinking of the vesicle until its final rupture. The time before the drop was dependent on c_{rod}, this period of time ranged from seconds for high particle concentrations to tens of minutes for low particle concentration (more particles resulted in a faster response). The dependence on c_{rod} implies that the trigger for the drop is a many-particle behavior requiring some minimum surface coverage. Vesicles within a single field of view do not all jump down in radius simultaneously upon introduction of the nanorods. The sudden drop in size of individual vesicles happened stochastically indicative of a particle nucleation process occurring on the membrane.

Following the sudden drop of radius, the rate of area contraction was found to be dependent on, x and c_{rod}. The duration of the delay time prior to the jump and the duration of the vesicle shrinkage process were comparable for high particle concentrations. However, for low particle concentration the process of shrinking was much faster than the delay time prior to the jump. For higher c_{rod}, the rate of shrinking increased universally for all DOTAP fractions measured. This dependence on c_{rod} makes sense if the projected area contraction is driven by the consumption of area by the binding of rods. The concentration of rods in the bulk is proportional to the flux of rods on the membrane as more rods bind to and are enveloped by the membrane the area contracts until the membrane can no longer support the area contraction and solute exchange causing its final rupture. The dependence on, x, however, was found to be nonmonotonic with the fastest shrinkage rates being found at 60 mol % DOTAP across all rod concentrations. This is quite surprising as it would imply there is some other effect driving the shrinkage rate beyond particle flux and envelopment. What this additional effect is remains unknown, however, it may depend on how the nanorods organize on the membrane as certain membrane-mediated interactions would be dependent on the adhesion strength and thus x. For example, it might be that the shrinkage rate increases with x at low x, and the trend is reversed at high x because of rods jamming on the membrane.

As particles bind and are wrapped by the membrane, the projected surface area of the membrane shrinks because of the envelopment of each bound nanoparticle. If each nanoparticle-wrapping event reduces the projected membrane surface area by an amount equal to the surface area of the nanoparticle, $(2\pi al+4\pi a^2)$, a steady area-reduction rate of 0.3 μm^2/sec on a 3000 μm^2 membrane corresponds to a flux of roughly 130 particles per μm^2 per second binding to the membrane, for c_{rod}= 50 nM. This estimate is found by solving for the particle flux as $\phi DV_{rod}/R$,

where D is the nanoparticle diffusion constant, R is the vesicle radius, V_{rod} is the volume of the rod and ϕ is the volume fraction of nanoparticles. This expression can be rewritten as, $(2\phi k_B TR)/(3\pi\eta a^2)$, if we substitute in the volume of the rod as well as the diffusion constant. For this approximation we used the diffusion constant for a spherical particle which will provide an upper limit on the flux in the absence of long-rage attraction. These estimates are in good agreement with the rates 0.36 ± 0.02 for 30 mol % DOTAP and 0.3 ± 0.1 for 100 mol % DOTAP (both at c_{rod}= 50 nM). However, this does not explain the fastest shrinkage rate observed 2.4 ± 0.7 μm^2/sec for vesicles at 60 mol% DOTAP (c_{rod}= 50 nM). Some additional factor that is dependent on DOTAP concentration is clearly at work in the 60 mol % case. This model of diffusion limited binding does provide a good baseline explanation of why the area reduction rate depends on the local nanoparticle concentration.

Another notable feature of the vesicle destruction process is the rapid exchange of solute across the membrane required to accommodate the interior volume contraction of the membrane. This is particularly striking during the sudden drop in radius where as much as 10% of the vesicles volume is exchanged in less than 500 ms. Additionally, the interior of the vesicles contains sugar which if unable to permeate through the membrane would further increase tension via osmotic stress. The fact that vesicles can shrink down to a fraction of their original size over the course of several minutes implies not only increased permeation of water through the membrane but also sugar as well. The nucleation and then subsequent closing of a pore in the membrane could explain the sudden exchange of solute required to reduce the volume. The continued binding of rods to the membrane may also stabilize nanopores on the membrane allowing for enhanced solute exchange,[71] though the pores would have to be smaller than the resolution limit of our microscopy,

unlike the case of spheres (Ch. 3). Eventually the contraction of the membrane is to great or the exchange of solute is restricted and the vesicles ruptures unfurling into a mass of lipid and nanorod.

Section 5: Conclusion

In our experiments we carefully tuned the interactions between lipid bilayer membranes and DNA origami nanorods to understand how nanoparticle adhesion can be used to remodel membranes. Controlling particle shape, membrane tension, particle concentration and binding strength allowed us to deform the membrane in a variety of unique, repeatable and characterizable ways. The ability to control membrane remodeling in this way may lead to the design of novel membrane-based materials.

These results span a large parameter space and show a consistent and coherent picture of particle membrane interactions. Our results show that for osmotically controlled, low tension membranes, deformation is driven by particle adhesion energy per area, which competes with membrane bending stiffness. Effective membrane tension or available membrane area also effects membrane remodeling. Additionally, we found that nanoparticle concentration effects the binding configuration of particles to the membrane as well as the resulting membrane morphology likely due to an increase in membrane tension caused by area consumption via enveloped nanorods. These results are highly repeatable and show a consistent dependency on tension, adhesion strength and particle concentration over a wide parameter space. This work provides concreate restrictions on what types of morphologies should be observed relative to each other in the phase space and is ideal for comparison in future simulation studies.

This system has demonstrated four distinct membrane morphological behaviors DXX, DAX, DAR and DXR. Each regime has unique features which distinguish it from the others and

have distinct potential for application. The DAX regime results in a long-lived stable vesicle gel which has a high surface area, large volume of more than 99% water and intact closed-cell structure separated by membrane that is impermeable to solutes. The large surface area can be easily functionalized, and the closed-cell structure should allow for the encapsulation of multiple reagents which would only react upon rupture of the gel structure. The DAR domain exhibits gel formation as well as vesicle rupture, which could be utilized to create, hold, and then release cargo at a rate determined by particle concentration. The DXR domain also exhibits vesicle rupture without the gel formation. Such a mechanism could be used for the controlled triggerable release of cargo from within the vesicle. The cross over between these various responses is controlled by adhesion strength, particle concentration and membrane tension. This system has the potential for application in a myriad of contexts where in encapsulation, delivery, and triggered release are desired on the micron scale.

We end with a comparison of the present results to prior studies of particles with different shapes. With spherical nanoparticles, a recent report by some of us showed a sharp cross-over from adhesion to destruction with increasing electrostatic adhesion strength ω. Weakly-bound nanospheres caused formation of a vesicle gel, while strongly bound nanospheres resulted in the destruction of the vesicles in a process that included a shrinking of the vesicles size, the formation of dark mobile aggregates, tubules, pores and lastly vesicle rupture. In the terms of this chapter, spheres showed a transition from DAX to DXR (rupture without adhesion). Similar to the rod case, this transition corresponded to a transition from weak deformation to complete wrapping at the scale of individual particles when $\omega a^2/\kappa$ is of order 1. The presence of discontinuous transitions in the binding energy between individual wrapping configuration of nanoparticles has been observed previously in both theoretical and simulation work looking at the binding of spherical

and non-spherical nanoparticles to low tension lipid bilayer membranes.[13,31,72,105] Rods have two transitions whereas spheres only have one. This key distinction leads to a big difference in the ensemble measurements of the two systems and the appearance of a new state (DAR) in the parameter space for the rods. It is difficult to compare the numerical values for the threshold binding energies for the spheres[13,72] and rods.[31] However, given that the radius of our DNA origami nanorods is quite similar to the radius of the Au-TTMA nanoparticles used previously, we anticipate a similar membrane charge density at the onset of DXR, which is indeed the case (4 mol% DOPS for the Au-TTMA spheres).

Comparisons can also be drawn in the morphologies observed. The presence of tubules is shared with a diversity of experimental systems of a variety of types of particles, spherical[72], proteins[1,126], DNA origami rods[111,127] and more.[125,128,129] It is worth noting that rods give rise to inward and outward pointing tubules, with the outward ones being the most prevalent, in contrast to spheres. What is remarkably striking is the similarity in how vesicles are destroyed between spheres and rods. Both processes exhibit shrinking, tubule formation and dark mobile aggregates.[72] One important feature that is revealed via our Cryo-TEM results is how rods arrange and aggregate on the membrane in parallel aligned rafts and bundled aster-like features. This not only demonstrates attractive interactions mediated by the membrane but is also suggestive of how some of the macroscopic morphologies are formed. In a paper by Mellor *et al* they report the formation of micro-spikes which are short cylindrical filopodia formed by the insertion of a core of 10-30 rod like actin filaments packed tightly together.[1] We can extend this mechanism to the small dark mobile aggregates which confocal microscopy confirms protruded slight from the membrane. We conclude that the aster arrangement of rods on the membrane likely form the small dark mobile aggregates via their out of plane deformation. These deformation and other membrane remodeling

events demonstrate a clear ability to control the morphology of the membrane. The ability to control the interactions between membranes and particles allows us to isolate which effects are governed by particle shape, membrane tension, adhesion strength and particle concentration.

CHAPTER 5

SUMMARY AND FUTURE WORK

This final chapter provides a summary of the results presented in this thesis and suggestions for future work. Section one describes the results presented in this thesis as well as suggestions on how this work can be expanded upon. Section two present projects that were initiated during the time of this thesis work, the questions that arose from these projects and potential experiments that could address those questions. The last section provides concluding remarks on the overall significance of the work presented and its potential for application.

Section 1: Overview of results

Subsection 1.1: Overview of spherical particle results

In chapter 3 of this thesis we presented the results of three different well-defined systems of lipid membrane and nanoparticles that allowed us to tune the interaction strength, ω, between the two components.[72] We observed a remarkably rich set of collective morphologies that are controllable via the particle binding energy. Using giant lipid-bilayer vesicles (10–100 μm) with varied amounts of charged lipid we controlled the adhesion of the membrane to oppositely charged nanoparticles. The majority of our studies focused on 6.7 nm-diameter cationic Au-TTMA nanoparticles.[79] We made the vesicles with a mixture of zwitterionic DOPC and anionic DOPS, so that the molar ratio of DOPS could be tuned to set the binding energy per unit area, ω. When the DOPS fraction and ω were small, the nanoparticles caused the vesicles to adhere to one another and form a soft but solid gel. By contrast, when ω exceeded a threshold value, the vesicles were destroyed in a remarkably complex but highly repeatable process that included vesicle shrinkage,

invagination, pore formation, runaway tubule formation, and possibly vesicle inversion. We associated this threshold with a characteristic binding energy that defined the binding configuration of the particle. Weak binding strength resulted in partial wrapping of the particle to the membrane leaving particles exposed and able to form an adhesive bridge between neighboring vesicles. Strong binding resulted in complete envelopment of the particle and destruction of the vesicle. We also carried out experiments with negatively charged silica nanoparticles mixed with vesicles doped with positively charged DOTAP lipid and found similar results. With this silica system, we investigated two slightly different particle sizes and found that the threshold lipid composition was noticeably lower for the larger particles. Computer simulations also showed a transition from partial to complete wrapping of nanoparticles and subsequent membrane rupture when the dimensionless ratio $\omega a^2/\kappa$ exceeded a threshold value of approximately 0.5, significantly lower than the threshold value of 2 predicted for a single particle.[13] The sequence of morphologies leading to destruction was consistent in each case.[72]

These results provide a unified picture for the wide variety of phenomena reported in cells and vesicles, which likely correspond to different regions of a phase space defined chiefly by ω, κ, a, and particle concentration. Future work controlling particle concentration and membrane tension may illuminate more details on how these binding configurations can be induced and propose new processes for tuning and controlling rupture.

Subsection 1.2: Overview of results for DNA origami nanorods

In chapter 4 we reported the results of a well-defined system of lipid membrane and nanorod interactions wherein we tuned the interaction strength, ω, membrane tension, τ, and particle concentration, c_{rod}. We used anionic DNA origami nanorods that are 420 nm long by 5 nm in diameter. We used giant lipid bilayer vesicles (GUVs) ranging from 10 -100 μm in diameter

composed of a combination of a zwitterionic lipid (DOPC) and a cationic lipid (DOTAP). The binding energy, ω, was tuned by varying the amount of the DOTAP in the membrane, x. We found that for low x, and thus low ω, and low c_{rod}, particles deformed the membrane into tubules and other shapes (DXX). For high c_{rod} and low x, we saw vesicle-vesicle adhesion and the formation of a vesicle-based gel (DAX). With higher x we saw a transition into rupture of vesicles simultaneous with vesicle-vesicle adhesion (DAR). At still higher x, we found a second crossover to rupture of individual vesicles without vesicle-vesicle adhesion (DXR). The process of single vesicle destruction was complex, involving the formation of aggregates, tubules, sudden drops in the vesicle's radius, and a shrinking of the size of the vesicle until final rupture. The sequence of events found in single vesicle destruction were highly repeatable and consistent over a large portion of the state space. To probe for the effects of tension, we also prepared vesicles with excess area by exposing them to a hypertonic solution and observed that the excess area shifted the second crossover. Cryo-TEM images provide the first evidence of membrane-mediated interactions among rods, leading to parallel alignment of membrane-bound rods in some regions of the membrane, and aster-like rod formations and a new mode of deformation in other regions. We presented these results in the form of a state diagram and concluded that the two crossovers arise from the two separate wrapping transitions that occur at the single-particle scale. In the case of perfectly rigid rod-shaped nanoparticles, simulation predicts three wrapping configurations: binding, shallowly wrapped, deeply wrapped, and completely wrapped.[31] Based on our experimental results we concluded that DXX and DAR correspond to the shallowly wrapped configuration, DAR with deeply wrapped and DXR with completely wrapped.

Compared to our earlier study of spherical particles, the rods exhibit many of the same behaviors such as inducing the formation of a bulk vesicle gel at low adhesion and causing vesicle

destruction at high adhesion. However, rods have an additional intermediate state wherein vesicle adhesion followed by rupture is observed. Another difference between the two systems is seen in the vesicle destruction dynamics. Though the process of destruction is very similar in the two systems, in the case of spheres we often observed a long-lived micron scale pore that forms and is stabilized by the nanospheres. This phenomenon was never observed with the rods, the key to understanding how, why, and when pores form remains unknown. One possibility may be area shrinkage rate. In our results with spherical particles it was shown that vesicles with faster shrinkage rates formed pores while those with slower shrinkage rates did not. If there is a dependence on shrinkage rate, then further target investigations with rods could potentially produce pores as well. Additionally, from our experiments it is clear that clusters form readily, however, tubules are found only at low particle concentration. The requirement on low particle concentration may hint at a requirement for specific particle aggregation configurations that can be frustrated if the membrane is too crowded. How these features form and how this relates to the packing of particles on the membrane is unclear. Additional experiments exploring Cryo-TEM imaging of vesicles and nanorods at different concentrations and binding strengths may illuminate more.

These results present a remarkably detailed overview of the phase space defined by ω, κ, τ, and c_{rod}. The wide variety of phenomena observed, and their well characterized dependences make this system an ideal comparison for theory and simulation. This work presents intriguing preliminary results on the dynamics of membrane disruption, including the surprising nonmonotonic dependence of the vesicle-shrinkage rate on adhesion strength. A variety of different membrane morphologies were observed including, dark aggregates, large spots, internal tubules, and external tubules. The dark mobile aggregates which confocal microscopy confirms

deform out of the plan of the membrane may be formed by the insertion of bundles of rods into the membrane as is seen in Cryo-TEM images in the asters configuration of rods on the membrane. Future work exploring the dynamics of particle binding could illuminate the dependence on many particle interactions in resulting membrane morphologies.

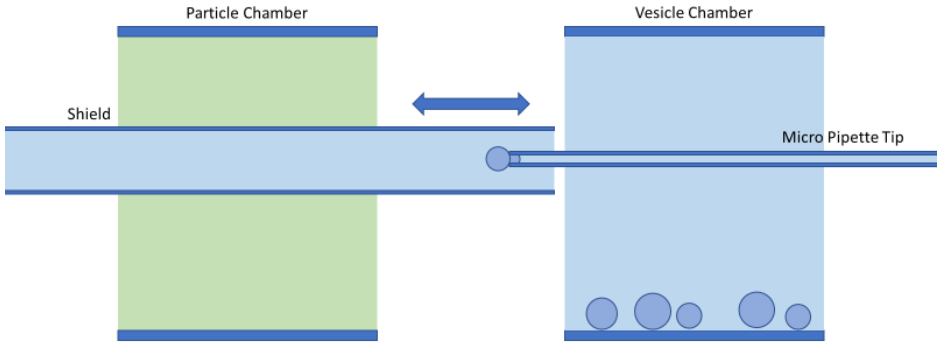

Figure 5.1: Micropipette aspiration chamber

An illustration of the experimental chambers used during micropipette aspiration. The blue chamber on the right side of the image stores the vesicles in an aqueous buffer. The green chamber on the left holds the nanoparticle solution. Vesicles are picked up via suction by the pipette tip. The shield is moved over the vesicle while it is in the vesicle chamber. The shield and tip are then moved across the air gap into the particle chamber and the shield is removed to allow for interactions.

Section 2: Proposed Future Work

During the process of conducting the experiments described in this thesis several other notable projects were initiated but never completed. These projects represent unique and intriguing questions all their own and are presented here as inspiration for future work.

Subsection 2.1: Micropipette Aspiration

Micropipette aspiration is a technique used to measure the mechanical properties of single cells or vesicles. It does so by observing the deformation of such objects under suction pressure.

For a more detailed description of the instrumentation refer to work done by Longo and Ly in a piece published in the Methods of Molecular Biology in 2007.[135] This powerful technique allows us a direct measurement of the mechanical properties of membranes.[136] The question we initially asked, and which remains unanswered is: How do the mechanical properties of vesicles vary as particles bind to the membranes and how does this depend on the binding strength of particles to the membrane.

With the help and training of Arash Manafirad we approached this question by conducted some initial experiments introducing charged vesicles to oppositely charged nanoparticles while under suction by a micropipette tip and measured the response. The experimental system, designed and fabricated by Arash, consisted of two chambers, one with vesicles sedimented to the bottom and the other containing particle solution at the desired concentration, (Fig. 5.1). The vesicles were initially captured via suction by the micro pipette tip. Then a shield containing the same aqueous solution the vesicles were diluted in was drawn around the vesicle. The shield and vesicle were then moved across an air gap to the second chamber which contained the nanoparticle suspension at a defined concentration. The shield was then withdrawn exposing the vesicles to the nanoparticles. The interactions were observed visually with a camera.

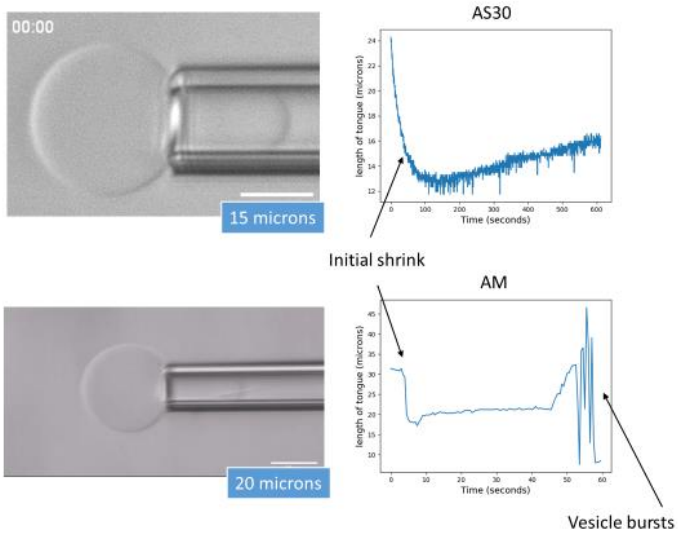

Figure 5.2: Micropipette Aspiration

Two examples of the experimental results found during micropipette aspiration experiments. The top row shows a 100 mol % DOPC vesicle exposed to Ludox AS30 silica nanospheres (50:1 buffer to stock). The response is shown on the right as a trace of the measured tongue length over time. The second row shows a 5 mol% DOTAP and 95 mol% DOPC vesicle interaction with Ludox AM silica nanospheres (100:1 buffer to stock). The response is depicted on the right as a measure of the tongue length over time. Both vesicles experienced an initial decrease in the projected tongue length, the first vesicle then showed a steady growth in the length of the tongue while the second vesicle burst suddenly after about a minute.

We looked at two different species of anionic silica nanoparticles, Ludox AS30 and Ludox AM. The vesicles were composed of zwitterionic DOPC and doped with cationic DOTAP. Preliminary results showed an initial shrinking of the "tongue" length (the portion of the vesicle captured by the pipette tip) followed by a slow increase in the tongue length or rupture in some cases (Fig. 5.2). This response could correspond to an increase in membrane tension, enhanced permeation, and other unknown particle membrane interactions. Work of this nature has yet to be done and would provide a first of its kind measurement of mechanical change in membranes due to particle binding. This experimental system could also be useful for determining permeation effects due to binding which would have direct relevance to the encapsulation and release of cargo carrying vesicle-based materials.

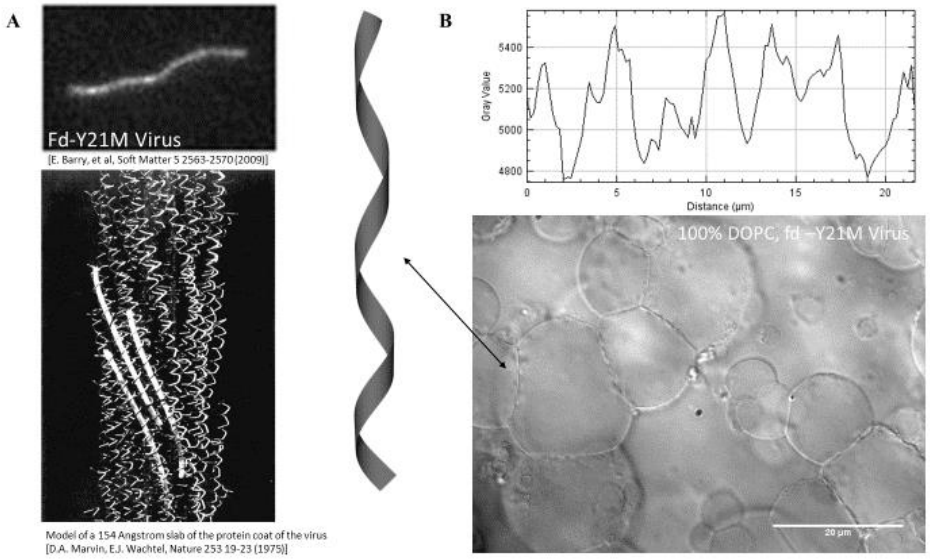

Figure 5.3:fd-Y21M virus

(A) the top image shows fd Y21M viruses imaged with fluorescence microscopy.[137] The bottom image depicts a model of a 154 Angstrom slab of the protein coat of the fd virus.[138] (B) shows optical micrographs (brightfield) of GUVs interacting with fd-Y21M viruses. The rods appear to bind to the membrane and aggregate at the intersections of multiple vesicles in the bulk gel network. At these interfaces, the chiral rods induce a light/dark pattern creating a periodic rippled appearance. The orientation of the rods as they twist with respect to the image plane may be the source of the light/dark patterning.

Subsection 2.2: fd viruses as nanorods

Prior to work with DNA origami nanorods, our initial rod-shaped particle was the fd-Y21M virus, which is a mutant of the filamentous bacteriophage fd wild-type virus. This virus is "rod" like with dimensions of 800 nm by 5nm and a similar stiffness to that of the DNA origami particles outlined in detail in chapters 2 and 4. These viruses were produced in both cationic and anionic varieties by Zhenkun Zhang and Marc Ridilla (Brandeis University) and consist of a single strand of DNA coated with a layer of protein, (Fig. 5.3a).[88,89] These viruses were initially selected because they are monodisperse and readily grown in sufficient quantity. Experiments with these particles were conducted using perfusion chambers in the same way as was done for spherical particles. See chapter 2 for details.

Interactions were tested over a range of charge densities for both the cationic and anionic versions of the virus. For cationic viruses DOPC membranes were doped with the anionic DOPS

(ranging from 0 – 8 mol%). Cationic DOTAP (ranging from 0 – 50 mol%) was used for experiments with anionic particles. We observed vesicle-vesicle adhesion similar to the DAX case for the DNA origami rods (Fig 5.3b). In addition to the formation of a bulk vesicle gel we sometimes observed light-dark patterning at the interfaces between adhered vesicles in the gel for experiments with low adhesion strength (100 mol % DOPC). The fd-Y21M virus has intrinsic twist and we suspect that rods were binding to the surface of the membrane and packing tightly at the interface between adhered vesicles. When chiral rods are packed tightly, they tilt with respect to their neighbors resulting in a large-scale twist like the twist observed in a ribbon. We suspect that the light dark pattern observed at the interfaces between vesicles was caused by the chiral rods packing tightly and twisting along the length of the pattern in a ribbon like fashion. The orientation of the rods as they twist with respect to the image plane may be the source of the light/dark patterning.

These results can be compared to the results with the DNA origami rod shaped particles in chapter 4 where we never saw these light/dark patterns. They also present the question, how does the chirality of bound nanorods effect the deformation of the lipid bilayer membrane. The work could be extended further to look at how the interaction of multiple species of particles allow for controlled membrane deformation. For example, would one observe a membrane mediated depletion effect when nanorods and nanospheres of appropriate size ratios bind to a membrane simultaneously? The optical component of this interaction is particularly intriguing. If one can induce liquid crystalline structures to form on the surface of vesicles, one may be able to tune the color observed in the aqueous suspension. This is particularly intriguing from a food science perspective as the ability control the color of foods is a highly sought-after parameter. Vesicles

formed from food grade lipids combined with nontoxic nanoparticles could be used to manipulate the color of various beverages and potentially other foods.

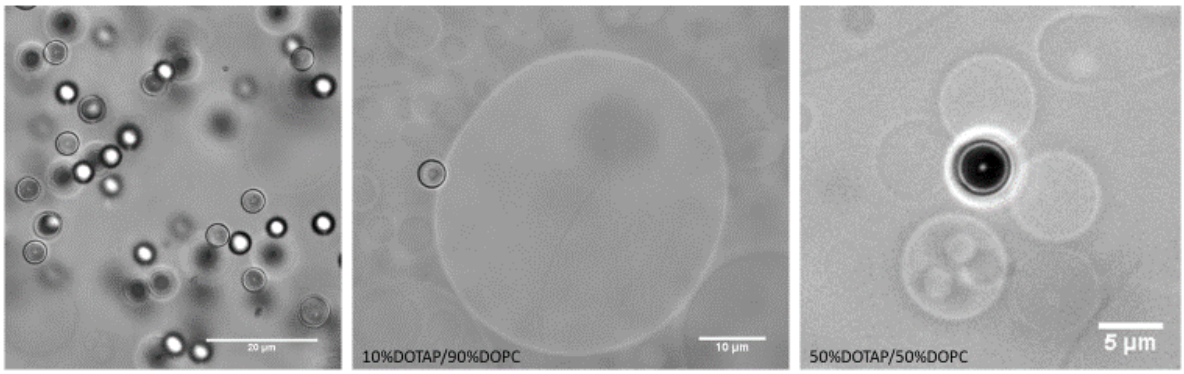

Figure 5.4: Patchy Particles

(Left) Brightfield micrograph of micron sized patchy particles. (Right) Brightfield micrographs of a single micron sized patchy particle lightly bound to the surface of a GUV(s) via one of the charge patches.

Subsection 2.3: Patchy Particles

During our research we were introduced to a new type of Janus micro-particle. These large patchy particles were synthesized by Zhe Gong from the group of Prof Stefano Sacanna (Department of Chemistry, New York University). The particles were 2.5 μm in diameter with a cationic matrix and anionic patches. The bulk of these patchy particles are composed of amidinated polystyrene (PS). The patches of the particles are anionic 3-(Trimethoxysilyl)propyl methacrylate (TPM). The entire surface is coated in triblock copolymer Pluronic F108 to the particles to further stabilize. The particles are then suspended in a 0.5%wt. F108 aqueous solution.

We conducted a few preliminary experiments with these particles to see if the heterogeneous surface functionalization would allow the particles to bind without being fully enveloped. Our experiments followed the same procedure outlined for the spherical particles in chapter 2, using DOPC vesicles doped with the cationic DOTAP to enhance binding. We used a

perfusion chamber, flowed in the patchy particles, and observed the interactions. Indeed, we observed that the particles bound to the membrane but were not fully enveloped (Fig. 5.4). We propose that these large bound particles could be used to track diffusion on the membrane with and without nanoparticles present.[83] They could be used, for example, to see whether the network structure predicted by simulations, in chapter 3, makes the membrane more rigid or more viscous for a much larger tracer particle. This would allow for an indirect measurement of the diffusion of the nanoparticles on the membrane and may provide new insight into the collective dynamics of the many particle system.

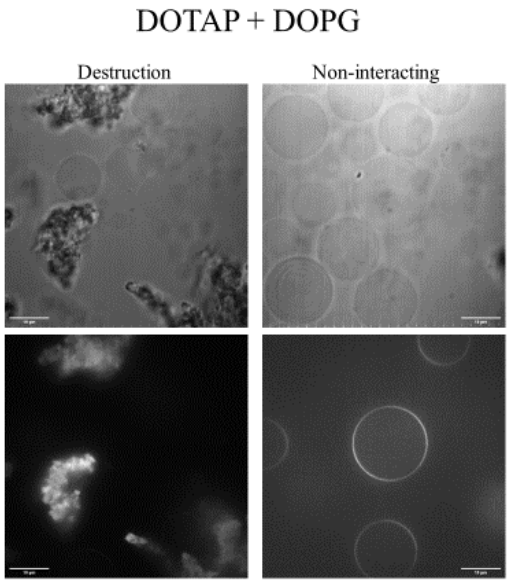

Figure 5.5: Oppositely charged vesicles

The top row shows brightfield micrographs, the bottom row depicts their confocal fluorescence counterparts. The vesicles visible via confocal microscopy are composed of 50% DOTAP / 50% DOPC / >1% rhDOPE. The unlabeled vesicles which are only visible via brightfield microscopy are composed of 50% DOPG / 50% DOPC. The left-hand column shows an example of vesicle destruction due to the interaction of the oppositely charged vesicles. The right-hand column shows oppositely charged vesicles in physical proximity to one another without adhesion or disruption.

Subsection 2.4: Interactions of oppositely charged vesicles

We briefly explored the interactions of vesicles composed of oppositely charged lipids. For these experiments we used vesicles composed of 50/50 DOPC/DOTAP (<1 % rhDOPE) and 50/50

DOPC/DOPG. DOPG is an anionic lipid which should be attracted to the cationic DOTAP. The question we wanted to explore was how will oppositely charged vesicles interact, will they adhere to one another to form a vesicle gel or can we arrange for one vesicle to engulf a smaller one in the manner of phagocytosis. What we found was perplexing. We observed both complete vesicle destruction simultaneous to non-interacting vesicles, (Fig. 5.5). Surprising still the non-interacting vesicles were observed to be in physical contact with their oppositely charged neighbors but not adhering or spreading over one another. Destruction occurred rapidly suggesting perhaps some external mechanical trigger (like the initial flow combining the vesicles) is required to cause interaction and destruction.

This system may still provide a worthwhile investigation. Nanoparticle toxicity is an issue that is still being explored and represents a real hindrance to a technology's adaptation into practical medicine. Being able to induce rupture without the use of nanoparticles is advantageous in this context. More work is needed to determine under what conditions rupture occurs in order to control the process. Subsequent control opens the door to application in encapsulation and release.

Section 3: Conclusion

The work described in this thesis provides new insight into the ways in which nanoparticles interact with lipid bilayer membranes and the parameters that governor that interaction. The first questions we posed was: How do nanospheres interact with and deform lipid bilayer membranes and what are the key parameters that govern that interaction. As is described in detail in chapter 3, we showed that the adhesion strength (of the particles to the membrane) governed the particles binding configuration resulting in either the formation of a bulk vesicle gel or the destruction of

the vesicle. The second question we asked was: How do the multiple regions of curvature for rod shaped particles expand the possible binding configurations of the rod to the membrane and what effect does this have on the bulk interactions in the many particle system. In chapter 4 we described in detail the results that answer this question. We show indeed an increase in the possible binding configurations as well as expanding our understanding of how specific particle binding configurations depend on adhesion strength, particle concentration and vesicle tension. These results present a first of its kind analysis on the key parameters that govern the interaction between lipid vesicles and nanoparticles resulting in a compelling state diagram. We also present the first ever reported direct observation of attractive interaction between nanorods on a lipid bilayer membrane. This is particularly significant as much of the current literature predicted repulsive interactions. The results presented in their totality paint a clear picture of the dependence on particle shape, adhesion strength, particle concentration and membrane tension on the binding of nanoscale particles to lipid bilayer membranes. Controlling these key parameters allowed us to deform the membrane in a variety of unique, repeatable and characterizable ways.

These results show a unified picture that could explain the wide variety of behaviors reported previously with vesicles exposed to nanoparticles, viruses, proteins, or polymers. The robust nature of these results is in part due to the wide parameter space that was explored. This work demonstrates how powerful controlling and tuning core parameters is in illuminating fundamental properties. Additionally, the ability to tune morphology opens the door to the design of smart responsive membrane-based materials. These results could be used to motivate the creation of cargo-carrying vesicle gels that rupture when exposed to external stimuli[11], or for the design of controlled release over extended periods of time. Realizing these applications requires a fundamental understanding of the design principles that govern the deformation and remodeling

of lipid bilayer membranes. This work makes a major contribution to the understand of and implementation of these parameters and provides key insight into intuitive next steps. This could include exploring different particle geometries, exploiting inhomogeneous particle functionalization, mixing particles of different geometries and so much more. Biological systems have shown us how a diversity of proteins and biomolecules can work in tandem to do useful work for cells. So, too we hope to harness that same functionality to inspire the formation of new bio-inspired membrane-based materials.

APPENDIX

VESICLE SIZE TRACKING

Primary Script

File name: findVesicle_Single_Rate.m

```
%% Vesicle finding with Circular Hough Transform
% Sarah Zuraw-Weston
%
% Code uses the |circle_hough| and |circle_houghpeaks| to find
% circular objects in an image.
%
% Uses the Image Processing Toolbox

%% User Inputs
% Figure Title
PlotTitle = '60% DOTAP and 10 nM DNA Rods Vesicle 15';
Trial = 'V15';

% Filename and folder with format "path/filename" + 0000
path =
'C:\Users\sarah\Documents\MATLAB\findVesicle\Data\11_21_2019_DNAorigamiTW_10n
M_Balanced_60DOTAP\60DOTAP_test15\60DOTAP';
pathFigures =
'C:\Users\sarah\Documents\MATLAB\findVesicle\Data\11_21_2019_DNAorigamiTW_10n
M_Balanced_60DOTAP\60DOTAP_test15\';

% Number of frames to be analyzed (counting the first frame as 0)
firstFrame = 1;
lastFrame = 251;
frames = lastFrame - firstFrame;

% frames per second
frameRate = 0.5;
v = zeros(1,frames);

% Note the approximate center of the vesicle
centerx = 91;
centery = 95;

% Note frame where the vesicle has a sudden decrease in radius
% If no jump set to zero
jump = 0;

% Note the approx. min and max radius of the vesicle before sudden jump
% Before jump
% if no jump use  rminStart and rmaxStart
rminStart = 10;
```

```
rmaxStart = 40;

% After jump
rminEnd = 20;
rmaxEnd = 30;




%% Setup
% Loop over all the frames
c = firstFrame;
k =0;

for i = 0:(frames-1)
      tic;

      d = num2str(c);

      if c<10
            filename = [path,'000', d];
      end

      if 9<c && c<100
            filename = [path,'00', d];
      end

      if 99<c && c<1000
            filename = [path,'0', d];
      end

      if 999<c && c<10000
            filename = [path,'', d];
      end

      % Reads an image, gets its edges
      im = imread(filename,'tiff');

      % Display original image
      %figure(1)
      %imshow(im);


      % Create a black and white image of only the edges of the vesicles
      % [e,threshOut] = edge(im, 'canny',[low high],std);
      e = edge(im, 'canny',[0.0000 0.0001],1.5);

      % Remove objects that are less then 50 pixels (stray lines)
      e = bwareaopen(e, 20);

      % Display edge image
      %figure(2)
      %imshow(e);
```

```
%% Carry out the HT
% The circles round the vesicles have radii in a specified pixel range.
% To make sure we cover the range, we search radii in steps of 1 pixel.

if ((c < jump) || (jump == 0))
      radii = rminStart:1:rmaxStart;
else
      radii = rminEnd:1:rmaxEnd;
end

% We run the Hough transform on our edge image over our range of radii
% We select the 'same' option to simplify later processing, and the
% 'normalize' option to avoid a bias towards finding larger circles.

h = circle_hough(e, radii, 'same', 'normalise');


%% Find some peaks in the accumulator
% We use the neighborhood-suppression method of peak finding to ensure
% that we find spatially separated circles.

% peaks = circle_houghpeaks(h, radii ,[minimum threshold],'nhoodxy',
odd int,
% 'nhoodr', odd int);
% minimum(hard min you set, if specified unrelated to h_max)
% threshold(multiplied by h_max)] default [0.4*h_max 0.5*h_max]

peaks = Copy_of_circle_houghpeaks(h, radii, [1.5 0.8],'nhoodxy', 45,
'nhoodr', 35, 'npeaks', 8);


%% Look at the results
% We draw the circles found on the image, using both the positions and
the
% radii stored in the |peaks| array. The |circlepoints| function is
% convenient for this - it is also used by |circle_hough| so comes with
it.
% tally and display result of fits

x = 1:max(radii);
f = false(1,max(radii));
f(peaks(3,:)) = 1;
x = x(f);
z = zeros(length(x),2);
ind = 1;
for y = x
      z(ind,2) = sum(peaks(3,:)==y);
      ind = ind+1;
end

% Select circle with center closest to the center of image

dist =  zeros(length(peaks(1,:)),1);
```

```
for j = 1:length(peaks(1,:))
      dist(j)=sqrt((centerx-peaks(1,j))^2 + (centery-peaks(2,j))^2);
end

[val,idx] = min(dist);

% Record the radius of the center most vesicle for this frame
v(k+1) = peaks(3,idx);


% If difference in radius is still greater than 10 pixels from the
previous
%vesicle assign the current vesicle the average radius of the previous
ten

if k>10 && ((v(k+1)>(v(k)+10)) || (v(k+1)<(v(k)-10))) && (c ~= jump)
      %assign radius to be the average of the last 10 radius measured
      ave = 0;
      for m = 1:10
            ave = ave + v(k-m);
      end
      ave = ave/10;
      v(k+1) = ave;

      disp('Reassigned Vesicle Radius to the average of last 10
      vesicles'),
      disp('   ----------'),
      disp(v(k+1));
end

% Overlay edge on original image
figure(3)
imshow(im);
hold on;

% Draw All circles
for peak = peaks
      [x, y] = circlepoints(peak(3));
      plot(x+peak(1), y+peak(2), 'r-');
end
scatter(peaks(1,:),peaks(2,:),'.b')

% Draw circle with center closest to the center of image
[x, y] = circlepoints(peaks(3,idx));
plot(x+peaks(1,idx), y+peaks(2,idx), 'g-');
scatter(peaks(1,idx),peaks(2,idx),'.b')

hold off

% Save circle images
folder = [ pathFigures 'CirclesDrawn\'];
figureName = [d,'.jpg'];
saveas(figure(3),[folder figureName]);
```

```
        disp('Iteration'),
        disp('   ----------')
        disp(k+1);

        %advancing each frame
        c = c+1;
        %counter that advances vector, v, storing the #vesicles in each frame
        k = k+1;

        toc;
end


% Make Figures
n = 0:(frames-1);
m = (n*frameRate)/60;



if (jump~=0)
    %Plot frames vs radius
    figure(4)
    hold on
    plot(n,v)

    %divide data between before and after jump
    j = jump - firstFrame;
    nbefore = n(1:j);
    nafter = n((j+1):end);
    vbefore = v(1:j);
    vafter = v((j+1):end);

    %Apply linear fit before jump and save as .txt
    fit1ml = fitlm(nbefore,vbefore);
    disp('Before Jump ----------');
    disp(fit1ml);
    f1 = evalc('disp(fit1ml)');
    fileID = fopen([pathFigures 'fitBefore.txt'],'w');
    fprintf(fileID,f1);
    fclose(fileID);
    fit1_est = nbefore.*(fit1ml.Coefficients.Estimate(2))+
(fit1ml.Coefficients.Estimate(1));
    plot(nbefore,fit1_est,'r--','LineWidth', 2);

    %Apply linear fit after jump and save as .txt
    fit2ml = fitlm(nafter,vafter);
    disp('After Jump ----------');
    disp(fit2ml);
    f2 = evalc('disp(fit2ml)');
    fileID = fopen([pathFigures 'fitAfter.txt'],'w');
    fprintf(fileID,f2);
    fclose(fileID);
    fit2_est = nafter.*(fit2ml.Coefficients.Estimate(2))+
(fit2ml.Coefficients.Estimate(1));
    plot(nafter,fit2_est,'g--','LineWidth', 2);
```

```
    %Plot fits on data and save as .fig
    title(PlotTitle)
    xlabel('Time (frames)')
    ylabel('Vesicles Radius (pixels)');
    legend('Vesicle Radius',['Fit 1 y ='
num2str(round(fit1ml.Coefficients.Estimate(2),3)) '*x +'
num2str(round(fit1ml.Coefficients.Estimate(1),3))],['Fit 2 y ='
num2str(round(fit2ml.Coefficients.Estimate(2),3)) '*x +'
num2str(round(fit2ml.Coefficients.Estimate(1),3))]);

    hold off
    savefig([pathFigures Trial '.fig']);

else
    %Plot frames vs radius
    figure(4)
    hold on
    plot(n,v)

    %Apply linear fit save as .txt
    fit1ml = fitlm(n,v);
    disp('Fit ----------');
    disp(fit1ml);
    f1 = evalc('disp(fit1ml)');
    fileID = fopen([pathFigures 'fit.txt'],'w');
    fprintf(fileID,f1);
    fclose(fileID);
    fit1_est = n.*(fit1ml.Coefficients.Estimate(2))+
(fit1ml.Coefficients.Estimate(1));
    plot(n,fit1_est,'r--','LineWidth', 2);

    %Plot fits on data and save as .fig
    title(PlotTitle)
    xlabel('Time (frames)')
    ylabel('Vesicles Radius (pixels)');
    legend('Vesicle Radius',['Fit 1 y ='
num2str(round(fit1ml.Coefficients.Estimate(2),3)) '*x +'
num2str(round(fit1ml.Coefficients.Estimate(1),3))]);

    hold off
    savefig([pathFigures Trial '.fig']);

end
```

Circle Function

File name: circle_hough.m

```
function [h, margin] = circle_hough(b, rrange, varargin)
%CIRCLE_HOUGH Hough transform for circles
%   [H, MARGIN] = CIRCLE_HOUGH(B, RADII) takes a binary 2-D image B and a
%   vector RADII giving the radii of circles to detect. It returns the 3-D
%   accumulator array H, and an integer MARGIN such that H(I,J,K) contains
%   the number of votes for the circle centred at B(I-MARGIN, J-MARGIN),
%   with radius RADII(K). Circles which pass through B but whose centres
%   are outside B receive votes.
%
%   [H, MARGIN] = CIRCLE_HOUGH(B, RADII, opt1, ...) allows options to be
%   set. Each option is a string, which if included has the following
%   effect:
%
%   'same' returns only the part of H corresponding to centre positions
%   within the image. In this case H(:,:,k) has the same dimensions as B,
%   and MARGIN is 0. This option should not be used if circles whose
%   centres are outside the image are to be detected.
%
%   'normalise' multiplies each slice of H, H(:,:,K), by 1/RADII(K). This
%   may be useful because larger circles get more votes, roughly in
%   proportion to their radius.
%
%   The spatial resolution of the accumulator is the same as the spatial
%   resolution of the original image. Smoothing the accumulator array
%   allows the effective resolution to be controlled, and this is probably
%   essential for sensitivity to circles of arbitrary radius if the spacing
%   between radii is greater than 1. If time or memory requirements are a
%   problem, a generalisation of this function to allow larger bins to be
%   used from the start would be worthwhile.
%
%   Each feature in B is allowed 1 vote for each circle. This function
%   could easily be generalised to allow weighted features.
%
%   See also CIRCLEPOINTS, CIRCLE_HOUGHPEAKS, CIRCLE_HOUGHDEMO

% Copyright David Young 2008, 2010

% % argument checking
% opts = {'same' 'normalise'};
% narginchk(2, 2+length(opts));
% validateattributes(rrange, {'double'}, {'real' 'positive' 'vector'});
% if ~all(ismember(varargin, opts))
%     error('Unrecognised option');
% end

% get indices of non-zero features of b
[featR, featC] = find(b);

% set up accumulator array - with a margin to avoid need for bounds checking
[nr, nc] = size(b);
nradii = length(rrange);
```

```
margin = ceil(max(rrange));
nrh = nr + 2*margin;        % increase size of accumulator
nch = nc + 2*margin;
h = zeros(nrh*nch*nradii, 1, 'uint32');  % 1-D for now, uint32 a touch faster

% get templates for circles at all radii - these specify accumulator
% elements to increment relative to a given feature
tempR = []; tempC = []; tempRad = [];
for i = 1:nradii
    [tR, tC] = circlepoints(rrange(i));
    tempR = [tempR tR]; %#ok<*AGROW>
    tempC = [tempC tC];
    tempRad = [tempRad repmat(i, 1, length(tR))];
end

% Convert offsets into linear indices into h - this is similar to sub2ind.
% Take care to avoid negative elements in either of these so can use
% uint32, which speeds up processing by a factor of more than 3 (in version
% 7.5.0.342)!
tempInd = uint32( tempR+margin + nrh*(tempC+margin) + nrh*nch*(tempRad-1) );
featInd = uint32( featR' + nrh*(featC-1)' );

% Loop over features
for f = featInd
    % shift template to be centred on this feature
    incI = tempInd + f;
    % and update the accumulator
    h(incI) = h(incI) + 1;
end

% Reshape h, convert to double, and apply options
h = reshape(double(h), nrh, nch, nradii);

if ismember('same', varargin)
    h = h(1+margin:end-margin, 1+margin:end-margin, :);
    margin = 0;
end

if ismember('normalise', varargin)
    h = bsxfun(@rdivide, h, reshape(rrange, 1, 1, length(rrange)));
end

end
```

Peak Function

File name: circle_houghpeaks.m

```
function peaks = circle_houghpeaks(h, radii, varargin)
%CIRCLE_HOUGHPEAKS finds peaks in the output of CIRCLE_HOUGH
%   PEAKS = CIRCLE_HOUGHPEAKS(H, RADII, MARGIN, OPTIONS) locates the
%   positions of peaks in the output of CIRCLE_HOUGH. The result PEAKS is a
%   3 x N array, where each column gives the position and radius of a
%   possible circle in the original array. The first row of PEAKS has the
%   x-coordinates, the second row has the y-coordinates, and the third row
%   has the radii.
%
%   H is the 3D accumulator array returned by CIRCLE_HOUGH.
%
%   RADII is the array of radii which was passed as an argument to
%   CIRCLE_HOUGH.
%
%   MARGIN is optional, and may be omitted if the 'same' option was used
%   with CIRCLE_HOUGH. Otherwise, it should be the second result returned
%   by CIRCLE_HOUGH.
%
%   OPTIONS is a comma-separated list of parameter/value pairs, with the
%   following effects:
%
%   'Smoothxy' causes each x-y layer of H to be smoothed before peak
%   detection using a 2D Gaussian kernel whose "sigma" parameter is given
%   by the value of this argument.
%
%   'Smoothr' causes each radius column of H to be smoothed before peak
%   detection using a 1D Gaussian kernel whose "sigma" parameter is given
%   by the value of this argument.
%
%       Note: Smoothing may be useful to locate peaks in noisy accumulator
%       arrays. However, it may also cause the performance to deteriorate
%       if H contains sharp peaks. It is most likely to be useful if
%       neighbourhood suppression (see below) is not used.
%
%       Both smoothing operations use reflecting boundary conditions to
%       compute values close to the boundaries.
%
%   'Threshold' sets the minimum number of votes (after any smoothing)
%   needed for a peak to be counted. The default is 0.5 * the maximum value
%   in H.
%
%   'Npeaks' sets the maximum number of peaks to be found. The highest
%   NPEAKS peaks are returned, unless the threshold causes fewer than
%   NPEAKS peaks to be available.
%
%   'Nhoodxy' must be followed by an odd integer, which sets a minimum
%   spatial separation between peaks. See below for a more precise
%   statement. The default is 1.
%
%   'Nhoodr' must be followed by an odd integer, which sets a minimum
%   separation in radius between peaks. See below for a more precise
```

```
%   statement. The default is 1.
%
%       When a peak has been found, no other peak with a position within an
%       NHOODXY x NHOODXY x NHOODR box centred on the first peak will be
%       detected. Peaks are found sequentially; for example, after the
%       highest peak has been found, the second will be found at the
%       largest value in H excepting the exclusion box found the first
%       peak. This is similar to the mechanism provided by the Toolbox
%       function HOUGHPEAKS.
%
%       If both the 'Nhoodxy' and 'Nhoodr' options are omitted, the effect
%       is not quite the same as setting each of them to 1. Instead of a
%       sequential algorithm with repeated passes over H, the Toolbox
%       function IMREGIONALMAX is used. This may produce slightly different
%       results, since an above-threshold point adjacent to a peak will
%       appear as an independent peak using the sequential suppression
%       algorithm, but will not be a local maximum.
%
%   See also CIRCLE_HOUGH, CIRCLE_HOUGHDEMO

% check arguments
params = checkargs(h, radii, varargin{:});

% smooth the accumulator - xy
if params.smoothxy > 0
    [m, hsize] = gaussmask1d(params.smoothxy);
    % smooth each dimension separately, with reflection
    h = cat(1, h(hsize:-1:1,:,:), h, h(end:-1:end-hsize+1,:,:));
    h = convn(h, reshape(m, length(m), 1, 1), 'valid');

    h = cat(2, h(:,hsize:-1:1,:), h, h(:,end:-1:end-hsize+1,:));
    h = convn(h, reshape(m, 1, length(m), 1), 'valid');
end

% smooth the accumulator - r
if params.smoothr > 0
    [m, hsize] = gaussmask1d(params.smoothr);
    h = cat(3, h(:,:,hsize:-1:1), h, h(:,:,end:-1:end-hsize+1));
    h = convn(h, reshape(m, 1, 1, length(m)), 'valid');
end

% set threshold

 if isempty(params.threshold)
        params.threshold = 0.5 * max(h(:));
 end

if isempty(params.nhoodxy) && isempty(params.nhoodr)
    % First approach to peak finding: local maxima

    % find the maxima
    maxarr = imregionalmax(h);

    maxarr = maxarr & h >= params.threshold;
```

```
    % get array indices
    peakind = find(maxarr);
    [y, x, rind] = ind2sub(size(h), peakind);
    peaks = [x'; y'; radii(rind)];

    % get strongest peaks
    if ~isempty(params.npeaks) && params.npeaks < size(peaks,2)
        [~, ind] = sort(h(peakind), 'descend');
        ind = ind(1:params.npeaks);
        peaks = peaks(:, ind);
    end

else
    % Second approach: iterative global max with suppression
    if isempty(params.nhoodxy)
        params.nhoodxy = 1;
    elseif isempty(params.nhoodr)
        params.nhoodr = 1;
    end
    nhood2 = ([params.nhoodxy params.nhoodxy params.nhoodr]-1) / 2;

    if isempty(params.npeaks)
        maxpks = 0;
        peaks = zeros(3, round(numel(h)/100));  % preallocate
    else
        maxpks = params.npeaks;
        peaks = zeros(3, maxpks);  % preallocate
    end

    np = 0;
    while true
        [r, c, k, v] = max3(h);
        % stop if peak height below threshold
        if v < params.threshold || v == 0
            break;
        end
        np = np + 1;
        peaks(:, np) = [c; r; radii(k)];
        % stop if done enough peaks
        if np == maxpks
            break;
        end
        % suppress this peak
        r0 = max([1 1 1], [r c k]-nhood2);
        r1 = min(size(h), [r c k]+nhood2);
        h(r0(1):r1(1), r0(2):r1(2), r0(3):r1(3)) = 0;
    end
    peaks(:, np+1:end) = [];   % trim
end

% adjust for margin
if params.margin > 0
    peaks([1 2], :) = peaks([1 2], :) - params.margin;
end
end
```

```
function params = checkargs(h, radii, varargin)
% Argument checking
ip = inputParser;

% required
htest = @(h) validateattributes(h, {'double'}, {'real' 'nonnegative'
'nonsparse'});
ip.addRequired('h', htest);
rtest = @(radii) validateattributes(radii, {'double'}, {'real' 'positive'
'vector'});
ip.addRequired('radii', rtest);

% optional
mtest = @(n) validateattributes(n, {'double'}, {'real' 'nonnegative'
'integer' 'scalar'});
ip.addOptional('margin', 0, mtest);

% parameter/value pairs
stest = @(s) validateattributes(s, {'double'}, {'real' 'nonnegative'
'scalar'});
ip.addParamValue('smoothxy', 0, stest);
ip.addParamValue('smoothr', 0, stest);
ip.addParamValue('threshold', [], stest);
nptest = @(n) validateattributes(n, {'double'}, {'real' 'positive' 'integer'
'scalar'});
ip.addParamValue('npeaks', [], nptest);
nhtest = @(n) validateattributes(n, {'double'}, {'odd' 'positive' 'scalar'});
ip.addParamValue('nhoodxy', [], nhtest);
ip.addParamValue('nhoodr', [], nhtest);
ip.parse(h, radii, varargin{:});
params = ip.Results;
end

function [m, hsize] = gaussmask1d(sigma)
% truncated 1D Gaussian mask
hsize = ceil(2.5*sigma);  % reasonable truncation
x = (-hsize:hsize) / (sqrt(2) * sigma);
m = exp(-x.^2);
m = m / sum(m);  % normalise
end

function [r, c, k, v] = max3(h)
% location and value of global maximum of a 3D array
[vr, r] = max(h);
[vc, c] = max(vr);
[v, k] = max(vc);
c = c(1, 1, k);
r = r(1, c, k);
end
```

Circle points Function

File name: circlepoints.m

```
function [x, y] = circlepoints(r)
%CIRCLEPOINTS  Returns integer points close to a circle
%   [X, Y] = CIRCLEPOINTS(R) where R is a scalar returns coordinates of
%   integer points close to a circle of radius R, such that none is
%   repeated and there are no gaps in the circle (under 8-connectivity).
%
%   If R is a row vector, a circle is generated for each element of R and
%   the points concatenated.

%   Copyright David Young 2010

x = [];
y = [];
for rad = r
    [xp, yp] = circlepoints1(rad);
    x = [x xp];
    y = [y yp];
end

end

function [x, y] = circlepoints1(r)
% Get number of rows needed to cover 1/8 of the circle
l = round(r/sqrt(2));
if round(sqrt(r.^2 - l.^2)) < l   % if crosses diagonal
    l = l-1;
end
% generate coords for 1/8 of the circle, a dot on each row
x0 = 0:l;
y0 = round(sqrt(r.^2 - x0.^2));
% Check for overlap
if y0(end) == l
    l2 = l;
else
    l2 = l+1;
end
% assemble first quadrant
x = [x0 y0(l2:-1:2)];
y = [y0 x0(l2:-1:2)];
% add next quadrant
x0 = [x y];
y0 = [y -x];
% assemble full circle
x = [x0 -x0];
y = [y0 -y0];
end
```

REFERENCES

[1] Mellor, H., (2010) Biochimica et Biophysica Acta (BBA) - Molecular Cell Research **1803**, 191.

[2] Richards, D. M. & Endres, R. G. (2017) "How cells engulf: a review of theoretical approaches to phagocytosis" Rep. Prog. Phys. **80**: 126601.

[3] Johannes, L., Parton, R. G., Bassereau, P. & Mayor, S. (2015) "Endocytosis: Remote Control from Deep Inside" Nature Reviews Molecular Cell Biology **16**: 311-321.

[4] van Meer, G., et al. (2008). "Membrane lipids: where they are and how they behave." Nature Reviews Molecular Cell Biology **9**(2): 112-124.

[5] Zimmerberg, J. and M. M. Kozlov (2006). "How proteins produce cellular membrane curvature." Nature Reviews Molecular Cell Biology **7**(1): 9-19.

[6] Keren, K. (2011) "Cell motility: the integrating role of the plasma membrane" Eur Biophys J. **40** (9): 1031-1027.

[7] Kay, R., Langridge, P., Traynor, D. & Hoeller, O. (2008) "Changing directions in the study of chemotaxis" Nature Reviews Molecular Cell Biology **9**: 455-463.

[8] Svitkina, T. (2018) "The Actin Cytoskeleton and Actin-Based Motility" Cold Spring Harb Perspect Biol **10** (1): a018267.

[9] Alipour, E., Halverson, D., McWhirter, S., Walker, G. (2017) "Phospholipid Bilayers: Stability and Encapsulation of Nanoparticle" Ann Rev Phys Chem **5** (68): 261-283.

[10] Nikoleli, G., Nikolelis, D., Siontorou, C., Nikolelis, M., & Karapetis, S. (2018) "The Application of Lipid Membranes in Biosensing" Membranes MDPI **8** (4): 108.

[11] Paasonen, L., et al. (2007) "Gold Nanoparticles Enable Selective Light-Induced Contents Release from Liposomes" Journal of Controlled Release **122**: 86–93.

[12] Alberts, B. (2002). Molecular biology of the cell. New York, Garland Science.

[13] Deserno, M. (2004). "Elastic deformation of a fluid membrane upon colloid binding." Physical Review E **69**(3).

[14] Le Bihan, O., Bonnafous, P., Marak, L., Bickel, T., Trepout, S., Mornet, S., De Haas, F., Talbot, H., Taveau, J. C. & Lambert, O. (2009) "Cryo-Electron Tomography of Nanoparticle Transmigration into Liposome" Journal Struct. Biol **168**: 419.

[15] Bahrami, A. H., Raatz, M., Agudo-Canalejo, J., Michel, R., Curtis, E. M., Hall, C. K., Gradzielski, M., Lipowsky, R. & Weikl, T. R. (2014) "Wrapping of nanoparticles by membranes" Advances in Colloid and Interface Science **208**: 214-224.

[16] Rossi, G., and Monticelli, L., (2014) "Modeling the effect of nano-sized polymer particles on the properties of lipid membranes" Journal Phys.: Condens. Matter **26**:503101.

[17] Pogodin S., and Baulin, V. A. (2010) "Can a Carbon Nanotube Pierce through a Phospholipid Bilayer?" ACS Nano **4**:5293–300.

[18] Vacha, R., Martinez-Veracoechea, F. J., and Frenkel, D. (2012) "Intracellular Release of Endocytosed Nanoparticles Upon a Change of Ligand–Receptor Interaction" ACS Nano **6**(12):10598–10605.

[19] Tian, F., Zhang, X., & Dong, W. (2014) "How hydrophobic nanoparticles aggregate in the interior of membranes: A computer simulation" Phys. Rev. E **90**:052701.

[20] Reynwar, B. J. and M. Deserno (2011). "Membrane-mediated interactions between circular particles in the strongly curved regime." Soft Matter **7**(18): 8567.

[21] Reddy, A. S., et al. (2012). "Effect of membrane tension on the physical properties of DOPC lipid bilayer membrane." Biochim Biophys Acta **1818**(9): 2271-2281.

[22] Champion, J. A. and S. Mitragotri (2006). "Role of target geometry in phagocytosis." Proc Natl Acad Sci U S A **103**(13): 4930-4934.

[23] Zhang, Y., et al. (2012). "Permission to enter cell by shape: nanodisk vs nanosphere." ACS Appl Mater Interfaces **4**(8): 4099-4105.

[24] Xu, A., et al. (2012). "A physical model for the size-dependent cellular uptake of nanoparticles modified with cationic surfactants." Int J Nanomedicine **7**: 3547-3554.

[25] Wang, B., et al. (2008). "Nanoparticle-induced surface reconstruction of phospholipid membranes." Proc Natl Acad Sci U S A **105**(47): 18171-18175.

[26] Frese, R. N., et al. (2008). "Protein shape and crowding drive domain formation and curvature in biological membranes." Biophys J **94**(2): 640-647.

[27] Spangler, E. J., Upreti, S. & Laradji, M. (2016) "Partial Wrapping and Spontaneous Endocytosis of Spherical Nanoparticles by Tensionless Lipid Membranes" J. Chem. Phys. **144**:044901.

[28] Deserno, M. and W. M. Gelbart (2002). "Adhesion and Wrapping in Colloid−Vesicle Complexes." The Journal of Physical Chemistry B **106**(21): 5543-5552.

[29] Gauthier, N. C., Masters, T. A., Sheetz, M. P. (2012) “Mechanical feedback between membrane tension and dynamics” Trends Cell Biol. **22**:527–535.

[30] Lieber, A. D., Yehudai-Resheff, S., Barnhart, E. L., Theriot, J. A., Keren, K. (2013) “Membrane tension in rapidly moving cells is determined by cytoskeletal forces” Current biology **23**:1409–1417.

[31] Dasgupta, S., Auth, T., and Gompper, G. (2014) “Shape and Orientation Matter for the Cellular Uptake of Nonspherical Particles” Nanoletters **14**(2):687-693.

[32] Smith, A. -S., Sackmann, E. & Seifert, U. (2003) “Effects of a pulling force on the shape of a bound vesicle” Europhys. Lett. **64**:281.

[33] Seifert, U. & Lipowsky, R. (1990) “Adhesion of vesicles” Phys. Rev. A **42**:4768.

[34] Deserno, M. & Bickel, T. (2003) “Wrapping of a Spherical Colloid by a Fluid Membrane” Europhys. Lett. **62**: 767.

[35] Ruiz-Herrero, T., et al. (2012). "Mechanisms of budding of nanoscale particles through lipid bilayers." J Phys Chem B **116**(32): 9595-9603.

[36] Chen, X., et al. (2013). "Internalization pathways of nanoparticles and their interaction with a vesicle." Soft Matter **9**(31): 7592.

[37] Chen, L. P., Xiao, S. Y., Zhu, H., Wang, L. & Liang, H. J. (2016) “Shape dependent internalization kinetics of nanoparticles by membranes” Soft Matter **12**, 2632-2641.

[38] Santhosh, P. B., et al., (2014) “Influence of Nanoparticle-Membrane Electrostatic Interactions on Membrane Fluidity and Bending Elasticity” Chem. Phys. Lipids **178**:52 –62.

[39] van der Wel, C., et al. (2016) “Lipid Membrane-Mediated Attraction between Curvature Inducing Objects” Sci. Rep. **6**:32825.

[40] Dietrich, C., Angelova, M. & Pouligny, B. (1997) “Adhesion of Latex Spheres to Giant Phospholipid Vesicles: Statics and Dynamics” J. Phys. II **7**:1651–1682.

[41] Raatz, M., Lipowsky, R. & Weikl, T. R. (2014) “Cooperative wrapping of nanoparticles by membrane tubes” Soft Matter **20**, 3570-3577.

[42] Helm, C. A., Israelachvili, J. N. & McGuiggan, M. P. (1989) “Molecular mechanisms and forces involved in the adhesion and fusion of amphiphilic bilayers” Science **246**:919–22.

[43] Fošnarič, M., Iglič, A., Kroll, D. M., & May, S. (2009) “Monte Carlo simulations of complex formation between a mixed fluid vesicle and a charged colloid” J. Chem. Phys. **131**:105103.

[44] Gao, H., Shi, W., & Freund, L. B. (2005) “Mechanics of receptor-mediated endocytosis” Proc. Natl Acad. Sci. USA **102**:9469–9474.

[45] Chaudhuri, A., et al. (2011). "The effect of interactions on the cellular uptake of nanoparticles." Phys Biol **8**(4): 046002.

[46] Decuzzi, P., & Ferrari, M. (2008) “The Receptor-Mediated Endocytosis of Nonspherical Particles” Biophys. J. **94**:3790–3797.

[47] Smith, A.-S., Sengupta, K., Goennenwein, S., Seifert, U., & Sackmann, E. (2008) “Force-induced growth of adhesion domains is controlled by receptor mobility” Proc. Natl Acad. Sci. USA **105**:6906–6911.

[48] Fenz, S. F., Smith, A.-S., Merkel, R. & Sengupta, K. (2011) “Inter-membrane adhesion mediated by mobile linkers: Effect of receptor shortage” Soft Matter **7**:952–962.

[49] Tzlil, S., Deserno, M., Gelbart, W. M. & Ben-Shaul, A. (2004) “A statistical-thermodynamic model of viral budding” Biophys. J. **86**:2037–2048.

[50] Yi, X., & Gao, H., (2017) “Kinetics of receptor-mediated endocytosis of elastic nanoparticles” Nanoscale **9**:454–463.

[51] Morris, C., & Homann, U. (2001) “Cell Surface Area Regulation and Membrane Tension” J. Membr. Biol. **179**:79–102.

[52] Agudo-Canalejo, J. & Lipowsky, R. (2015) “Critical Particle Sizes for the Engulfment of Nanoparticles by Membranes and Vesicles with Bilayer Asymmetry” ACS Nano **9**:3704–3720.

[53] Qiu, Y., Liu, Y., Wang, L., Xu, L., Bai, R., Ji, Y., Wu, X., Zhao, Y., Li, Y., Chen, C. (2010) “Surface chemistry and aspect ratio mediated cellular uptake of Au nanorods” Biomaterials **31**(30):7606−7619.

[54] Gratton, S. E., Ropp, P. A., Pohlhaus, P. D., Luft, J. C., Madden, V. J., Napier, M. E., DeSimone, J. M. (2008) “The effect of particle design on cellular internalization pathways” Proc. Natl. Acad. Sci. U.S.A. **105**(33):11613−11618.

[55] Cherstvy, A. G. & Petrov, E. P., (2014) “Modeling DNA condensation on freestanding cationic lipid membranes” Phys. Chem. Chem. Phys. **16**:2020-2037.

[56] Yi, X., Shi, X. & Gao, H. (2018) “Cellular Uptake of Elastic Nanoparticles” Physics Review Letters 107:098101.

[57] Dasgupta, S., Auth, T., & Gompper, G. (2015) “Correction: Wrapping of ellipsoidal nano-particles by fluid membranes” Soft Matter **11**:7441–7444.

[58] Huang, C., Zhang, Y., Yuan, H., Gao, H., & Zhang, S. (2013) “Role of nanoparticle geometry in endocytosis: laying down to stand up” Nano Lett. **13**(9):4546–4550.

[59] Noda, T., Ebihara, H., Muramoto, Y., Fujii, K., Takada, A., Sagara, H., Kim, J. H., Kida, H., Feldmann, H. & Kawaoka, Y. (2006) “Assembly and budding of Ebolavirus” PLoS Pathog. **2**(9):e99.

[60] Welsch, S., Kolesnikova, L., Krahling, V., Riches, J. D., Becker, S., & Briggs, J. A. (2010) “Electron tomography reveals the steps in filovirus budding” PLoS Pathog. **6**:e1000875.

[61] Vácha, R., Martinez-Veracoechea, F. J., & Frenkel, D. (2011) “Receptor-mediated endocytosis of nanoparticles of various shapes” Nano Lett. **11**(12):5391–5395.

[62] Deserno, M. (2004). "When do fluid membranes engulf sticky colloids?" Journal of Physics: Condensed Matter **16**(22): S2061-S2070.

[63] Šarić, A. and A. Cacciuto (2012). "Fluid Membranes Can Drive Linear Aggregation of Adsorbed Spherical Nanoparticles." Physical Review Letters **108**(11).

[64] Bahrami, A. H., et al. (2012). "Tubulation and Aggregation of Spherical Nanoparticles Adsorbed on Vesicles." Physical Review Letters **109**(18).

[65] Ramos, L. (1999). "Surfactant-Mediated Two-Dimensional Crystallization of Colloidal Crystals." Science **286**(5448): 2325-2328.

[66] Šarić, A. and A. Cacciuto (2013). "Self-assembly of nanoparticles adsorbed on fluid and elastic membranes." Soft Matter **9**(29): 6677.

[67] Li, N., Sharifi-Mood, N., Tu, F., Lee, D., Radhakrishnan, R., Baumgart, T., & Stebe, K. J. (2017) “Curvature-Driven Migration of Colloids on Tense Lipid Bilayers” Langmuir **33**(2):600-610.

[68] Yu, Y. and S. Granick (2009). "Pearling of lipid vesicles induced by nanoparticles." J Am Chem Soc **131**(40): 14158-14159.

[69] Gozen, I., Billerit, C., Dommersnes, P., Jesorka, A. & Orwar, O. (2011) “Calcium-ion-controlled nanoparticle-induced tubulation in supported flat phospholipid vesicles” Soft Matter **7**:9706-9713.

[70] Ewers, H., Romer, W., Smith, A. E., Bacia, K., Dmitrieff, S., Chai, W. G., Mancini, R., Kartenbeck, J., Chambon, V., Berland, L., Oppenheim, A., Schwarzmann, G., Feizi, T., Schwille, P., Sens, P., Helenius, A. & Johannes, L. (2010) “GM1 structure determines SV40-induced membrane invagination and infection” Nat. Cell Biol. **12**:11-U36.

[71] Li, S. and N. Malmstadt (2013). "Deformation and poration of lipid bilayer membranes by cationic nanoparticles." Soft Matter **9**(20): 4969.

[72] Zuraw-Weston, S., Wood, D. A., Torres, I. K., Lee, Y., Wang, L., Jiang, Z., Lázaro, G. R., Wang, S., Rodal, A. A., Hagan, M. F., Rotello, V. M., & Dinsmore, A. D. (2019) “Nanoparticles binding to lipid membranes: from vesicle-based gels to vesicle tubulation and destruction” Nanoscale **39**:18464-18474.

[73] Needham, D. and D. Zhelev (2007) “Use of Micropipette Manipulation Techniques to Measure the Properties of Giant Lipid Vesicles” Perspectives in Supramolecular Chemistry, John Wiley & Sons, Ltd.: 102-147.

[74] Wang, B., et al. (2008). "Nanoparticle-induced surface reconstruction of phospholipid membranes." Proc Natl Acad Sci U S A **105**(47): 18171-18175.

[75] Yu, Y., Anthony, S. M., Zhang, L., Chul Bae, S., & Granick, S. (2007) “Cationic Nanoparticles Stabilize Zwitterionic Liposomes Better than Anionic Ones” J. Phys. Chem. C **111** (23):8233-8236.

[76] Mengistu, D. H., Bohinc, K., & May, S. (2009) “Binding of DNA to Zwitterionic Lipid Layers Mediated by Divalent Cations” J. Phys. Chem. B **113**:12277-12282.

[77] Angelova, M. I., Soléau, S., Méléard, P., Faucon, F., & Bothorel, P. (1992) Trends in Colloid and Interface Science VI edited by C. Helm, M. Lösche, and H. Möhwald (Steinkopff, Darmstadt) p. 127.

[78] Herold, C., et al. (2012). "Efficient electroformation of supergiant unilamellar vesicles containing cationic lipids on ITO-coated electrodes." Langmuir **28**(13): 5518-5521.

[79] Jiang, Y., et al. (2015) “The Interplay of Size and Surface Functionality on the Cellular Uptake of Sub-10 Nm Gold Nanoparticles” ACS Nano, **9**:9986–9993.

[80] Phillips, R. L., et al. (2009) “Gold Nanoparticle-Ppe Constructs as Biomolecular Material Mimics: Understanding the Electrostatic and Hydrophobic Interactions” Soft Matter **5**:607–612.

[81] Brust, M., Walker, M., Bethell, D., Schiffrin, D. J., & Whyman, R. (1994) "Synthesis of Thiol-Derivatized Gold Nanoparticles in a Two-Phase Liquid-Liquid System" J. Chem. Soc., Chem. Commun. **7**:801–802.

[82] Hostetler, M. J., Templeton, A. C., & Murray, R. W. (1999) "Dynamics of Place-Exchange Reactions on Monolayer Protected Gold Cluster Molecules" Langmuir **15**:3782–3789.

[83] Gong, Z., Hueckel, T., Yi, G., & Sacanna, S. (2017) "Patchy particles made by colloidal fusion" Nature, **550**:234-238.

[84] Stahl, E., Martin, T. G., Praetorius, F., Dietz, H. (2014) "Facile and scalable preparation of pure and dense DNA origami solutions" Angew Chem Int Ed Engl. **53(**47):12735-12740.

[85] Gerling, T., Kube, M., Kick, B., Dietz H. (2018) "Sequence-programmable covalent bonding of designed DNA assemblies" Sci Adv, **4**(8):1157.

[86] Wagenbauer, K. F., et al. (2017) "How we make DNA origami" ChemBioChem **18**:1873–1885.

[87] Siavashpouri, M., Wachauf, C. H., Zakhary, M. J., Praetorius, F., Dietz, H., & Dogic, Z. (2017) "Molecular engineering of chiral colloidal liquid crystals using DNA origami" Nature materials **16**(8):849-856.

[88] Marvin, D. A., & Hoffmann-Berling, H. (1963) "Physical and Chemical Properties of Two New Small Bacteriophages" Nature **197**:517.

[89]Fraden, S. (1995)"Phase transitions in colloidal suspensions of virus particles", p. 113-164 in "Observation, prediction and simulation of phase transitions in complex fluids" (M. Baus, L.F. Rull and J.P. Ryckaert, Eds.) Kluwer Academic Publishers, Dordrecht, NATO-ASI – Series C **460**.

[90] Khalkhal, F., Chaney, K. & Muller, S. (2016) "Optimization and application of dry photoresist for rapid fabrication of high aspect-ratio microfluidic devices" Microfluidics and Nanofluidics **20(**11):1-10.

[91] Veatch, S. L., Leung, S. S. W., Hancock, R. E. W., Thewalt, J. L. (2007) "Fluorescent probes alter miscibility phase boundaries in ternary vesicles" J. Phys. Chem. B **111**:502.

[92] Illingworth, J., & Kittler, J. (1987) "The Adaptive Hough Transform, IEEE Transactions on Pattern Analysis and Machine Intelligence" PAMI-9 **5**:690-698

[93] D. Young, (2016) "Hough transform for circles" Mathworks File Exchange version 1.2.0.0, https://www.mathworks.com/matlabcentral/fileexchange/26978-hough-transform-for-circles

[94] Deserno, M., & Bickel, T. (2003) "Wrapping of a Spherical Colloid by a Fluid Membrane" Europhys. Lett. **62**:767.

[95] Li, N. W., et al. (2017) “Curvature-Driven Migration of Colloids on Tense Lipid Bilayers” Langmuir **33**:600–610.

[96] Koltover, I., et al. (1999). "Membrane Mediated Attraction and Ordered Aggregation of Colloidal Particles Bound to Giant Phospholipid Vesicles." Physical Review Letters **82**(9): 1991-1994.

[97] Reynwar, B. J., et al. (2007). "Aggregation and vesiculation of membrane proteins by curvature-mediated interactions." Nature **447**(7143): 461-464.

[98] Saric, A., & Cacciuto, A. (2012) “Mechanism of Membrane Tube Formation Induced by Adhesive Nanocomponents” Phys. Rev. Lett. **109**:188101.

[99] Yue, T. T., & Zhang, X. R. (2012) “Cooperative Effect in Receptor Mediated Endocytosis of Multiple Nanoparticles” ACS Nano **6**:3196.

[100] Xiong, K., et al. (2017) “Cooperative Wrapping of Nanoparticles of Various Sizes and Shapes by Lipid Membranes” Soft Matter **13**:4644–4652.

[101] Šarić, A. and A. Cacciuto (2012). "Fluid Membranes Can Drive Linear Aggregation of Adsorbed Spherical Nanoparticles." Physical Review Letters **108**(11).

[102] Cooke, I. R., Kremer, K., & Deserno, M. (2005) “Tunable Generic Model for Fluid Bilayer Membranes” Phys. Rev. E: Stat., Nonlinear, Soft Matter Phys. **72**:011506.

[103] Wang, L., & Malmstadt, N. (2017) “Interactions between Charged Nanoparticles and Giant Vesicles Fabricated from Inverted Headgroup Lipids” J. Phys. D: Appl. Phys. **50**:415402.

[104] Nagle, J. F., Jablin, M. S., Tristram-Nagle, S., & Akabori, K. (2015) “What Are the True Values of the Bending Modulus of Simple Lipid Bilayers?” Chem. Phys. Lipids **185**:3 –10.

[105] Deserno, M. and W. M. Gelbart (2002). "Adhesion and Wrapping in Colloid−Vesicle Complexes." The Journal of Physical Chemistry B **106**(21): 5543-5552.

[106] Olbrich, K., Rawicz, W., Needham, D., & Evans, E. (2000) “Water Permeability and Mechanical Strength of Polyunsaturated Lipid Bilayers” Biophys. J. **79**:321–327.

[107] Sandre, O., et al. (1999). "Dynamics of transient pores in stretched vesicles." Proceedings of the National Academy of Sciences **96**(19): 10591-10596.

[108] Li, Y., & Gu, N. (2010) “Thermodynamics of Charged Nanoparticle Adsorption on Charge-Neutral Membranes: A Simulation Study” J. Phys. Chem. B **114**:2749–2754.

[109] Stachowiak, J.C., Hayden, C. C., & Sasaki, D. Y. (2010) "Steric Confinement of Proteins on Lipid Membranes Can Drive Curvature and Tubulation" Proc. Natl. Acad. Sci. U. S. A. **107**:7781.

[110] Adriani, G., de Tullio, M. D., Ferrari, M., Hussain, F., Pascazio, G., Liu, X., Decuzzi, P. (2012) "The preferential targeting of the diseased microvasculature by disk-like particles" Biomaterials **33**:5504−5513.

[111] Franquelim, H. G., Khmelinskaia, A., Sobczak, J. P., Dietz, H., & Schwille, P. (2018) "Membrane sculpting by curved DNA origami scaffolds" Nat Comm **9**:811.

[112] McMahon, H. T. & Gallop, J. L. (2005) "Membrane curvature and mechanisms of dynamic cell membrane remodelling" Nature **438**:590–596.

[113] Paasonen, L., et al. (2007) "Gold Nanoparticles Enable Selective Light-Induced Contents Release from Liposomes" J. Controlled Release **122**:86–93.

[114] Whitmore, S. E., Potten, C. S., Chadwick, C. A., Strickland, P. T., Morison, L. W. (2001) "Effect of Photoreactivating Light on UV Radiation-Induced Alterations in Human Skin" Photodermatol Photoimmunol Photomed. **5**:213-217.

[115] McLaughlin, S. (1989) "The electrostatic properties of membranes" Ann. Rev. Biophys. Biophys. Chem. **18**:113-136.

[116] Andelman, D. (1995) "Electrostatic properties of membranes: the Poisson–Boltzmann theory, R. Lipowsky, E. Sackmann" (Eds.) (2nd Edition), Structure and Dynamics of Membranes, 1, Elsevier, Amsterdam, **12**:603-642.

[117] Lifson, S., & Katchalsky, A. (1954) "The electrostatic free energy of polyelectrolyte solutions: ii. Fully stretched macromolecules" J. Polymer Sci. **13**:43-55.

[118] Lekkerkerker, H. N. W. (1989) "Contribution of the electric double layer to the curvature elasticity of charged amphiphilic monolayers" Phys. A. **159**:319-328.

[119] Helfrich, W. (1973) "Elastic Properties of Lipid Bilayers: Theory and Possible Experiments" Z. Naturforsch. C **28**:693.

[120] Rozycki, B., Lipowsky, R., Weikl, T. R. (2008) "Effective surface interactions mediated by adhesive particles" EPL **84**:26004.

[121] Herold, C., Schwille, P., & Petrov, E. P. (2016) "Single DNA molecules on freestanding and supported cationic lipid bilayers: diverse conformational dynamics controlled by the local bilayer properties" J. Phys. D: Applied Phys. **49**:7.

[122] Herold, C., Schwille, P., & Petrov, E. P. (2010) “DNA Condensation at Freestanding Cationic Lipid Bilayers” Phys. Rev. Lett. **104**:148102.

[123] Ghosh, S. K., Cherstvy, A. G., Petrov, E. P., & Metzler, R. (2016) “Interactions of rod-like particles on responsive elastic sheets” Soft Matter **12**:7908-7919.

[124] Petrova, A. B., Herold, C., & Petrov, E. P. (2017) “Conformations, and membrane-driven self-organization of rodlike fd virus particles on freestanding lipid membranes” Soft Matter **39**:7172-7187.

[125] Olinger, A. D., Spangler, E. J., Sunil Kumar, P. B., & Laradji, M. (2016) “Membrane-mediated aggregation of anisotropically curved nanoparticles” Faraday Discuss **186**:265.

[126] Baumgart, T., Capraro, B. R., Zhu, C., & Das, S. L. (2011) “Thermodynamics and Mechanics of Membrane Curvature Generation and Sensing by Proteins and Lipids” Annu. Rev. Phys. Chem. **62**:483-506.

[127] Czogalla, A., Kauert, D. A., Franquelim, H. G., Uzunova, V., Zhang, Y., Seidel, R., Schwille, P. (2015) “Amphipathic DNA Origami Nanoparticles to Scaffold and Deform Lipid Membrane Vesicles” Angew Chem Int Ed Engl. **54**(22):6501-6505.

[128] Khmelinskaia, A., Franquelim, H. G., Petrov, E. P., & Schwille, P. (2016) “DNA Nanostructures on Membranes as Tools for Synthetic Biology” Biophys J. **110** (8):1698-1707.

[129] Qualmann, B., Koch, D., Kessels, M. M. (2011) “Let's Go Bananas: Revisiting the Endocytic BAR Code” EMBO J. **30**(17):3501-3515.

[130] Lipowsky, R. (2013) “Spontaneous tubulation of membranes and vesicles reveals membrane tension generated by spontaneous curvature” Faraday Discuss. **161**:305-331.

[131] Weikl, T. R. (2003) “Indirect interactions of membrane-adsorbed cylinders” Eur. Phys. J. E **12**:265-273.

[132] Mkrtchyan, S., Ing, C., & Chen, J. Z. Y. (2010) “Adhesion of cylindrical colloids to the surface of a membrane” Phys. Rev. E **81**:011904

[133] Muller, M. M., Deserno, M., & Guven, J. (2007) “Balancing torques in membrane-mediated interactions: exact results and numerical illustrations” Phys. Rev. E **76**:011921.

[134] Kim, K. S., Neu, J., & Oster, G. (2000) “Effect of protein shape on multibody interactions between membrane inclusions” Phys. Rev. E **61**:4281-4285.

[135] Longo, M. L., & Ly, H. V. (2007) “Micropipet Aspiration for Measuring Elastic Properties of Lipid Bilayers,” Methods Mol. Biol. **400**:421–437.

[136] Leriche, G., Manafirad, A., Nguyen, S., Bell, N., Patterson, J. P., Thayumanavan, S., Yang, J., Dinsmore, A. D., & Gianneschi, N. C. (2018) "Water Permeability and Elastic Properties of an Archaea Inspired Lipid Synthesized by Click Chemistry" Chem. Mat. **30**:3618-3622.

[137] Barry, E., Bellar, D., & Dogic, Z. (2009) "A model liquid crystalline system based on rodlike viruses with variable chirality and persistence length" Soft Matter **5**:2563-2570.

[138] Marvin, D. A., & Wachtel, E. J., (1975) "Structure and assembly of filamentous bacterial viruses" Nature **253**:19-23.